GEND-INF- 060 - V1
July 1985
Volume 1

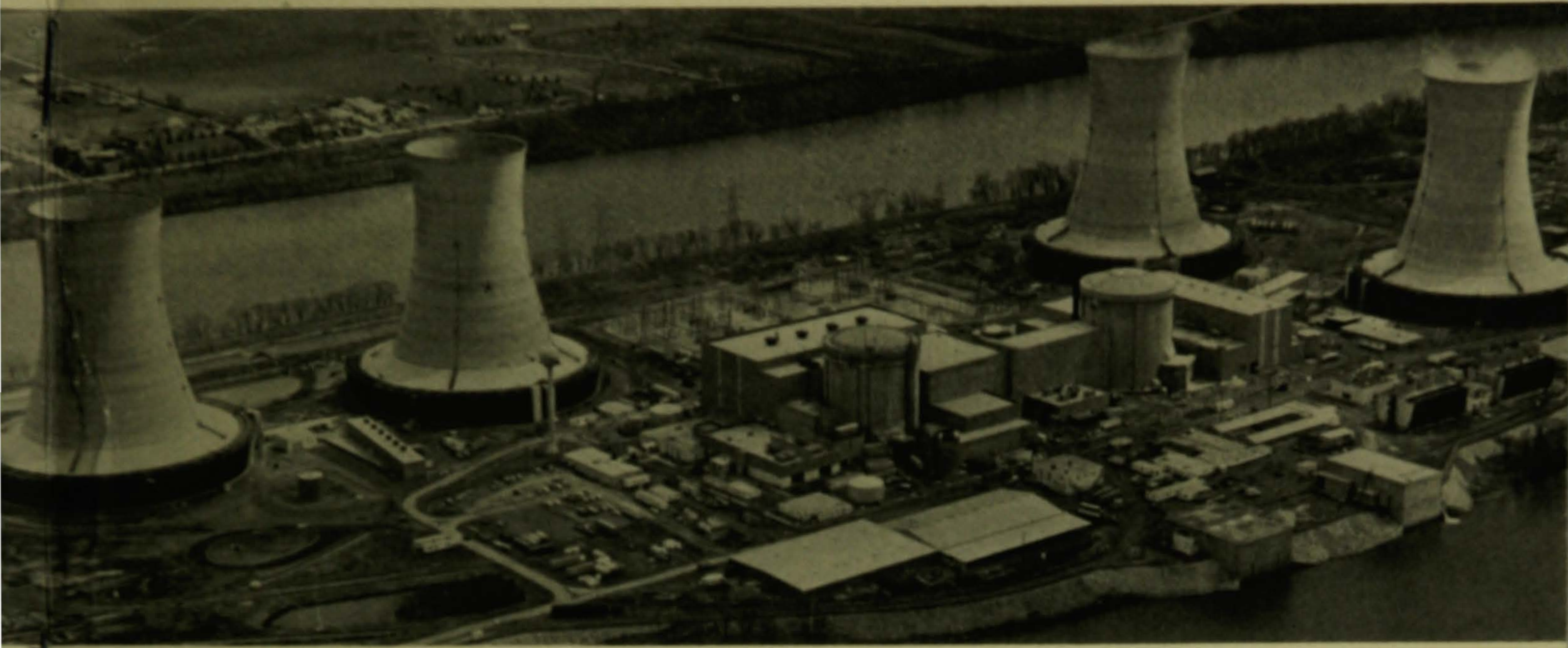

This is an informal report intended for use as a preliminary or working document

GEND

General Public Utilities • Electric Power Research Institute • U.S. Nuclear Regulatory Commission • U.S. Department of Energy

PRELIMINARY REPORT: TMI-2 CORE DEBRIS GRAB SAMPLES--ANALYSIS OF FIRST GROUP OF SAMPLES

Douglas W. Akers
Beverly A. Cook
Scott A. Ploger

GEND-INF-060
Volume 1

PRELIMINARY REPORT: TMI-2 CORE DEBRIS GRAB SAMPLES--ANALYSIS OF FIRST GROUP OF SAMPLES

Douglas W. Akers
Beverly A. Cook
Scott A. Ploger

Published July 1985

EG&G Idaho, Inc.
Idaho Falls, Idaho 83415

Prepared for the
U.S. Department of Energy
Three Mile Island Operations Office
Under DOE Contract No. DE-AC07-76ID01570

ABSTRACT

Six samples of particulate debris were removed from the TMI-2 core rubble bed during September and October 1983. The core debris grab samples (~30 cm^3 each) were obtained by lowering sampling devices through leadscrew openings at two locations in the core, H8 (mid-core) and E9 (mid-radius). Five of the six samples are being examined at the Idaho National Engineering Laboratory to obtain data on the physical and chemical nature of the debris and the postaccident condition of the TMI-2 core. This report presents results from the first phase of the examination and focuses primarily on the initial metallurgical and radiochemical examinations. The results are preliminary and, in many instances, require additional supportive examinations to reasonably interpret the data. Preliminary results indicate temperatures in the core reached at least 2900 K during the accident and large fractions of the core inventory of some radionuclides (e.g., ^{144}Ce) were retained in the core.

SUMMARY

Six samples of particulate debris were removed from the TMI-2 core rubble bed during September and October 1983. These core debris grab samples were acquired to obtain data on the extent and nature of the debris and the postaccident condition of the TMI-2 core. Five samples are being examined at EG&G Idaho, Inc. The other sample is being examined at the Lynchburg Research Center of Babcock & Wilcox Company.

Results from the first phase of the examination are presented in this report. This phase focused on data needed by GPU Nuclear to support reactor recovery. It consisted of the following activities: unpackaging, weighing, and visual and photographic examination of bulk samples; sieving (to determine particle size distribution) and weighing of sieve fractions; preliminary metallurgical and scanning electron microscopy examinations; testing for ferromagnetic material content; pyrophoricity tests; and gamma spectrometry and fissile/fertile material analyses. Discrete particles from the larger ($\geq$1000 μm) diameter sieve fraction sizes and aliquots from the smaller (<1000 μm) sieve fraction sizes were selected for the gamma spectrometry and fissile/fertile examinations.

A brief summary of findings from this phase of the examination is given below:

- Approximately 90% of the particles from the sample material are larger than 1000 μm (1 mm); less than 1% are smaller than 300 μm. The average particle size is approximately 2000 μm, and the bulk tap densities of the debris range from 3.5 to 3.8 g/cm^3.

- The samples contain fuel pellet fragments and shards of cladding or guide tubes. Most particles are a conglomerate mixture of nonuniform combinations of fuel (UO_2) and non-fuel materials. Further analysis of these materials is planned.

- Preliminary examination of selected large particles indicates peak core temperatures reached during the accident exceeded 2900 K.

- No pyrophoric (combustible) materials were observed during the pyrophoricity tests.

- The ferromagnetic material content of one sample examined was less than 1% of the total sample weight, and the ferromagnetic particles were mostly within the size range between 74 and 4000 μm.

- The following gamma emitting radionuclides are present in the samples: ^{60}Co, ^{106}Ru, ^{110m}Ag, ^{125}Sb, ^{134}Cs, ^{137}Cs, ^{144}Ce, ^{154}Eu, and ^{155}Eu. The predominant radionuclides are ^{137}Cs and ^{144}Ce.

- Based on a limited number of particles examined, the average measured enrichments at the H8 and E9 core locations are 2.4 and 2.8%, respectively, indicating that no significant amounts of peripheral core materials are present at the center of the core (i.e., H8) at the locations sampled.

- Measured gamma spectrometry and fissile/fertile data were compared with results of the ORIGEN-2 code. Preliminary evaluations indicate that some fission products (i.e., ^{144}Ce, ^{154}Eu, and ^{155}Eu) remained primarily with the fuel, whereas large percentages (>50%) of other fission products (principally ^{125}Sb, ^{134}Cs, and ^{137}Cs) were depleted from the debris (fuel bearing) material.

ACKNOWLEDGMENTS

Many people contributed to the analysis of the core debris samples. Special thanks go to the following individuals: Calvin Rowsell and the staff at the Radiation Measurement Laboratory for their timely gamma spectrometry analysis of the samples; Yale D. Harker and Paul R. Napper for developing the fast neutron flux measurement facility and performing the fissile/fertile material analysis; Joseph E. Stoyack for his assistance in conducting the metallography; Daniel A. Pavlica of Westinghouse Idaho Nuclear Company, Inc. for performing Auger and energy dispersive x-ray spectroscopy measurements and scanning electron microscopy examinations; Dr. Peter Hofmann of KfK in the Federal Republic of Germany for his invaluable, indepth review and analysis of the metallographic results; Orval D. Simpson for his critical review of the data; and Johan O. Carlson, Thomas E. Cox, Michael R. Martin, Jim K. Jacoby, Richard R. Hobbins, and Harley W. Reno for their assistance in analyzing data and reviewing the manuscript.

CONTENTS

FIGURES

TABLES

NOMENCLATURE

Aliquot - A representative fraction of a homogeneous particle size fraction.

Fragmented Piece - A small chip or chunk removed from a particle for analysis.

Large Particle - Particle of debris greater than or equal to 1000 μm in size.

Particle - A piece of debris.

Particle Size Fractions - Subgroupings of the samples by size, resulting from the sieving operation. There are nine size ranges, varying from less than 30 μm to greater than 4000 μm.

Sample - All debris contained in a sampling tool, as-received from GPU Nuclear. Six samples were removed from the TMI-2 core region. EG&G Idaho is examining five of the six samples.

Small Particle - Particle of debris smaller than 1000 μm in size.

PRELIMINARY REPORT: TMI-2 CORE DEBRIS GRAB SAMPLES--ANALYSIS OF FIRST GROUP OF SAMPLES

1. INTRODUCTION

On 28 March 1979, the Unit 2 pressurized water reactor at Three Mile Island (TMI-2) underwent a loss-of-coolant accident that resulted in severe damage to the core. As a consequence of the TMI-2 accident, numerous aspects of light water reactor safety have been questioned, and the U.S. Nuclear Regulatory Commission (NRC) has embarked on a thorough review of reactor safety issues, particularly the causes and effects of severe core damage accidents. The nuclear community acknowledges the importance of examining TMI-2 in order to understand the nature of the core damage. Immediately after the accident, four organizations with interests in both plant recovery and accident data acquisition formally agreed to cooperate in these areas. These organizations, General Public Utilities Nuclear Corporation (GPU Nuclear--owner/operator of TMI), Electric Power Research Institute (EPRI), NRC, and the U.S. Department of Energy (DOE), collectively known as GEND, are presently involved in postaccident evaluations of TMI-2. DOE is providing a portion of the funds for reactor recovery (in those areas where accident recovery knowledge will be of generic benefit to the light water reactor industry of the United States). In addition, DOE is providing funds for acquisition and analysis of severe accident data (such as will be obtained from examining the damaged core).

Acquisition and examination of core debris grab samples from TMI-2 are part of an examination program of core internals recommended by the TMI Reactor Assessment/Fission Product Behavior Technical Evaluation Group. The data and results of the examinations presented in this report support data requirements of GPU Nuclear for reactor recovery. The examinations are being performed to acquire data on the extent and nature of the damage and postaccident condition of the core to assist GPU Nuclear in assessing tooling and procedures required to defuel the TMI-2 reactor. The principal reactor recovery questions being addressed by the core debris examinations include the following:

- What is the physical form of the particulate core debris (particle size, shape, morphology, origin, etc.)?

- What are the chemical forms of the debris (fuel, cladding, control material, structural material, reaction products, etc.)?

- What are the identities and quantities of fission products retained in the debris?

- What are the release rates of radioisotopes from existing and freshly created surfaces?

- Are pyrophoric materials present in the debris, and, if so, to what extent?

- Does the core debris present any unanticipated defueling concerns (filtration properties, settling rate, etc.)?

- What is the airborne potential for radioactive particles (fines)? [This question will be addressed in subsequent examinations and is not part of this report.]

- Can the water that is physically or chemically entrained in the debris be removed readily to facilitate shipping and storage of the core debris? What drying conditions are required? [This question will be addressed in subsequent examinations and is not part of this report.]

Data obtained to answer these questions will aid defueling in numerous ways. The physical form of the debris (particle size and structure) is significant, because small size particles may be suspended during defueling and cause cloudiness in the water. Particle size distribution and filterability also will determine the type and effectiveness of filters, cyclones, and so forth, used for cleaning the water. Information on the physical state of debris particles (e.g., presence of previously molten materials) may provide a clue as to the nature of the core material underneath the loose debris layer. The physical and mechanical properties of the core materials will influence the design of tools and methods used for defueling. The retained fission product content of the debris also is important, because it represents a potential radiological source that must be controlled. The rate at which radioisotopes can be leached from the debris will affect the amount of radioactive materials dissolved in the water during defueling. The presence of pyrophoric materials in the debris may suggest that larger concentrations of those materials exist below the loose debris, which could present hazards during preparations for shipping. Water entrained in debris material represents a potential for the radiolytic buildup of hydrogen and oxygen gas in closed storage containers.

Six samples of particulate debris (identified as Samples 1 through 6) were obtained from the TMI-2 rubble bed during September and October 1983 by lowering sampling devices through leadscrew openings at two locations in the TMI-2 core, H8 (mid-core) and E9 (mid-radius). Two different sampling devices were used to extract the samples from the rubble bed. One was a clamshell type tool used to obtain the surface samples. The other was a rotating tube device used to obtain the subsurface samples. Figure 1 shows the sampling schematic for the TMI-2 core debris. Figure 2 is a summary schematic showing the core location and photograph of each bulk sample. Figure 3 shows the sampling tools used to obtain the samples. The samples are from three depths: surface of the debris bed, and 3 and 22 in. into the bed. After removal, the six samples were shipped to EG&G Idaho, Inc. Subsequently, Sample 2 was shipped to Babcock and Wilcox Company (B&W) for examination and analysis. The core debris grab samples are the first materials extracted from the TMI-2 debris bed.

This is Volume 1 in a series of reports documenting the examination of the core debris grab samples from TMI-2. This report provides preliminary data on the physical characteristics and radionuclide concentrations of five samples being examined at the Idaho National Engineering Laboratory (INEL). Follow-on examinations will supplement these data and assist in resolving the principal questions discussed above. In addition, these data will be used, along with data from other tasks described in the <u>TMI-2 Core</u>

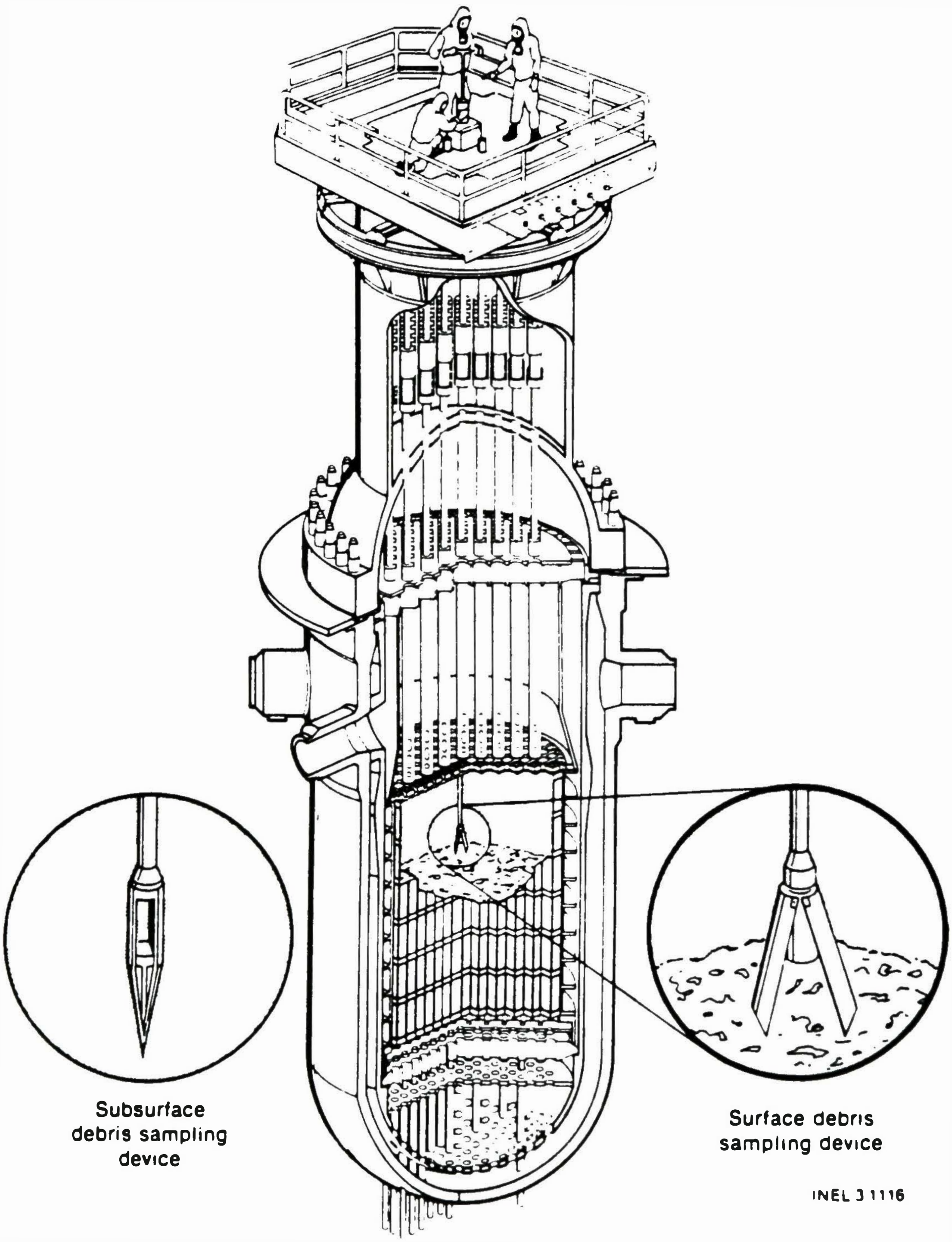

Figure 1. Sampling schematic for the TMI-2 core debris.

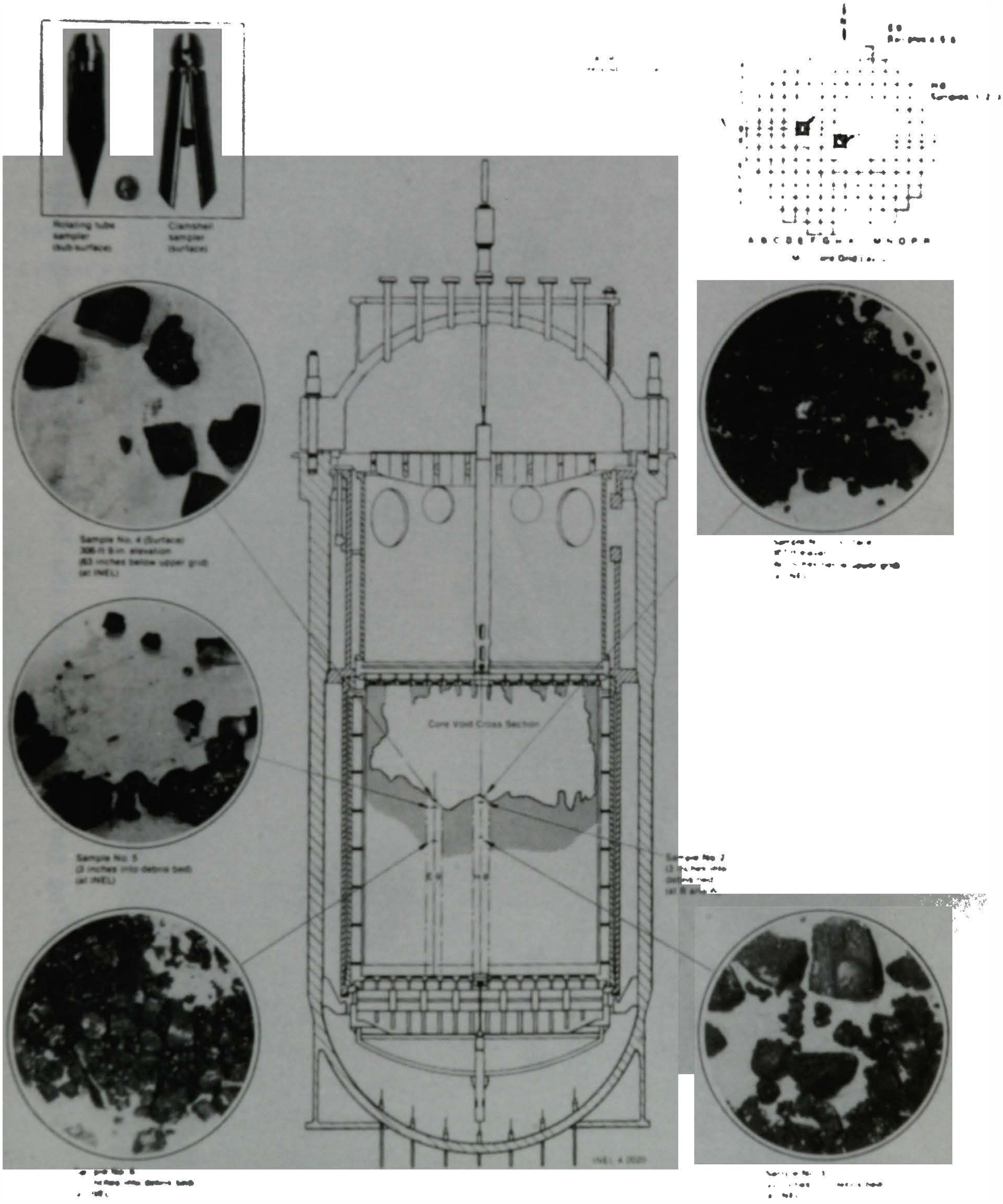

Figure 2. Summary schematic showing core location and photograph of each TMI-2 core debris grab sample

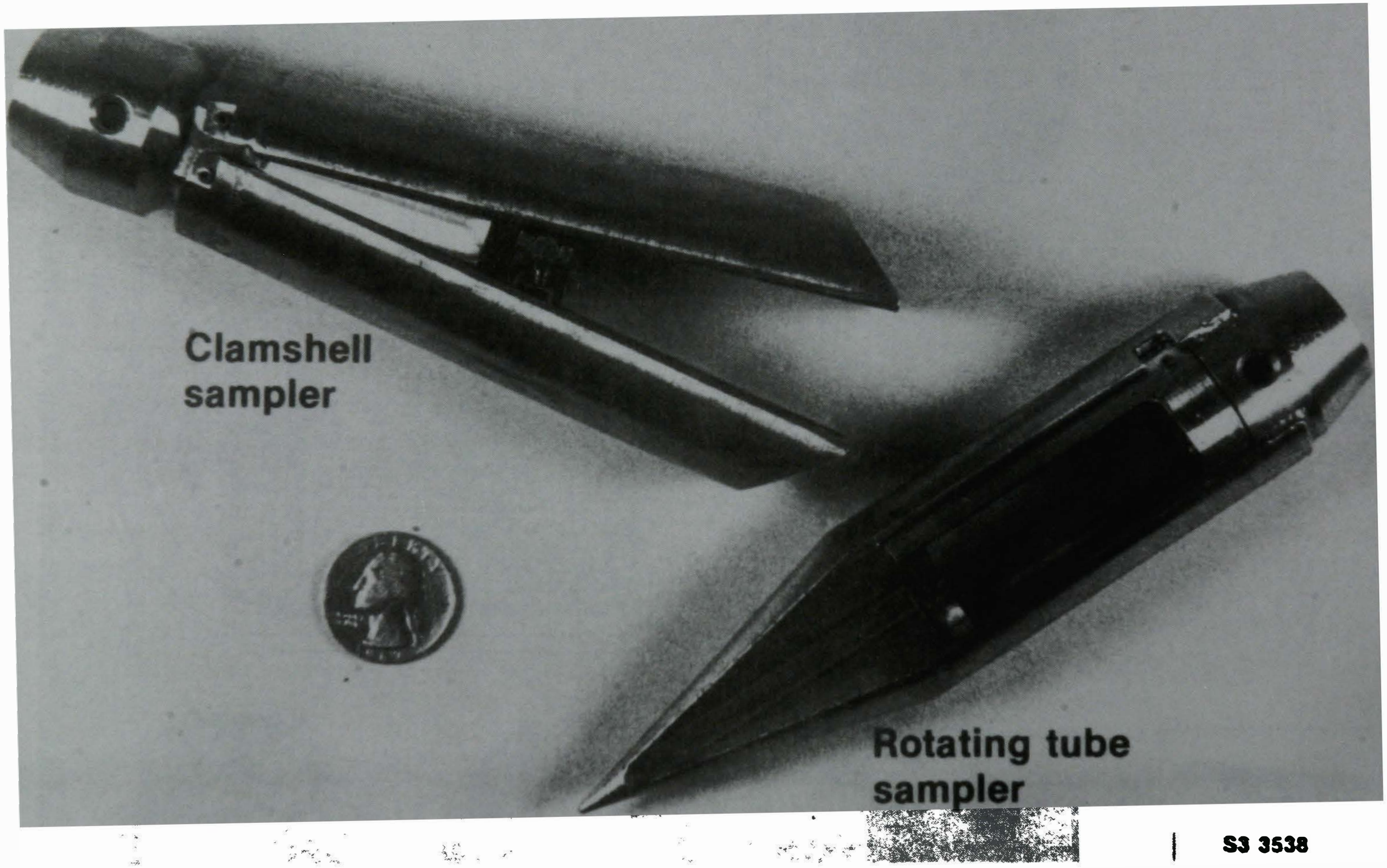

Figure 3. Sampling tools used to obtain the TMI-2 core debris grab samples.

Examination Plan,[1] to aid in defining the behavior of a commercial reactor reactor core under the accident conditions that occurred at TMI-2. Specifically, this report presents (a) bulk sample and individual particle geometry data (including particle size analysis), (b) results of metallurgical examinations of selected particles, (c) ferromagnetic material content data, (d) results of pyrophoricity tests, (e) gamma spectral measurements of the sieve fractions and some individual particles, and (f) fissile/fertile measurement data. The data are discussed, and a summary of observations is presented.

2. VISUAL AND PHOTOGRAPHIC EXAMINATIONS AND PARTICLE SIZING

After receipt from TMI, the five bulk samples retained at INEL (Samples 1, 3, 4, 5, and 6) were unpackaged and subjected to visual and photographic examinations and radiation survey. A summary of those results is presented in Table 1.

Before the particle size distribution analysis was performed, bulk tap density measurements (i.e., approximate volume and weight) were obtained for Samples 1, 3, and 6 (which are most representative of the debris bed). The tap densities ranged from 3.5 to 3.8 g/cm^3 for the three samples. Samples 4 and 5 were not analyzed, because they are composed primarily of large particles, and, therefore their tap density measurements would not provide a good indication of the actual density of the debris bed.

The bulk samples were subjected to particle size distribution analysis. This analysis was done by sieving the bulk samples into several progressively smaller particle size fractions (8 for most samples). The number and sizes of the divisions were determined during visual examination of the bulk samples and, in general, match those used by B&W. The results of this analysis are shown in Table 2. Both wet and dry sieving techniques were used. Dry, hand-agitated sieving was used to obtain the larger particle size fractions. For the smaller (<1000 μm) particle size fractions, wet sieving (i.e., Freon wash) was used to inhibit suspension of the smaller particles. The Freon wash was used because it does not react chemically with the core debris materials. The particle size distribution data are discussed further in Section 8.

Discrete particles from the larger (≥1000 μm) sieve fraction sizes were selected and photographed in preparation for follow-on examination. Photographs of these particles are shown in Appendix A. Detailed descriptions of each of the five bulk samples follow.

TABLE 1. RESULTS OF THE VISUAL AND PHOTOGRAPHIC EXAMINATION AND GROSS RADIATION SURVEY OF THE FIVE BULK SAMPLES

Sample	Sampling Tool	TMI-2 Core Location	Location of Sample in Rubble Bed	Gamma Radiation Level at 2.5 cm[a] (rad)	Visual Characteristics[b]
1	Clamshell	H8	Surface	16	A pile of very black, damp debris with a fairly wide range of particle sizes (up to 10 mm); several rounded surfaces; sporadic rust color throughout.
3	Rotating Tube	H8	22 in. into debris bed	36	Very black, slightly damp debris with wide range of particle sizes (up to 5 mm); small chunks to fine debris; similar to Sample 1.
4	Clamshell	E9	Surface	3	Thirteen major chunks of black, dry debris with rust colored sides; basically sharp edges with one or two chunks having rounded edges; dimensions range from 5 to 10 mm.
5	Rotating Tube	E9	3 in. into debris bed	18	Similar to Sample 4 with the following differences: many more pieces, greater size range (1 to 10 mm), some surfaces more reflective; very dry.
6	Rotating Tube	E9	22 in. into debris bed	36	Very black, slightly damp debris; small chunks to fine debris; some pieces blackish gray; a few pieces resemble metal shards similar to Sample 3.

---

a. Radiation levels measured using a teletector probe on the exposed sample.

b. All samples appeared to be of a loose granular nature with some sharp or rounded edges.

TABLE 2. RESULTS OF THE PARTICLE SIZE ANALYSIS OF THE FIVE BULK SAMPLES

Particle Size Range (µm)	Sample 1		Sample 3		Sample 4[a]	Sample 5[b]		Sample 6		Sample 6[c]
	(g)	(wt%)	(g)	(wt%)	(g)	(g)	(wt%)	(g)	(wt%)	(g)
>4000	12.62	18.4	63.75	42.9	--	69.57	77.1	57.99	42.0	--[d]
1680 to 4000	27.82	40.6	51.45	34.7	--	13.96	15.5	49.39	35.8	0.39
1000 to 1680	15.64	22.8	19.19	12.9	--	6.25	6.9	13.88	10.1	0.30
>1000	--	81.8	--	90.5	--	--	99.5	--	87.9	--
<1000	--	--	--	--	--	0.44	0.49	--	--	--
707 to 1000	7.80	11.4	5.49	3.7	--	--	--	8.93	6.5	0.25
297 to 707	3.20	4.7	6.34	4.3	--	--	--	5.99	4.3	0.19
149 to 297	0.87	1.3	1.27	0.86	--	--	--	0.97	0.70	0.025
74 to 149	0.44	0.64	0.77	0.52	--	--	--	0.67	0.48	0.024
30 to 74	0.17	0.25	0.18	0.12	--	--	--	0.22	0.16	--[d]
<30	--[d]	--	0.013	0.01	--	--	--	--[d]	--[d]	--[d]
Summed weight	68.56	--	148.45	--	--	90.22	--	138.04	--	1.178
Initial weight	70.88	--	152.71	--	16.59	90.96	--	140.73	--	--
Sample loss[e]	2.32	3.3	4.26	2.8	--	0.74	0.8	2.69	1.9	--

---

a. Sieving was not done. Sample consisted only of large particles.

b. Sieving was limited to four sizes. Sample consisted mostly of large particles.

c. Ferromagnetic material weights. These values are subsets of their respective weight fractions for Sample 6. The ferromagnetic material analysis of Sample 6 is discussed in Section 4 of this report.

d. None detected (not measurable).

e. The sample loss defines the quantity of material lost during sieving; however, the particle size distribution of the lost material is not known.

Sample 1, the surface sample from the H8 core location, was obtained using a clamshell sampling tool (see Figure 3). The sampling tool contained approximately 71 g of very black debris with a wide range of particle sizes. The particle sizes in this sample range from 30 μm to greater than 4000 μm, with most particles larger than 1000 μm. Figure 4 is a photograph of Sample 1. A unique particle from Sample 1, Particle 1A, is a large fuel rod remnant, approximately 19000 μm long, consisting of zirconium cladding with pieces of fuel attached (Figure 5). The outer surface of the cladding and all fracture surfaces appear smooth. Several other particles from Sample 1 also have smooth surfaces and rounded corners. There are no sharp fracture surfaces apparent on the particles. Several particles were selected from Sample 1 for detailed analysis. Photographs of these particles are presented in Appendix A.

Sample 3, the sample from 22 in. into the debris bed at the H8 location, was obtained using a rotating tube sampling tool (see Figure 3). Figure 6 shows the sample before it was removed from the sampling tool. The material was stratified by particle size within the sampling tool, with larger particles near the top and finer particles nearer the bottom. The material may have become stratified during shipment. The particle sizes in this sample range from 30 μm to greater than 4000 μm, as shown in Table 2, with most (90 wt%) particles greater than 1000 μm. This sample contains several particles that appear to be fractured fuel pellets. The sample is shown in Figure 7.

Sample 4, the surface sample from the E9 core location, consists of 13 larger particles ranging from 1000 μm to approximately 4000 μm. All particles have the appearance of fractured fuel pellets (Figure 8).

Sample 5, the sample from 3 in. into the debris bed at the E9 core location, contains almost all large (>1000 μm) particles (Figure 9). It appears similar to Sample 4. The lack of smaller (<1000 μm) particles in Samples 4 and 5 agrees with in-core closed circuit television video inspections which show that the E9 location and adjacent areas contain larger sized particles on the surface of the debris bed.[2]

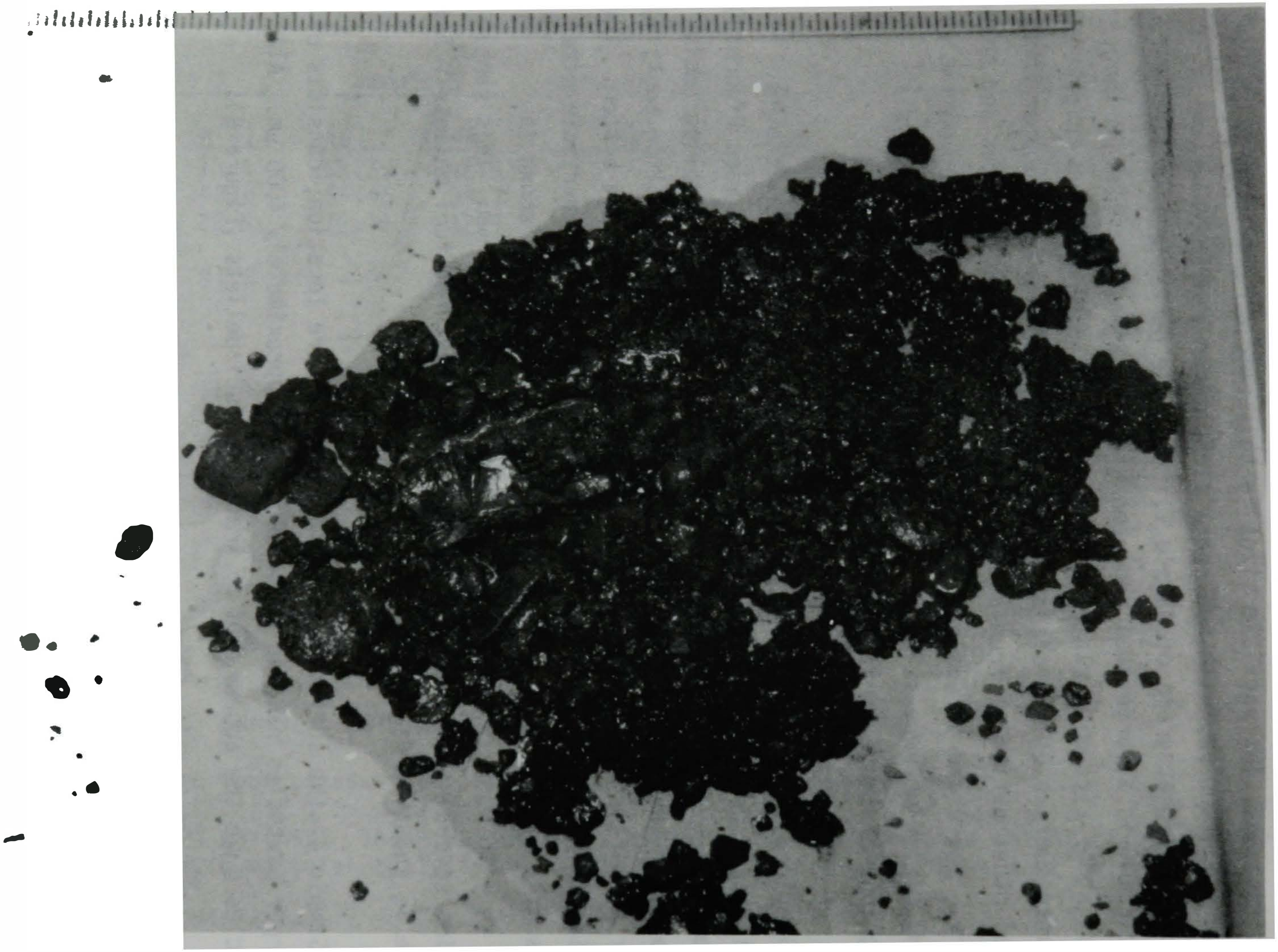

Figure 4. Photograph of Sample 1 which was obtained from the surface of the debris bed at the H8 core location.

83-655-3-17

84-216-2-27

Figure 5. Photograph of Particle 1A, a fuel rod remnant obtained from the surface of the debris bed at the H8 core location.

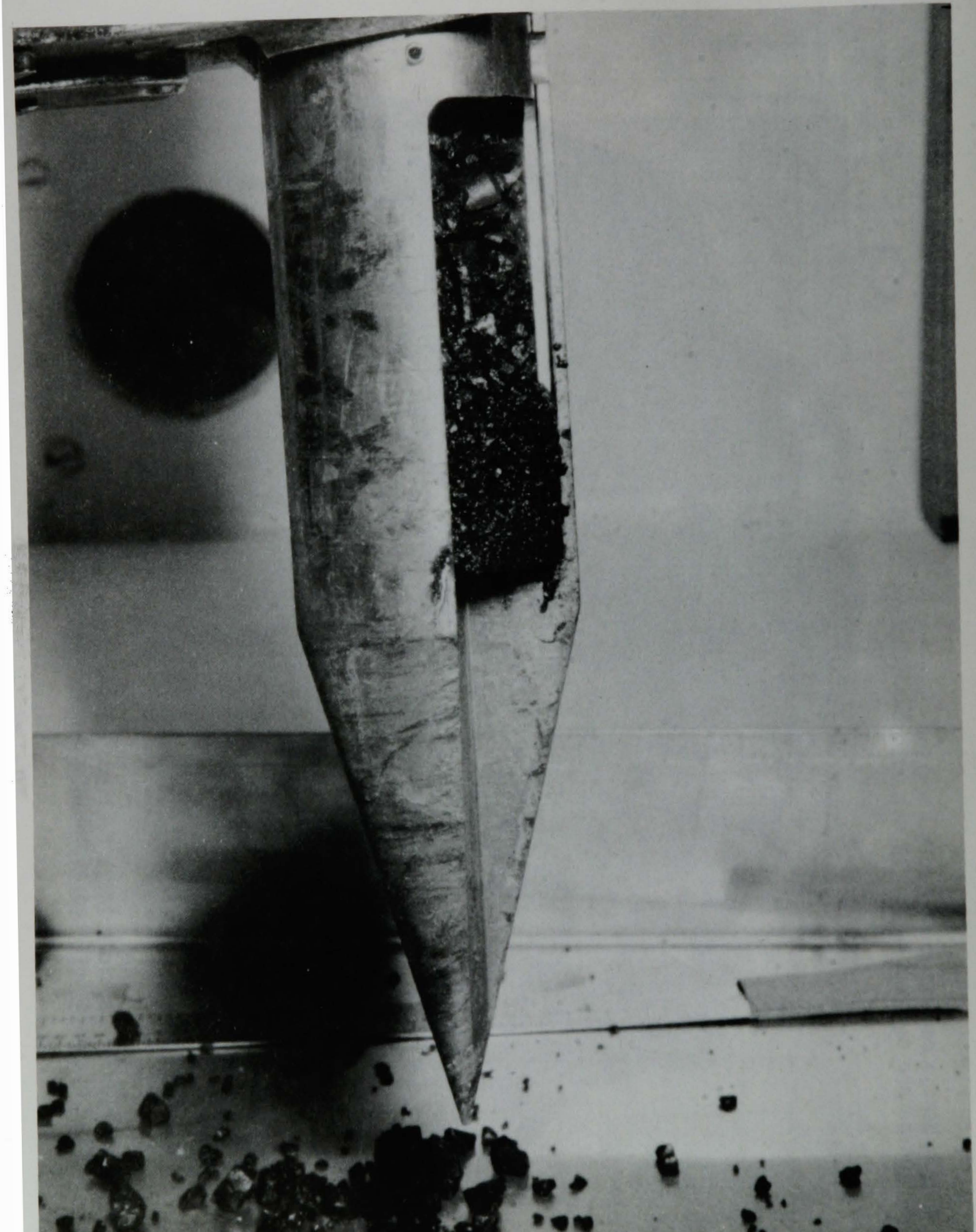

Figure 6. Photograph of Sample 3 in the rotating tube sampling tool.

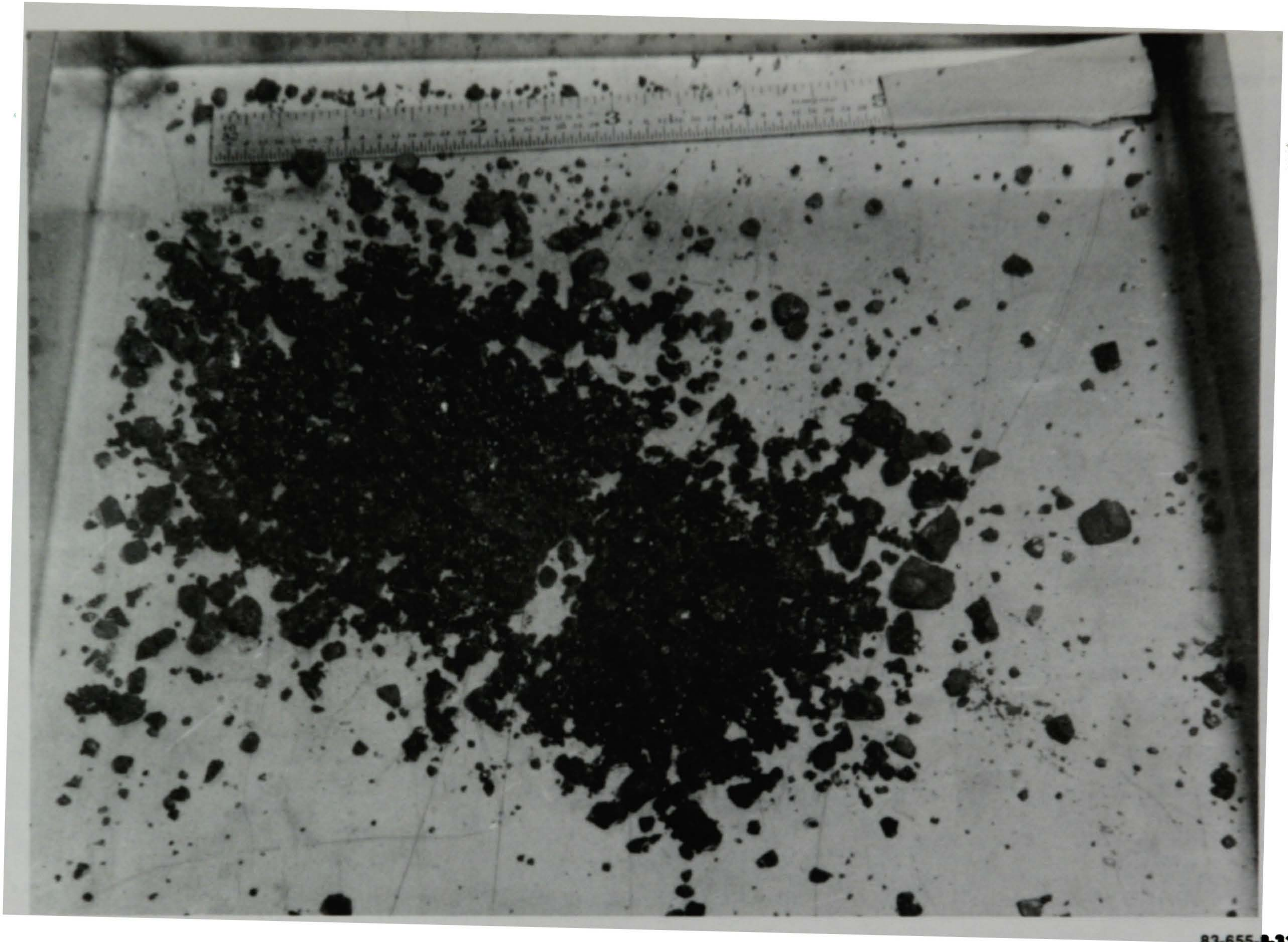

83-655-8-31

Figure 7. Photograph of Sample 3 which was obtained from 22 in. into the debris bed at the H8 core location.

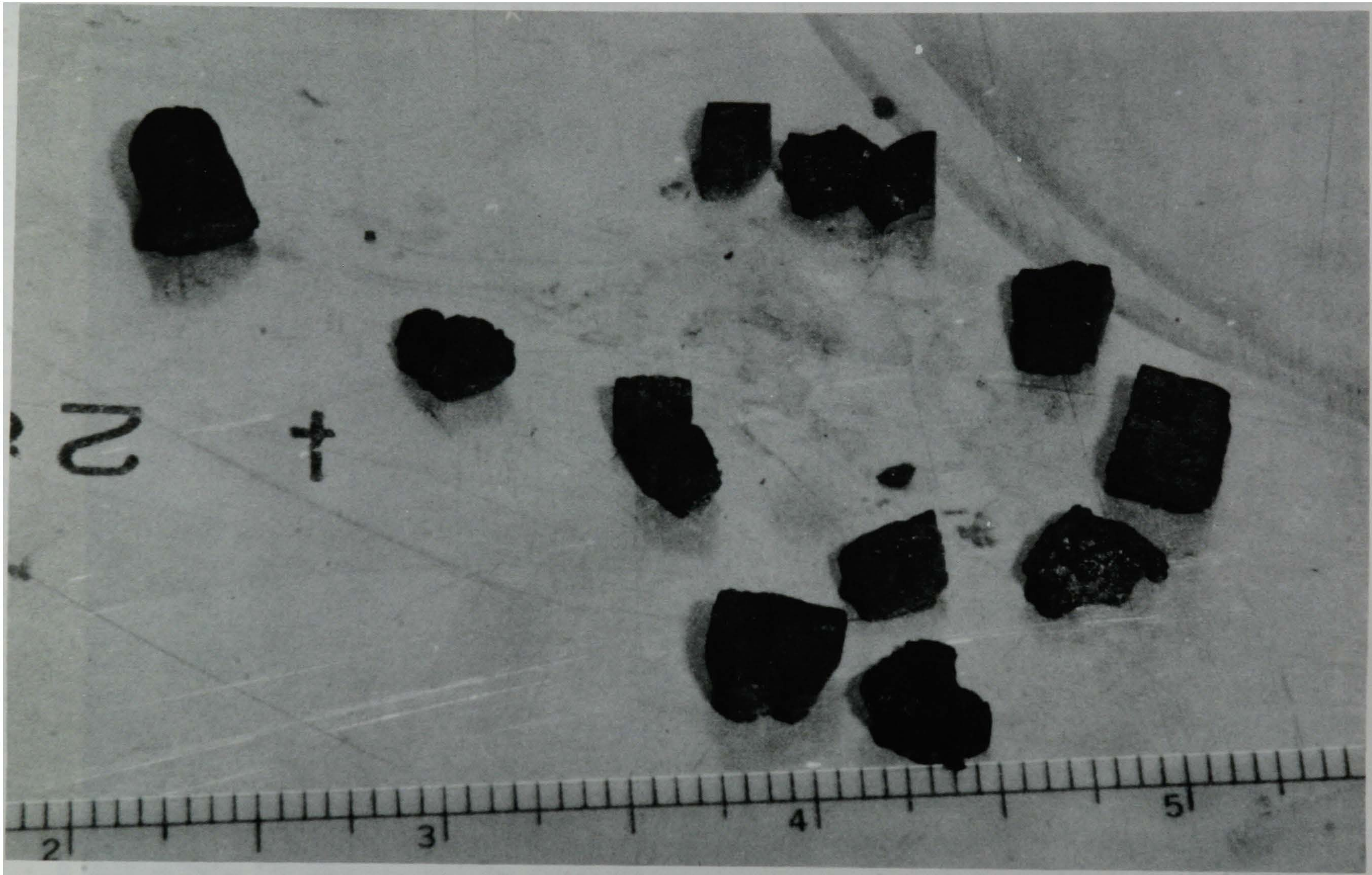

83-655-4-27

Figure 8. Photograph of Sample 4 which was obtained from the surface of the debris bed at the E9 core location.

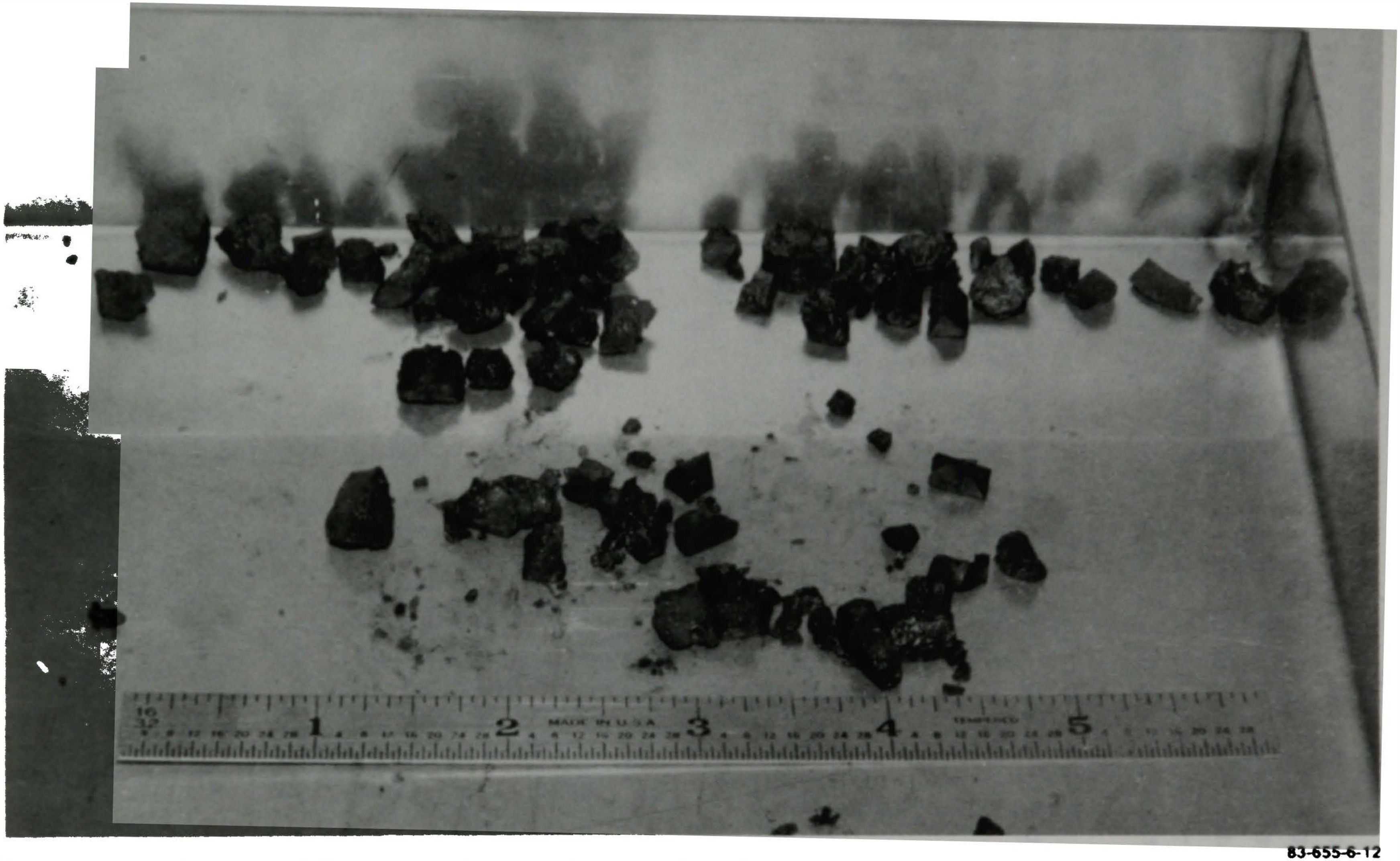

83-655-6-12

Figure 9. Photograph of Sample 5 which was obtained from 3 in. into the debris bed at the E9 core location.

Sample 6 (Figure 10), obtained from 22 in. into the debris bed at the E9 core location, is very similar to Sample 3. In general, 80 wt% or more of the particles from Sample 6 are larger than 1000 μm in size. Smaller particles may be absent from Sample 6 because of washout or settling. Evidence of washout of smaller particles was shown by examination of the TMI-2 makeup system filters and B8 and H8 leadscrews, which revealed particles in the 0.5- to 6-μm range.

A large fraction of the particles in all of the samples appear to be partially covered with rust. There is extensive coverage on some surfaces and a lack of coverage on other surfaces of the same particle.

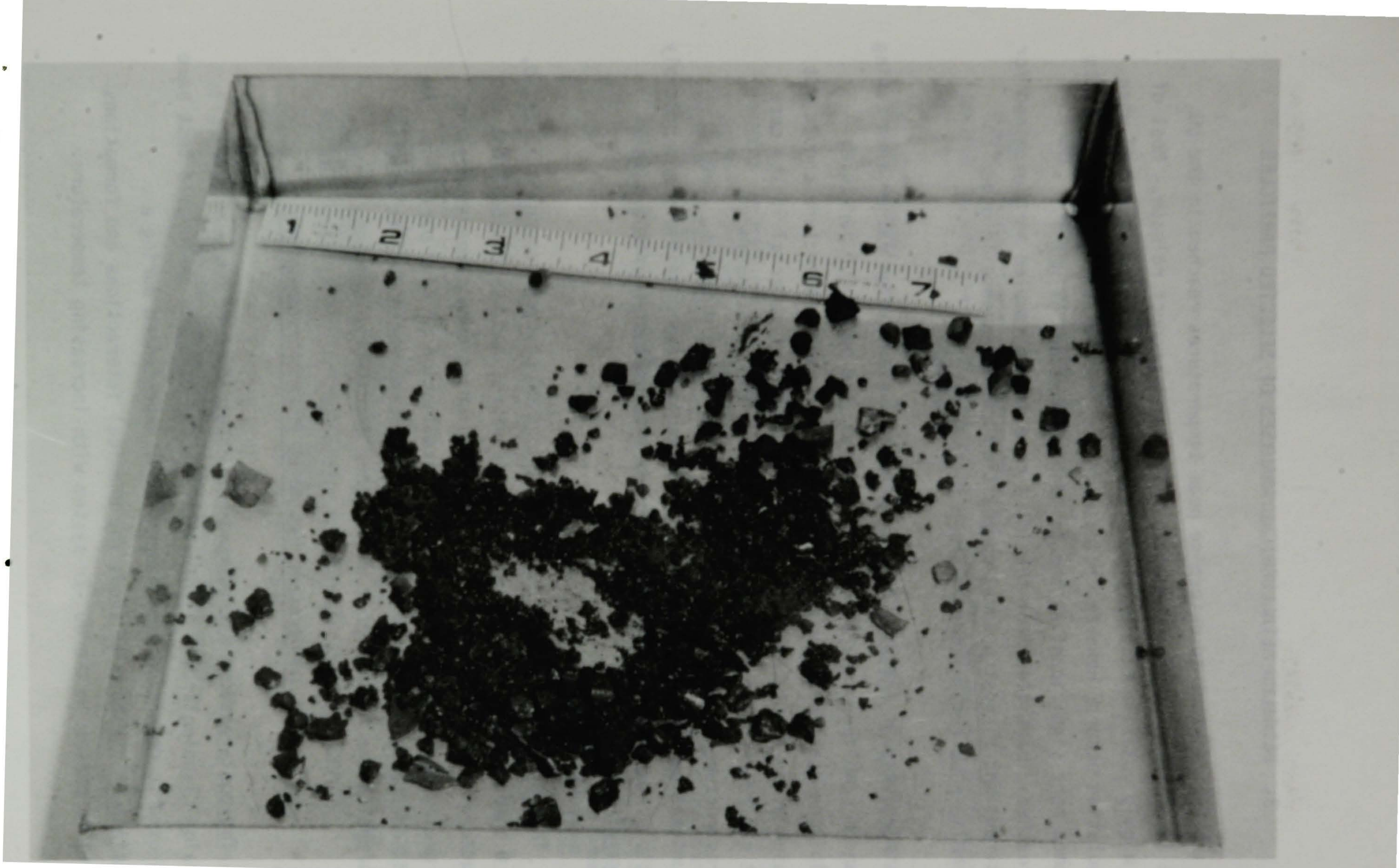

83-655-10-13

Figure 10. Photograph of Sample 6 which was obtained from 22 in. into the debris bed at the E9 core location.

3. DETAILED METALLURGICAL ANALYSES OF SELECTED PARTICLES

It is important to determine peak temperatures reached in the UO_2 fuel in order to correctly analyze the fission product release. Most of the highly volatile fission products will be released from the fuel when dissolution occurs; however, release of the less volatile fission products becomes more significant as the melting temperature of UO_2 is approached. Particles from the TMI-2 core debris samples were examined for posttransient microstructural composition and appearance in order to determine peak temperatures reached in the fuel.

Particles of interest were selected for examination rather than taking a random sampling of particles. Therefore, the number of particles exhibiting structures indicative of a certain peak temperature should not be used as an indicator of the relative amounts of material in the core that had reached those temperatures. Also, the posttransient microstructures were compared to equilibrium phase diagrams. The structures observed probably reflect nonequilibrium conditions and possibly multiple temperature excursions, making interpretation of the data a difficult task.

This section contains (a) descriptions of changes occurring in Zr, U, and O compositions with increasing temperature, and key compositions and structural features important for distinguishing peak temperatures and (b) preliminary results from detailed examination of five particles. An additional 24 particles are being examined, and those results will be reported in the final report on the core debris grab samples.

3.1 Temperature Estimates From Microstructure

The posttransient microstructural appearances of UO_2 fuel and zircaloy cladding from a light water reactor core and an in-pile test have been used to determine peak temperatures experienced during a transient.[3,4] Figure 11 shows the chemical interactions and formations of liquid phases in the UO_2-Zr system with increasing temperature.

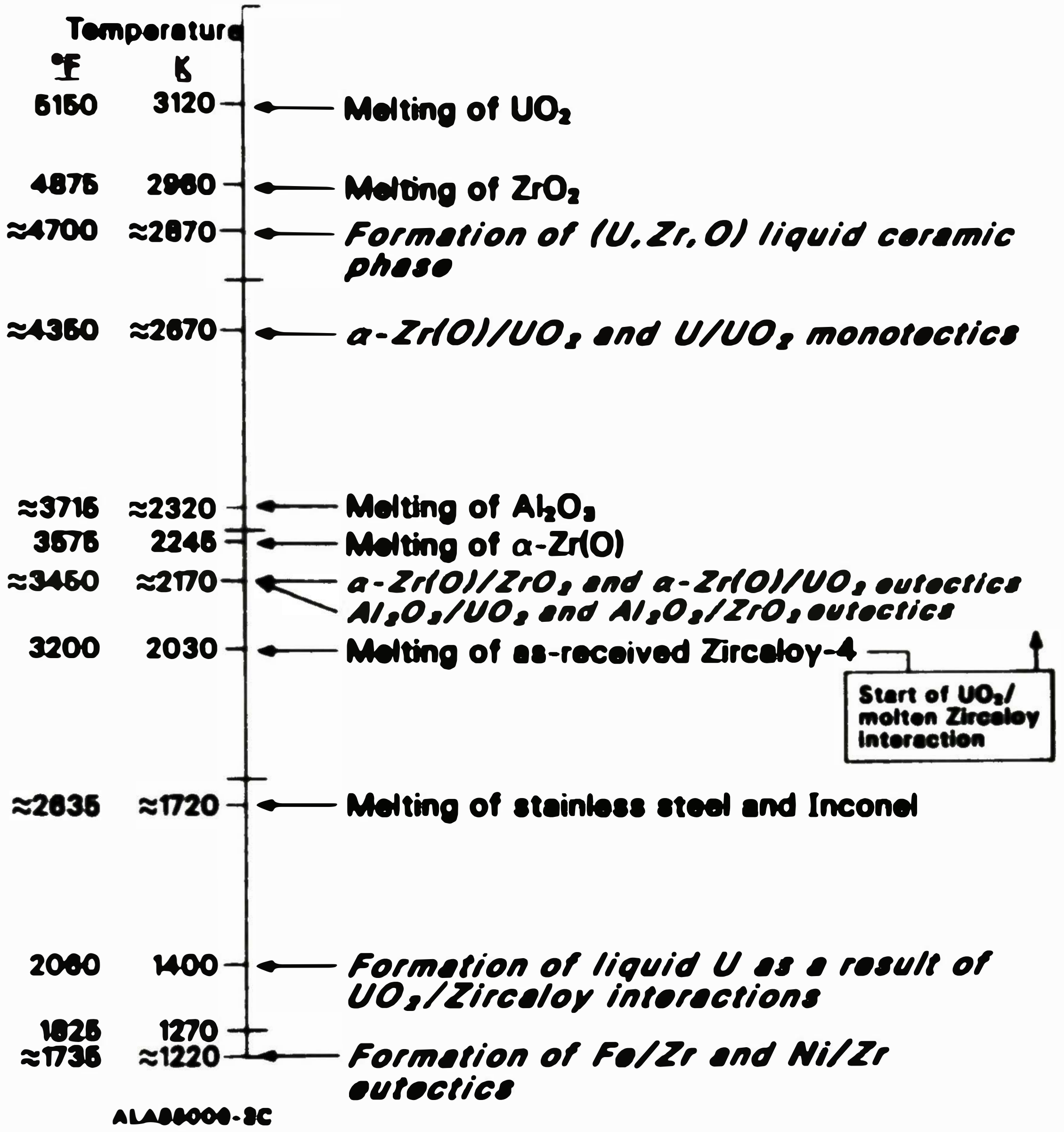

Figure 11. Chemical interactions and formations of liquid phases in the UO_2-Zr system with increasing temperature.

Several microstructural features have been used to determine peak temperatures, including (a) grain growth in the UO_2 fuel and evidence of melting, (b) phase changes in the Zr cladding, and (c) interaction of molten core materials. This section describes key features used in determining the peak temperatures.

3.1.1 Fuel Grain Growth and Melting

Fuel grain growth is highly time-temperature dependent and can be calculated using correlations of time at temperature for a given fuel burnup.[5] These calculations are based on an integrated total time at a given temperature, however, and are difficult to use for transient conditions and multiple temperature excursions. Indications that fuel was exposed to high (>2000 K) temperatures are the rearrangement of pores and grain structure. When the melting point (3120 K) of the UO_2 fuel is approached, the fuel grains become almost pore-free, sharp corners on the equiaxed grains become rounded, and the grains separate. The fuel has a slightly foamy appearance, having few small pores and many large, rounded voids.

3.1.2 Zircaloy Phase Changes with Temperature

The zircaloy cladding progresses through several distinct microstructural changes with increasing temperature. The original (as-fabricated) zircaloy microstructure consists of alpha-zircaloy (α-Zr) grains elongated in the circumferential direction (referred to as a stress-relieved microstructure). This structure is observed with peak temperatures of less than 920 K. With increasing temperature, the α-Zr grains recrystallize and become equiaxed ($920 < T < 1105$ K). At about 1105 K, the transformation from α-Zr to the β-Zr phase begins. The temperature at which this transformation occurs increases with increasing oxygen content in the Zr. The β-Zr transforms back to α-Zr as temperatures are reduced below 1105 K; however, the microstructural appearance of the transformed β-Zr grains (referred to as "prior β-Zr") is distinctly different from the α-Zr grains that were not exposed to temperatures greater than 1105 K. The two-phase α + prior β-Zr mixture is observed in materials exposed to $1105 < T < 1245$ K.

Several phenomena occur between $1245 < T < 2100$ K. As the temperature increases above 1245 K, the α-Zr transforms completely to β-Zr and then transforms back to α-Zr on cooling (prior β-Zr). The prior β-Zr structure appears as large, equiaxed grains with α-Zr platelets within each grain. Interaction of the zircaloy cladding with steam on its outside surface and UO_2 fuel on its inside surface becomes significant above 1245 K, and oxidation of the cladding occurs. Two layers are formed on the outside surface: first, a layer of α-Zr that has been stabilized at high temperatures because of oxygen uptake is formed [denoted "α-Zr(O)"], and then a layer of ZrO_2 is formed outside of the α-Zr(O) layer. The longer the cladding is exposed to temperatures greater than 1245 K, the thicker these two layers can become. The entire wall thickness can eventually transform to ZrO_2 and α-Zr(O). Frequently, there are two layers in the ZrO_2 phase. The inside layer [closest to the α-Zr(O)] contains a metallic α-Zr(O) phase. This indicates that the ZrO_2 was slightly hypostoichiometric at temperature and underwent an eutectoid decomposition into stoichiometric $ZrO_{2.00}$ + α-Zr(O) during cooling. This decomposition only takes place if significant amounts (enough to be visible) of the ZrO_2 have been above about 1850 K (Figure 12).

If fuel-cladding contact exists, interaction of the cladding with the UO_2 fuel also occurs, resulting in oxidation of the cladding from the inside surface. The internal UO_2/Zr interaction results in the formation of the following reaction layer sequence:

$$[UO_2 + U] \rightarrow [\alpha\text{-}Zr(O)_a + (U,Zr)]$$
$$\rightarrow (U,Zr)\ \text{alloy} \rightarrow \alpha\text{-}Zr(O)_b$$

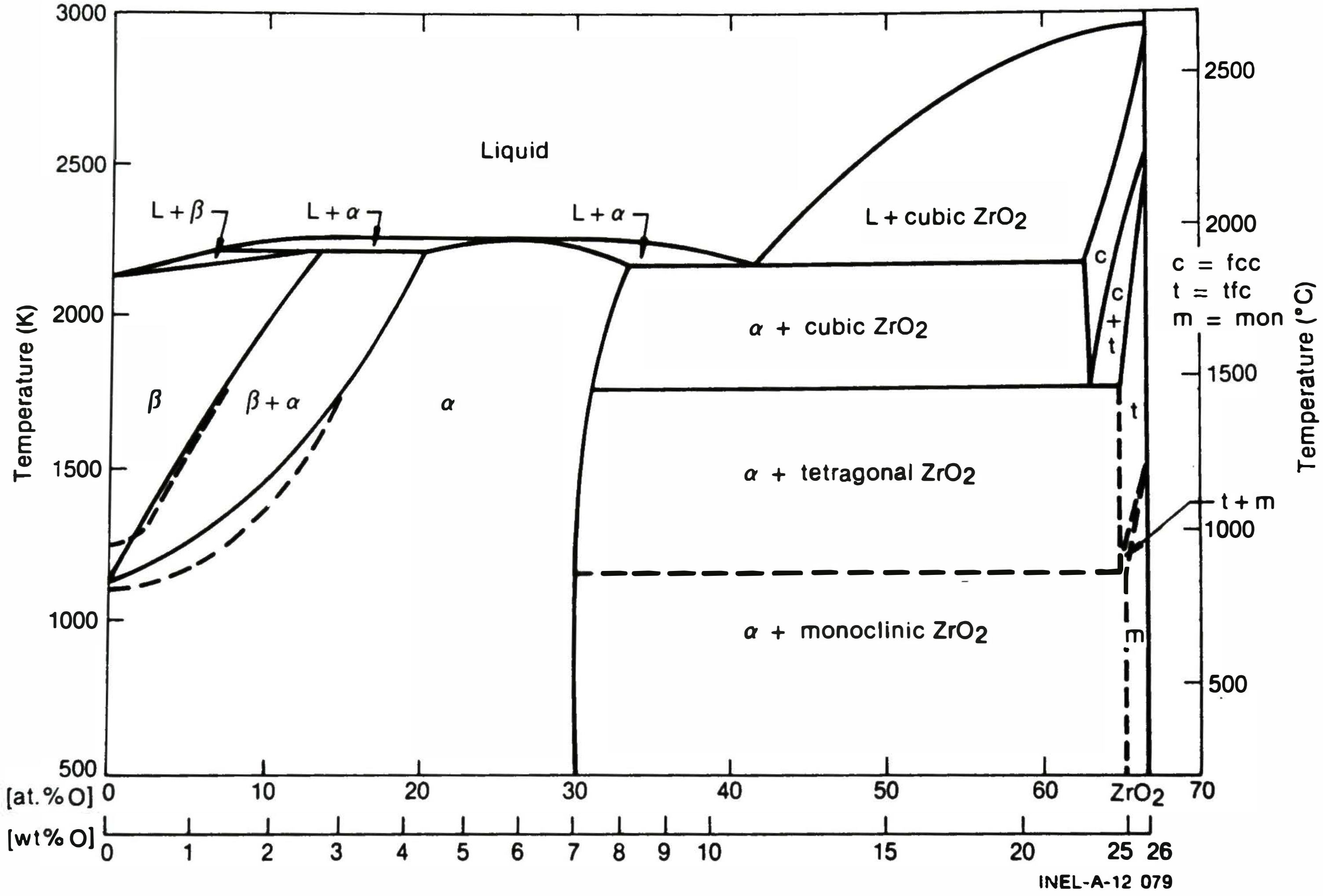

Figure 12. Zirconium-oxygen equilibrium phase diagram.

where

a = the α-Zr(O) next to the fuel

b = the α-Zr(O) near the center of the cladding.

These layers will then be followed by prior β-Zr → α-Zr(O) → ZrO_2 or only α-Zr(O) → ZrO_2, depending on the amount of oxidation from the outside by the steam. The fuel is chemically dissolved by the Zr to form metallic α-Zr(O) and elemental uranium. ZrO_2 cannot form as a result of the UO_2/Zr reaction alone. The metallic uranium does not remain at the $UO_2/\alpha\text{-}Zr(O)_a$ interface, because it tends to interact with Zr low in oxygen and therefore penetrates and/or diffuses into the cladding to form a (U,Zr) alloy rich in uranium. The (U,Zr) alloy lies between two α-Zr(O) layers and is liquid above about 1425 K, depending on the Zr content. This small quantity of liquid is a result of the solid state diffusion couple. The α-Zr(O) layer adjacent to the fuel contains small amounts of the (U,Zr) alloy, primarily along grain boundaries, but also as small globules within the $\alpha\text{-}Zr(O)_a$ grains. The $\alpha\text{-}Zr(O)_b$ layer adjacent to the prior β-Zr contains no (U,Zr) alloy. During cooldown, the hypostoichiometric UO_{2-x} decomposes into stoichiometric $UO_{2.00}$ and additional metallic uranium. The two-phase $[\alpha\text{-}Zr(O)_a + (U,Zr)]$ layer is made up of relatively small, radially elongated α-Zr(O) grains compared with the $\alpha\text{-}Zr(O)_b$ layer [and α-Zr(O) in general] which is made up of large grains.[6-12]

The boundary between the $[\alpha\text{-}Zr(O)_a + (U,Zr)]$ and (U,Zr) layers is distinct, but the interface between the (U,Zr) and $\alpha\text{-}Zr(O)_b$ layers can be very irregular. The formation of large (U,Zr) globules within the $\alpha\text{-}Zr(O)_b$ layers occurs only at temperatures greater than or equal to 1775 K; at lower temperatures, small spherical particles form (References 7 and 8).

3.1.3 Interaction of Molten Core Materials

The zircaloy cladding can begin to melt at 2030 K, while the UO_2 fuel does not melt until 3120 K; however, interaction of the Zr, UO_2, and steam results in materials with intermediate melting temperatures. The melting point of the Zr increases with increasing oxygen content, with the melting temperature of oxygen-saturated α-Zr(O) being about 2245 K. An eutectic interaction takes place between oxygen-saturated α-Zr(O) and UO_2 at about 2170 K (20 mole% UO_2), and a monotectic interaction at about 2670 K (85 mole% UO_2).[7] The UO_2 and ZrO_2 form a solid solution at high temperatures, and a 50/50 mole% composition melts at about 2870 K. Therefore, cladding melting and dissolution of the UO_2 fuel (liquefaction) can begin at temperatures as low as 2030 K. Other low-temperature eutectics may form between the fuel rod materials (Zr and UO_2) and other core structural materials (Inconel, stainless steel, and control rod materials).

The key to determining the peak temperatures reached and the possible scenario is the number and distribution of phases present in a previously molten material at room temperature. Neglecting alloying element effects, the observed phases should agree with the (U,Zr,O) ternary phase diagram. The ternary equilibrium phase diagrams of the (U,Zr,O) system at 1773 and 2273 K are shown in Figure 13. The equilibrium phases shown in the 1773 K diagram also are present at room temperature, because no further decomposition takes place at lower temperatures.

The initial tie-line lies between the UO_2 fuel and pure Zr at 2273 K. Interaction between these two components results in a single-phase homogeneous liquid or a two-phase (U,Zr,O) melt plus $(U,Zr)O_{2-x}$ solid (at >3.6-wt% oxygen). Upon cooling, the homogeneous melt will decompose into two metallic components: an α-Zr(O) phase containing some uranium and an (U,Zr) alloy containing little or no oxygen.[6,10,13]

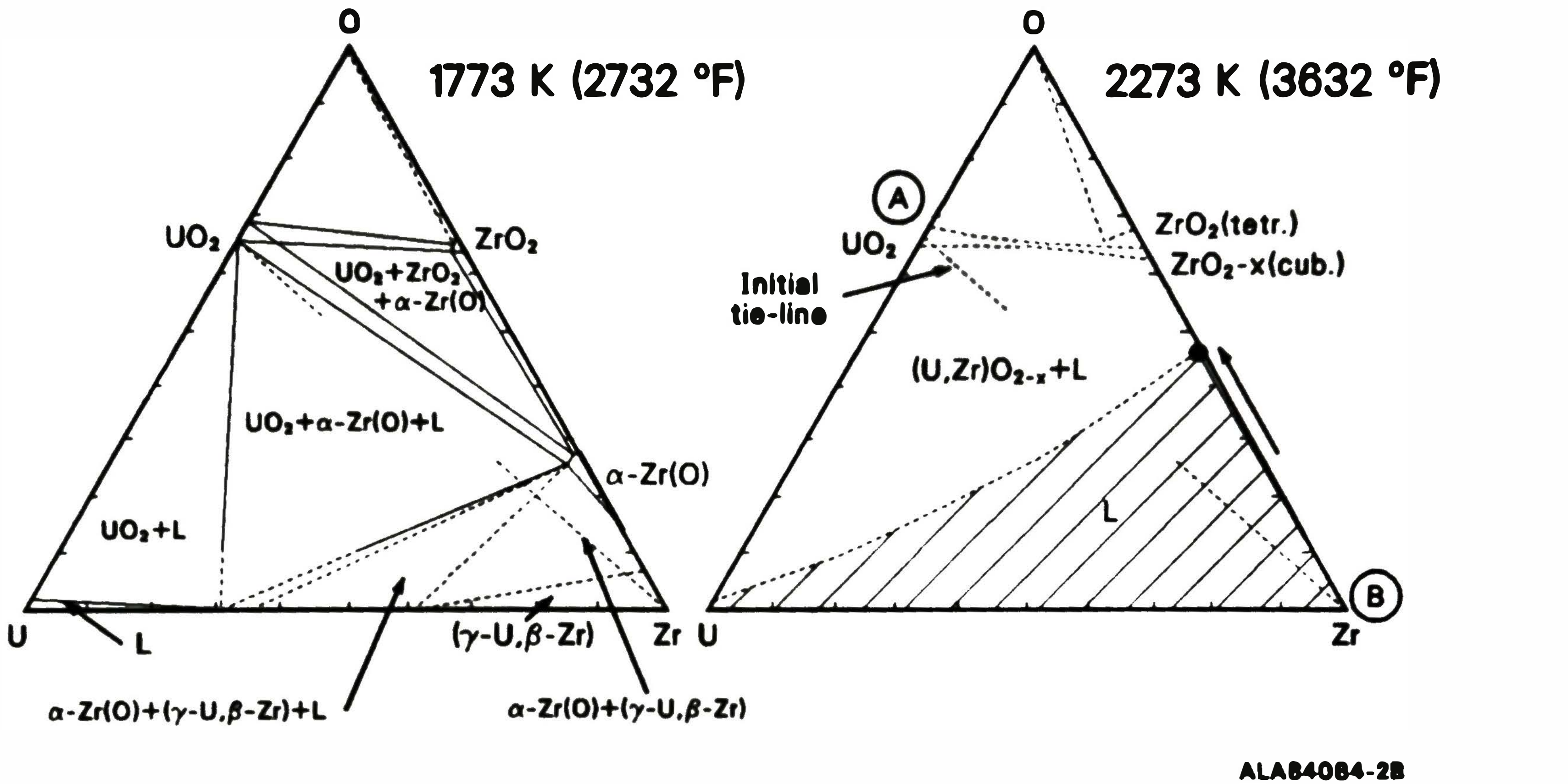

Figure 13. U-Zr-O ternary phase diagrams for temperatures of 1773 and 2273 K.

The heterogeneous melt also decomposes on cooldown, with the solid $(U,Zr)O_{2-x}$ particles having low Zr content decomposing into stoichiometric $(U,Zr)O_2$ and a (U,Zr) alloy, and the (U,Zr,O) melt decomposing into α-Zr(O) and (U,Zr) alloy.

Because of the transient conditions, oxidation of the heterogeneous and homogeneous melts must be considered, as this affects the final microstructural appearance. If oxidation occurs after solidification, the α-Zr(O) will transform to ZrO_2 and the (U,Zr) alloy will transform to $(U,Zr)O_2$. Therefore, the homogeneous melt will transform from α-Zr(O) + (U,Zr) to ZrO_2 + $(U,Zr)O_2$. Whatever the state of oxidation, two phases are always distinguishable.

The molten material may also absorb oxygen while in the liquid state. As the oxygen content of the melt increases, the temperature must increase for the material to remain molten, or a $(U,Zr)O_2$ solid solution forms. Oxidation of the UO_2-Zr melt will result in a single-phase $(U,Zr)O_2$ solid solution. This material will no longer have the appearance of being molten. Elongated grains will tend to form along the oxygen concentration and temperature gradient, and the material will generally contain few pores and be dense in appearance.

The ZrO_2 and UO_2 can also form a solid solution by diffusion at temperatures up to 2873 K and by mixing of molten oxides at higher temperatures. Figure 14 shows the ZrO_2/UO_2 binary phase diagram. The minimum melting point of the solid solution occurs at about the 50/50 mole% mixture. Only one phase is apparent on cooling of the $(U,Zr)O_2$ mixture. If this material had been molten, it would generally show structures such as large pores and irregular or nonexistent grain structure, usually associated with molten material.

Another indication of whether the posttransient $(U,Zr)O_2$ solid solution is a metallic melt which oxidized while liquid or a ceramic melt is the amount of interaction with other materials. If the metallic melt

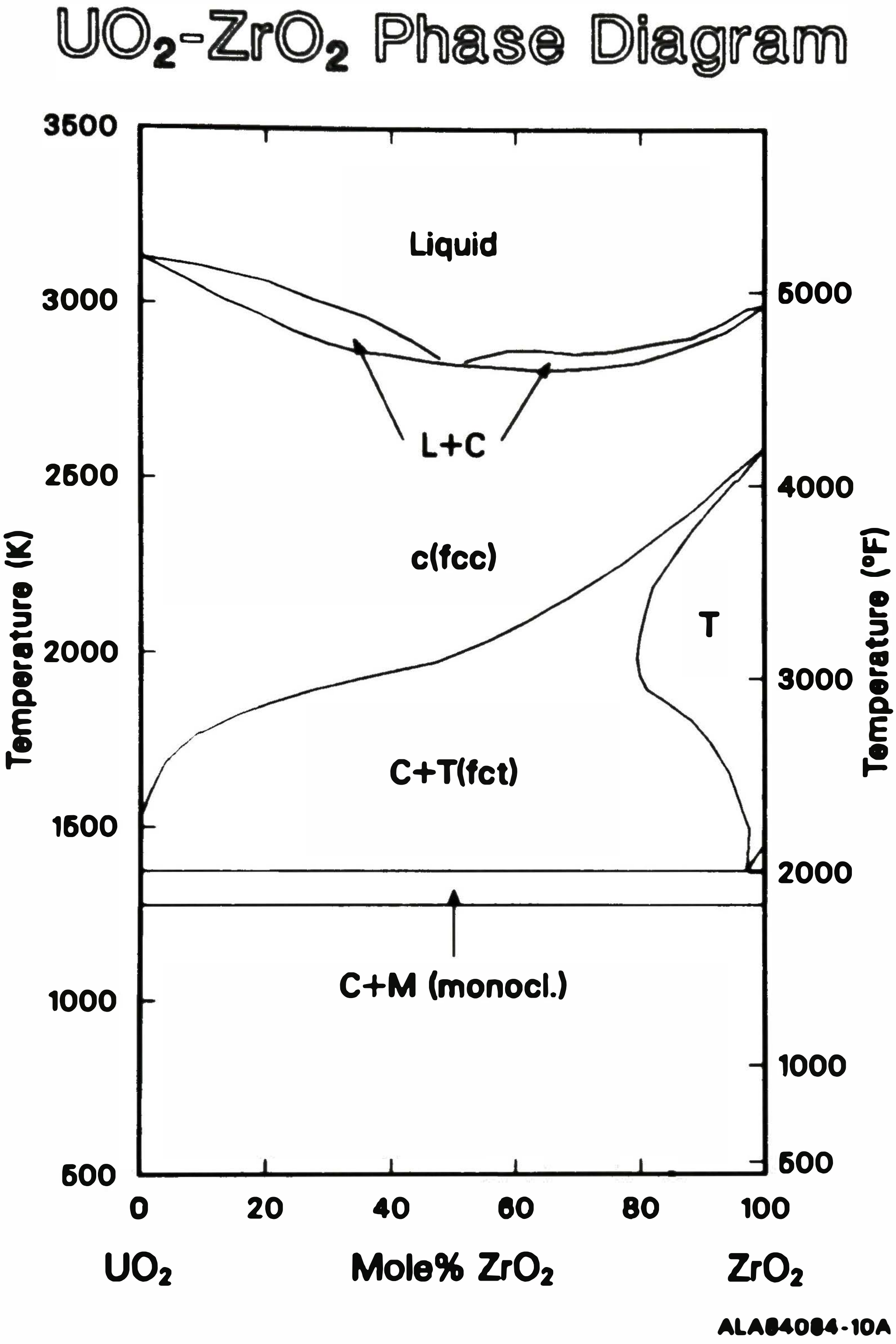

Figure 14. UO_2-ZrO_2 binary phase diagram.

contacted a ceramic material (UO_2 fuel or ZrO_2 oxidized cladding), dissolution of the ceramic should have occurred. A ceramic melt contacting a ceramic solid will show very little interaction.

3.2 Metallographic Findings and Composition Measurements

This section describes the results of the metallographic examinations and composition measurements of five particles (Particles 1A, 1E, 1H, 6D, and 6F) selected from the core debris grab samples. These particles have been studied extensively by metallography and scanning electron microscopy/energy-dispersive x-ray spectroscopy (SEM/EDS) to determine the basic structures present and the approximate elemental compositions, excepting oxygen. One particle (so far) has been further characterized by scanning Auger spectroscopy to measure concentrations of oxygen and other elemental species and confirm peak temperature interpretations. Additional work is scheduled on the Auger apparatus and on the molecular optical laser examiner (MOLE), primarily to ascertain extents of chemical interaction and study fission product behavior. Nevertheless, ample information has been gathered to help understand many of the high temperature phenomena that occurred during the TMI-2 transient.

EDS-derived composition information should be considered semiquantitative because the x-ray peak area fractions are converted into elemental weight fractions without the use of standards. The theoretical corrections applied to the peak area fractions compensate for mass attenuation, self-fluorescence, and atomic number effects and are more appropriate to metals than to oxides. Therefore, EDS values reported herein should be interpreted as relative indications of elemental amounts. The EDS instrumentation used is not capable of determining oxygen concentrations because of system limitations, which is the reason for also using Auger spectroscopy techniques.

However, some empirical correction factors for EDS-derived data (where necessary) will soon be available as a consequence of an analytical calibration program at INEL. A UO_2/Zr interaction standard was graciously donated by the Kernforschungszentrum Karlsruhe (Federal Republic of Germany) where UO_2, α-Zr(O), and (U,Zr) alloy were assessed by both Auger spectroscopy and electron microprobe, each of which had been previously calibrated to numerous standard materials. An extruded ZrO_2 rod (Corning Glass Co.) was also supplied by Babcock & Wilcox Co. to provide a known Zr-O ratio for Auger spectroscopy calibration. The rod composition was precisely determined by inductively coupled plasma spectrometry at INEL, and small amounts of CaO, MgO, Al_2O_3, Fe_2O_3, and other compounds were also measured. Thus, standards sliced from this rod will further serve to benchmark quantitative determinations of trace molecular concentrations and detectability thresholds for numerous analytical systems. Both rough and polished standards are being prepared to assess effects of surface texture.

3.2.1 Particle 1A

Particle 1A (Figure A-1) is composed of an outer shell of partially oxidized cladding, an intermediate region of once-molten U-Zr-O mixture, and an interior piece of UO_2 fuel. Thickness variations in the prior β-Zr wall and in the melt layer (Figure 15) indicate that the cladding ballooned asymmetrically (presumably as a consequence of unbalanced heat transfer), with a radial increase of approximately 1 mm at the orientation shown. Zircaloy in direct contact with fuel pellets above the ballooned region reacted to create a homogeneous (U,Zr,O) melt that relocated downward to fill the balloon space. The large voids with oxidized surfaces represent two portions of the melt that slumped further downward to be replaced by steam. The extent of oxidation suggests that steam flow occurred through these voids between two axially separated cladding breaches.

The melt composition was measured by EDS. Neglecting oxygen, which cannot be detected by this technique, the average composition over a representative portion is 87-wt% Zr, 11-wt% U, and 2-wt% Ni, with traces of Fe, Sn, and Cr. The Fe, Sn, and Cr content could be attributed to

Particle 1A

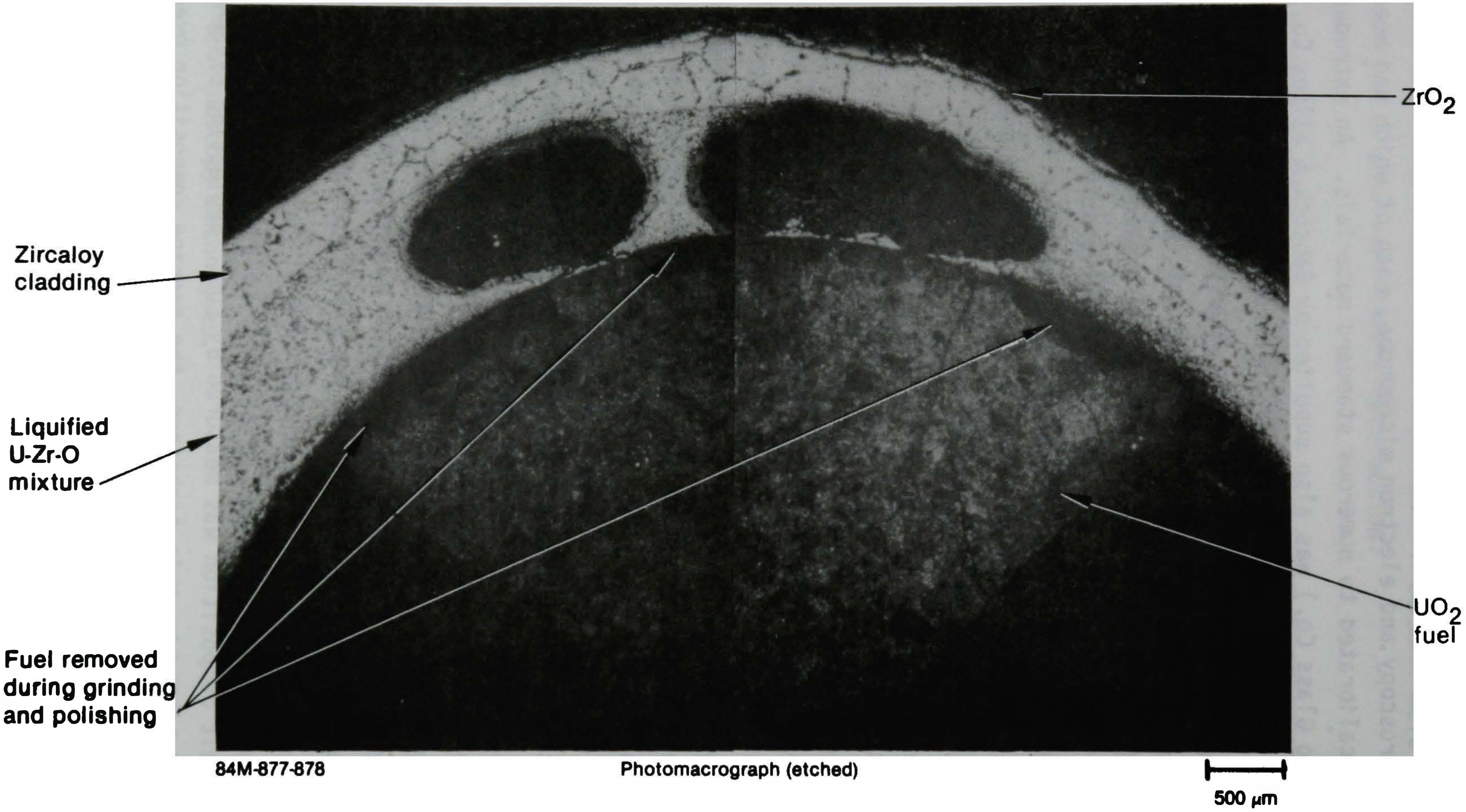

Figure 15. Particle 1A, liquefied U-Zr-O mixture and oxidized voids between fuel and ballooned, steam-oxidized cladding.

Zircaloy-4 alloying ingredients, but the Ni originated from other component sources (i.e., Inconel spacer grids, control rod guide tubes, fuel assembly end fittings, etc.).

As shown in Figure 16, appreciable segregation of melt constituents occurred upon cooldown, before solidification. Most of the Zr reconfigured into grains of α-Zr(O), while irregular patches of (U,Zr) alloy formed at grain junctions. The Sn, Ni, Fe, and Cr remained liquid longer, and were squeezed between the α-Zr(O) grains and (U,Zr) patches. The backscattered scanning electron micrograph at the bottom of Figure 16 illustrates this segregation quite clearly, because higher atomic number elements appear brighter. Steam oxidation of the melt effectively diluted the concentrations of Zr and U, so oxidized melt appears dark gray on this image.

The tendency of the melt to wet both the zircaloy cladding and the UO_2 fuel is apparent from the oval shapes of both voids in Figure 15. However, virtually no chemical interaction was found at the cladding-melt interface. Similarly, Zr and Fe were detected between UO_2 grains, but only in the immediate vicinity of the melt. Thus, the melt seems to have solidified shortly after arrival at this rod elevation. [Areas now absent of fuel near the pellet periphery were removed during sample preparation for metallography, and a thin layer of UO_2 still adheres to the melt at these positions.] The negligible UO_2 grain growth and rather thin ZrO_2 layer on the cladding exterior confirm that this fuel rod elevation stayed relatively cool.

3.2.2 Particle 1E

Particle 1E (Figure A-3b) is a partially oxidized cladding section with UO_2 fuel bonded to the interior surface and ZrO_2 on the outer surface. Two parallel, circumferentially oriented cladding bands (Figure 17) that are rich in uranium content provide evidence of high temperature zircaloy-UO_2 interactions. Radially oriented patches of ZrO_2 within the cladding matrix and large metallic stringers along the

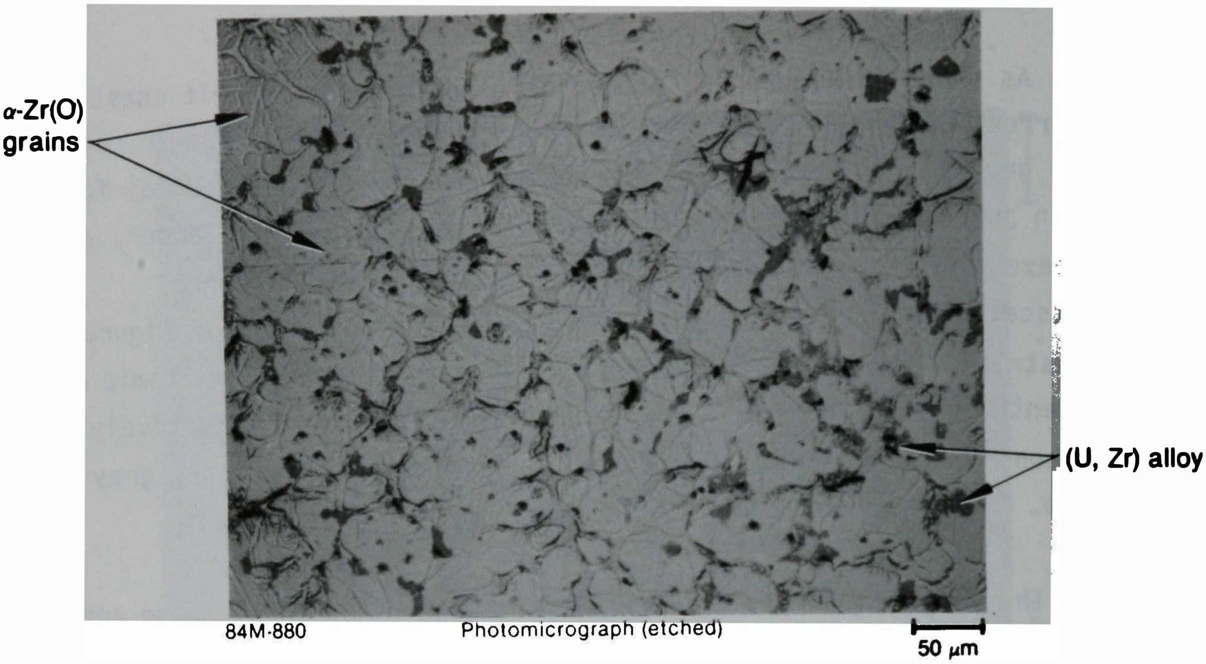

Photomicrograph (etched)

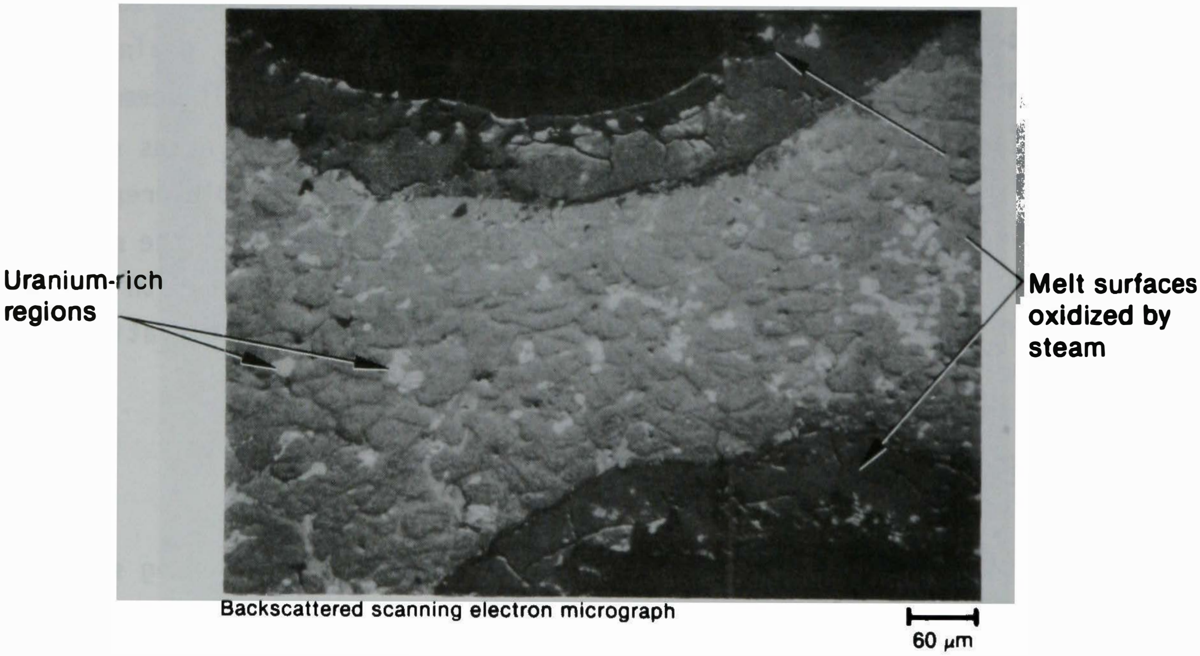

Backscattered scanning electron micrograph

Figure 16. Metallographic (top) and SEM (bottom) images of liquefied material structures in Particle 1A.

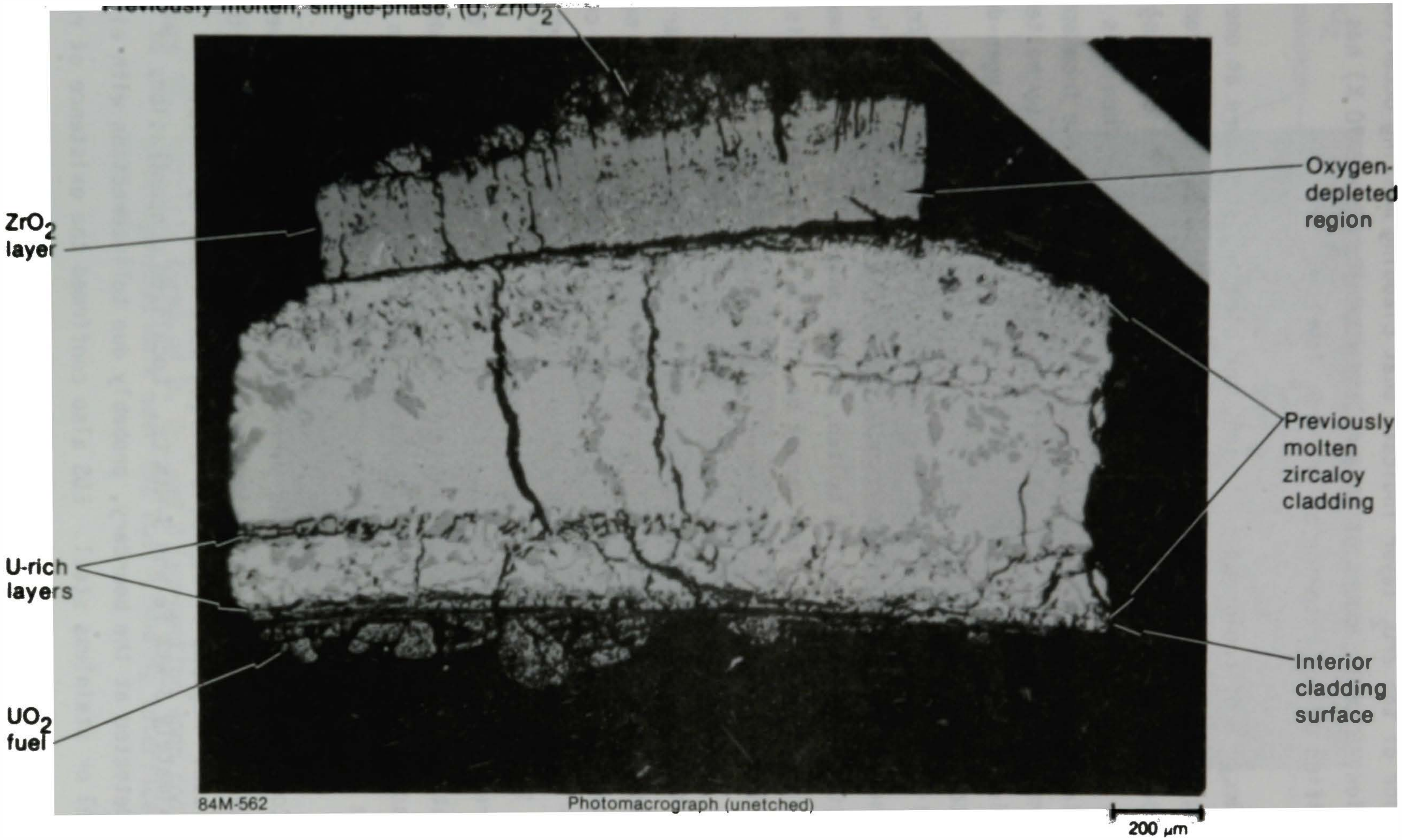

Figure 17. Particle 1E, cladding fragment with adherent fuel and once-molten mixed ceramic.

interior of the ZrO_2 layer indicate that cladding melting occurred. In addition, a small amount of once-molten $(U,Zr)O_2$ ($T > 2870$ K) has solidified on the exterior of the ZrO_2 layer.

Because of prolonged oxidation, the cladding structure at one point during the TMI-2 transient consisted of the following layers (from the outside inward): ZrO_2, α-Zr(O), large β-Zr grains at the cladding center, $\alpha\text{-Zr(O)}_b$, (U,Zr) alloy, $\alpha\text{-Zr(O)}_a$, and the UO_2. Then this cladding structure melted, which accelerated oxygen uptake from both the UO_2 and external ZrO_2. For a brief time, UO_2 dissolution by molten cladding must have proceeded rapidly. Upon cooldown, the oxygen-depleted, hypostoichiometric portion of the ZrO_2 decomposed into ZrO_2 and metallic stringers of α-Zr(O). Meanwhile, the heterogeneous (U,Zr,O) melt near the fuel interface transformed into α-Zr(O), (U,Zr) alloy, and $(U,Zr)O_2$. The timing of the molten, single-phase $(U,Zr)O_2$ attachment to the exterior ZrO_2 surface cannot be directly inferred from this scenario.

Semiquantitative elemental analysis by EDS was performed near the cladding-fuel interface to determine compositions of the various melt components shown on the top of Figure 18. [Higher atomic number compounds appear brighter in this backscattered electron image.] No uranium was found inside the α-Zr(O) and ZrO_2 regions. The (U,Zr) alloy was measured to be approximately 83-wt% U and 17-wt% Zr. Neglecting oxygen, the outer $(U,Zr)O_2$ band was found to be 32-wt% U and 68-wt% Zr, while the band adjacent to the UO_2 was 33-wt% U and 67-wt% Zr. The uranium dot map at the bottom of Figure 17 confirms these local measurements.

Considerable analysis was performed on the external ZrO_2 layer shown in Figure 19. EDS investigations were focused on the cladding-ZrO_2 interface. Regions of adjacent α-Zr(O) were found to contain approximately 3-wt% Fe and 3-wt% Cr. Localized concentrations of Al were also detected at the boundary, probably due to interaction with either Inconel or stainless steel. EDS also confirmed the existence of radially

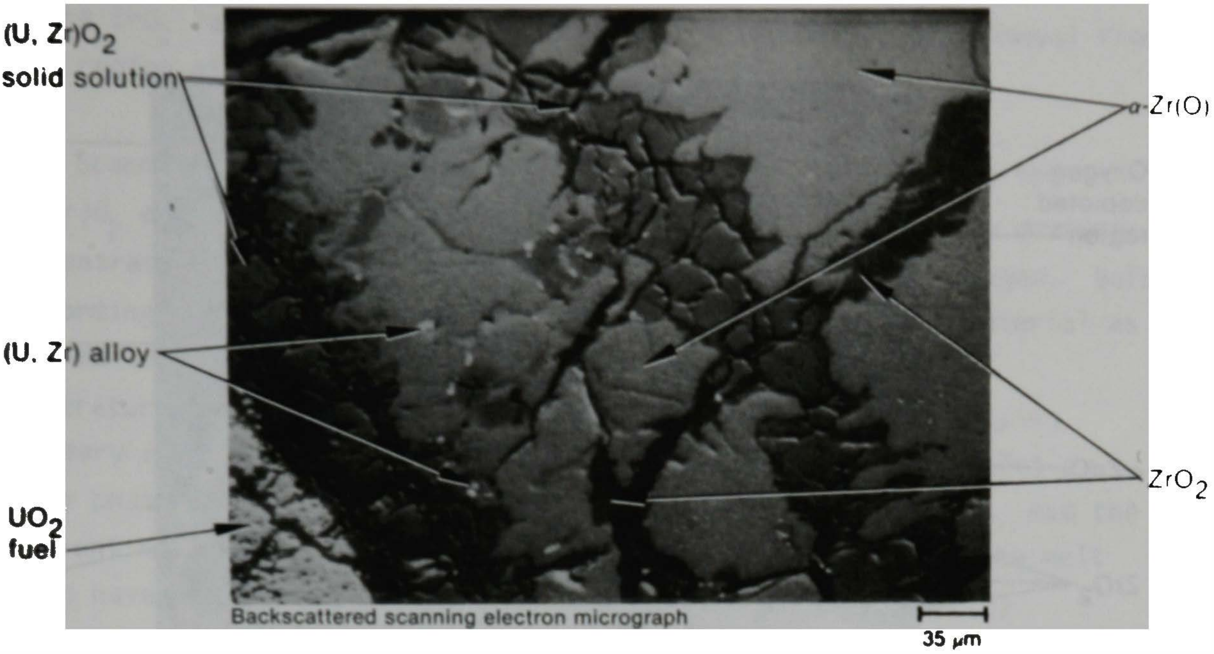

Figure 18. Multiple forms of U, Zr, and O segregation upon cooldown of a heterogeneous melt near the fuel-cladding interface in Particle 1E.

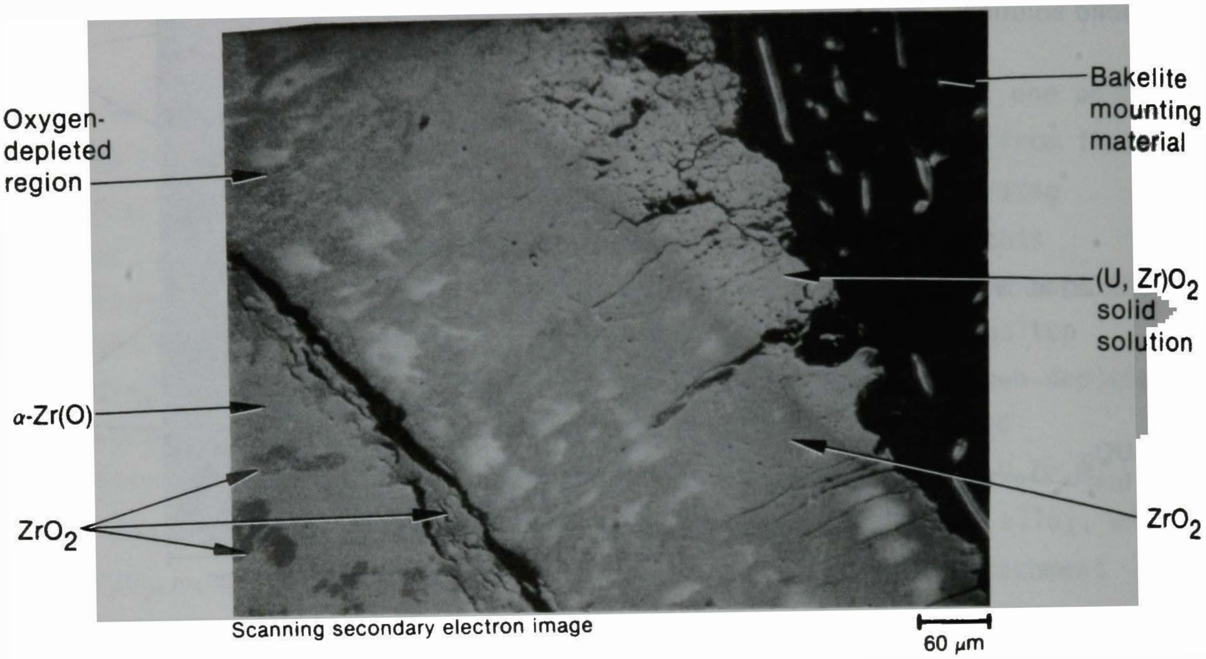

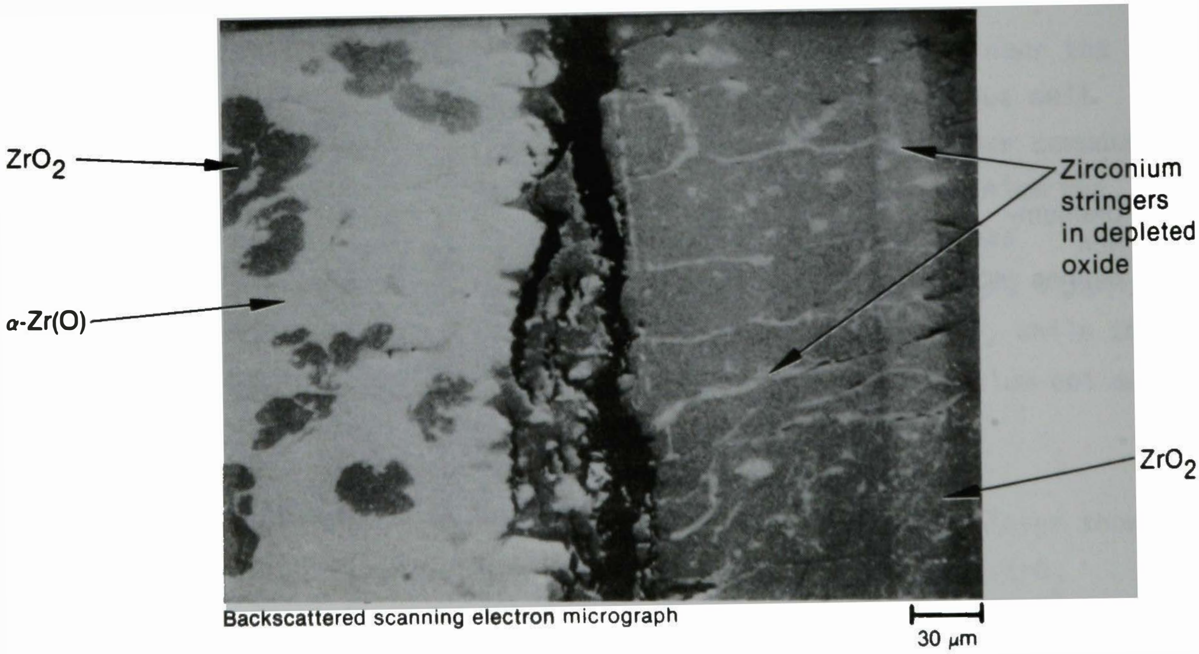

Figure 19. SEM images of zircaloy/ZrO_2 interface on Particle 1E, with adherent once-molten ceramic on exterior ZrO_2 surface.

oriented stringers containing Zr [probably α-Zr(O)] in the interior half of the ZrO_2 layer, which again represents accelerated oxygen removal from this region after cladding melting.

Scanning Auger spectroscopy (SAS) was used to characterize the $(U,Zr)O_2$ attached to the outer ZrO_2 surface. SAS can precisely measure concentrations of all elemental species present, especially oxygen. Before performing SAS, a preliminary identification of the adherent material as a once-molten, single-phase solid solution of UO_2 and ZrO_2 (peak temperature >2870 K) had been deduced metallographically. Applying standard Zr and UO_2 etches failed to expose the α-Zr(O) and (U,Zr) alloy phases formed during cooling of a metallic (U,Zr,O) melt. Had the adherent melt been partially metallic at the time of contact, the melt would have begun reducing the ZrO_2 immediately--creating α-Zr(O) stringers on cooldown at the outer ZrO_2 surface like those found on the interior half. Equivalently, a gradually changing ratio of ZrO_2 to α-Zr(O) would occur across the ZrO_2-melt interface. Nevertheless, because the metallographic interpretations had not been confirmed in this specific context, Auger spectroscopy was performed (after calibration to suitable standards) to supply oxygen concentration data on this portion of the particle.

Regions 15 μm in diameter were sequentially measured from the middle of the ZrO_2 layer to the exterior of the attached melt at two separate locations. The only evidence of oxygen depletion was found on the interior half of the ZrO_2, from reaction with molten cladding. The outer ZrO_2 layer and adherent mixed ceramic are uniform stoichiometric dioxides within measurement uncertainties (±2 at. % for primary constituents). While no oxygen gradient was detected near the ZrO_2-$(U,Zr)O_2$ interface, some diffusional inward migration of U did occur. However, this region of continuous U concentration change was restricted to a 50-μm-thick band centered at the visual demarcation on Figure 19, so most of the adherent melt and outer ZrO_2 layer were not affected by this process.

Although perturbed somewhat near the ZrO_2 boundary, the U and Zr concentrations were both consistently close to 17-at. % throughout the mixed oxide. [These values convert to 61-wt% U, 23-wt% Zr, and 16-wt% O, or, equivalently, 69-wt% UO_2 and 31-wt% ZrO_2.] Consequently, the minimum melting point of this ceramic solid solution was very nearly 2870 K, approaching the 3120 K melting point of pure UO_2. Trace amounts of Fe, Cr, and Al were also detected, as would be expected in a UO_2-ZrO_2 ceramic melt.

In addition, the scanning Auger investigations found one isolated deposit of Sb fission product in the mixed oxide. Approximately 2-at. % U was also found throughout the ZrO_2 layer, with 1-at. % U extending well into the cladding matrix. This widespread U content cannot be attributed to diffusion from the mixed oxide, so it presumably originated in UO_2. Redistribution during sample grinding is one possible explanation. However, this U probably diffused from dissolved UO_2 through the molten cladding to enter the ZrO_2 at the same period when the ZrO_2 was being reduced. Subsequent SEM/EDS investigations confirm the second explanation, as widely distributed pockets of (U,Zr) alloy were found at high resolution in the ZrO_2 layer.

3.2.3 Particle 1H

Particle 1H (Figure 20) has a very porous (foamy) appearance and is a quench-frozen agglomerate of two distinctly different types of material. Single-phase, large-grained, pore-free fragments have been surrounded by a fine-grained, porous, multiphase melt. After metallography, it was initially thought that this particle was probably composed of fuel pellet pieces coated by a quenched melt, which would have accounted for the apparent chemical dissolution of the single-phase ceramic blocks. However, SEM/EDS investigations quickly established that Particle 1H would require a much more complicated explanation.

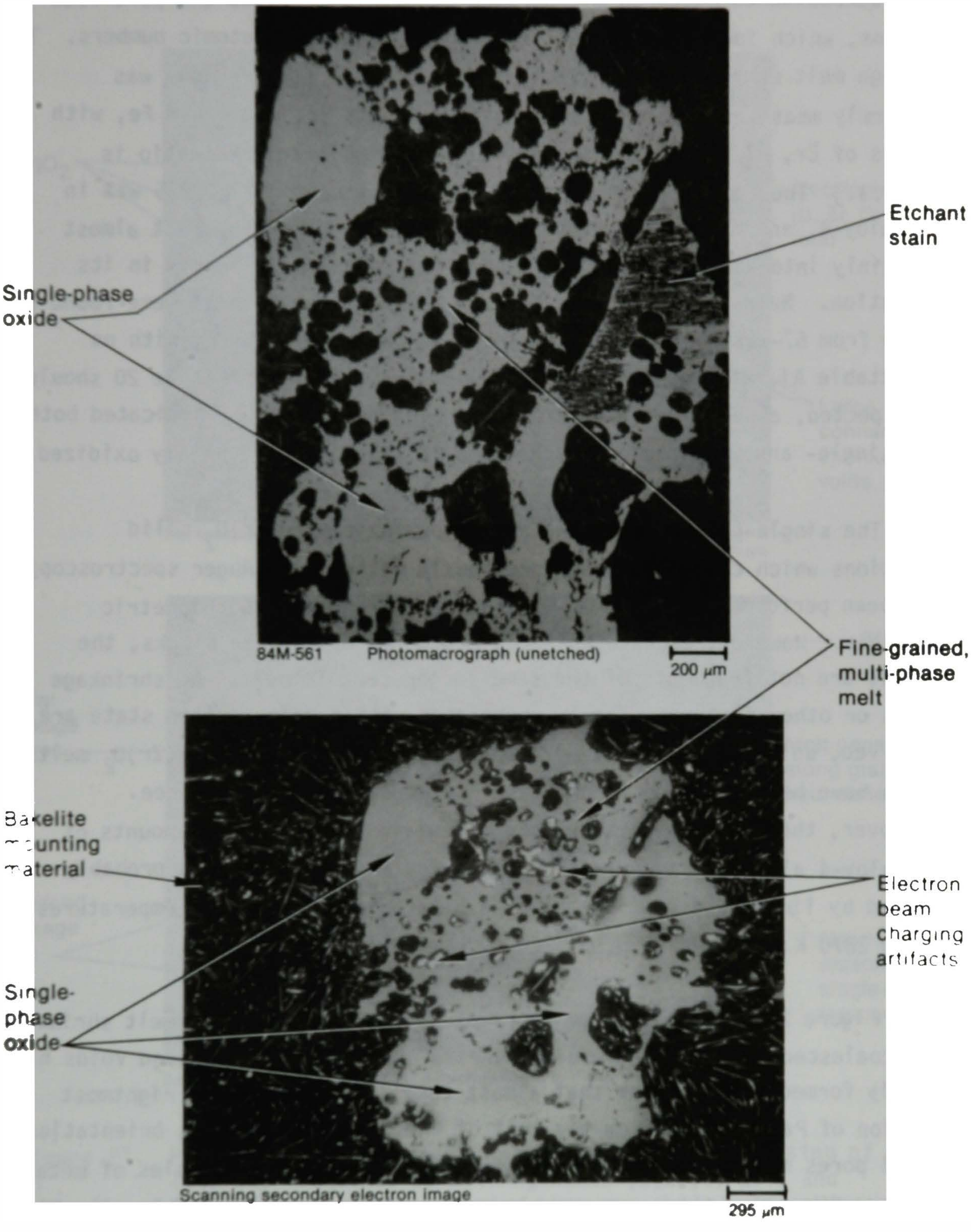

Figure 20. Metallographic (top) and SEM (bottom) images of Particle 1H, an agglomerate of single-phase fragments and porous, multiphase melt.

As shown in Figure 21, very little gray-level contrast was found on the backscattered electron micrographs between the porous and pore-free regions, which indicates overall similarity in average atomic numbers. The average melt composition (neglecting oxygen) over four regions was uniformly measured by EDS to be 68-wt% U, 28-wt% Zr, and 4-wt% Fe, with traces of Cr, Al, and Ni. [The approximate atomic Zr:U:Fe ratio is 13:12:3.] The Fe content is much higher than the nominal 0.225 wt% in Zircaloy-4, and Ni should not normally be detected, so the melt almost certainly interacted with Inconel and/or stainless steel early in its evolution. Meanwhile, the single-phase, pore-free "islands" were found to range from 67-wt% U and 33-wt% Zr to 59-wt% U and 41-wt% Zr, with no detectable Al, Ni, Fe, and Cr. Thus, little contrast on Figure 20 should be expected, especially since etching during metallography indicated both the single- and multiphase components of Particle 1H are highly oxidized.

The single-phase blocks are almost definitely $(U,Zr)O_2$ solid solutions which could have been previously molten. No Auger spectroscopy has been performed thus far to confirm that they are stoichiometric dioxides. However, because the Zr:U ratio varies between blocks, the blocks are not fragments of the same larger ceramic melt. No shrinkage pores or other features clearly associated with a prior molten state are observed, unlike the ceramic melt on Particle 1E; however, $(U,Zr)O_2$ melts which have been superheated and fast cooled can appear pore-free. Moreover, these pieces of mixed oxide contain no detectable amounts of Zircaloy-4 alloying ingredients. Each single-phase block was probably formed by liquid-state oxidation of a heterogeneous melt at temperatures below 2870 K.

Figure 21 illustrates how porosity from cooling-induced melt shrinkage has coalesced into larger void features. For example, elongated voids have nearly formed a full crack that almost totally separates the rightmost portion of Particle 1H from the rest of the structure at this orientation. Small pores may be nucleated at temperature by miniscule bubbles of metal vapor. Tiny unoxidized, presumably condensed deposits of Fe, Cr, Al, Ni, and Sn can occasionally be found within the smallest pores. These deposits might be more common on unetched samples.

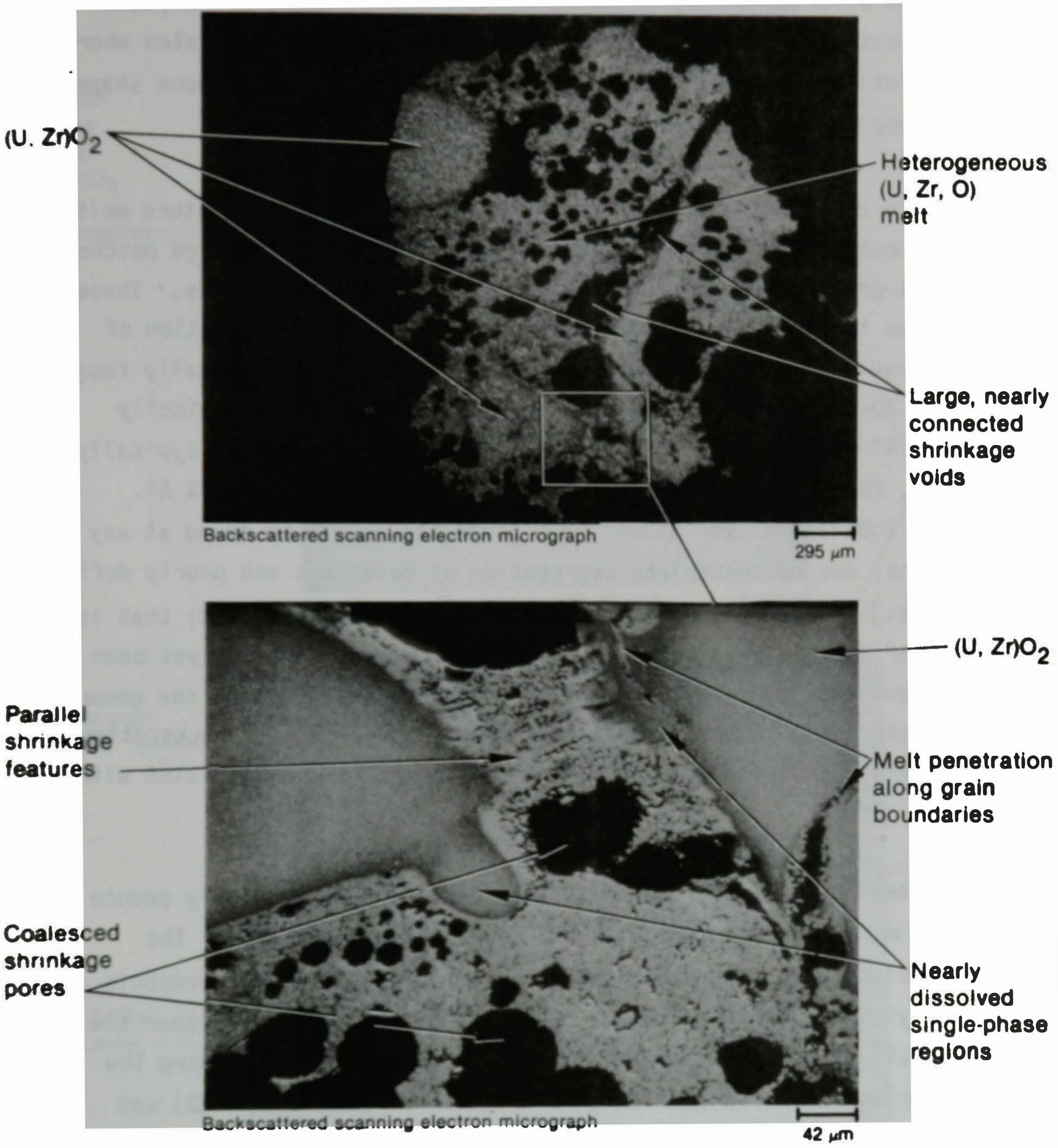

Figure 21. Particle 1H--macroscopic and closeup views of wetting of $(U,Zr)O_2$ fragments by heterogeneous (U,Zr,O) melt and formation of shrinkage voids upon quenching. The absence of contrast reflects compositional similarities.

Figure 21 also shows that the $(U,Zr)O_2$ blocks are wetted equally by the melt, regardless of their compositions. The highly magnified view proves that dissolution of the mixed oxide occurred along all exposed surfaces, not just at grain boundaries. Two regions are indicated where the dissolution process is almost complete. The rounded, bulbous shape of one of these regions indicates incipient melting ($T > 2870$ K).

Figure 22 illustrates that the fine-grained, room-temperature melt structure consists of three phases: bright-gray grains, mottled patches, and a dark-gray phase sandwiched between the grains and patches. These phases have irregular boundaries, as quenching prevented formation of distinct equilibrium structures. The bright grains were typically found by EDS to be 70-wt% U, and 30-wt% Zr; the mottled patches are typically 54-wt% U, 41-wt% Zr, and 5-wt% Fe; and the dark-gray phase is typically 26-wt% Fe, 25-wt% U, 17-wt% Cr, 12-wt% Ni, 11-wt% Zr, and 9-wt% Al. [However, substantial variations from these values can be found at any given point, due to incomplete segregation of materials and poorly defined boundaries.] No phase consisting primarily of Zr was detected; that is, no α-Zr(O) nor ZrO_2 is apparent. Oxygen concentrations have not yet been measured but etching results, metallographic appearances, and the general lack of contrast between the melt and mixed oxide blocks on backscattered SEM images all indicate that the three phases are nearly saturated with oxygen.

The melt behavior at temperature is difficult to precisely deduce from the phase make-up after quenching. Because the dissolution of the $(U,Zr)O_2$ blocks had progressed quite far, some of the melt represents previously dissolved mixed oxide. Thus, it is not certain whether the melt was initially homogeneous or heterogeneous. The melt surrounding the $(U,Zr)O_2$ blocks and along block grain boundaries (see Figure 22) was measured to be 54-wt% U, 42-wt% Zr, and 4-wt% Fe--nearly identical to the average mottled patch composition--so the patch phase was likely responsible for attacking the mixed oxide fragments. Because Fe forms a complex eutectic system with U,Zr, and O, the dissolution mechanism was

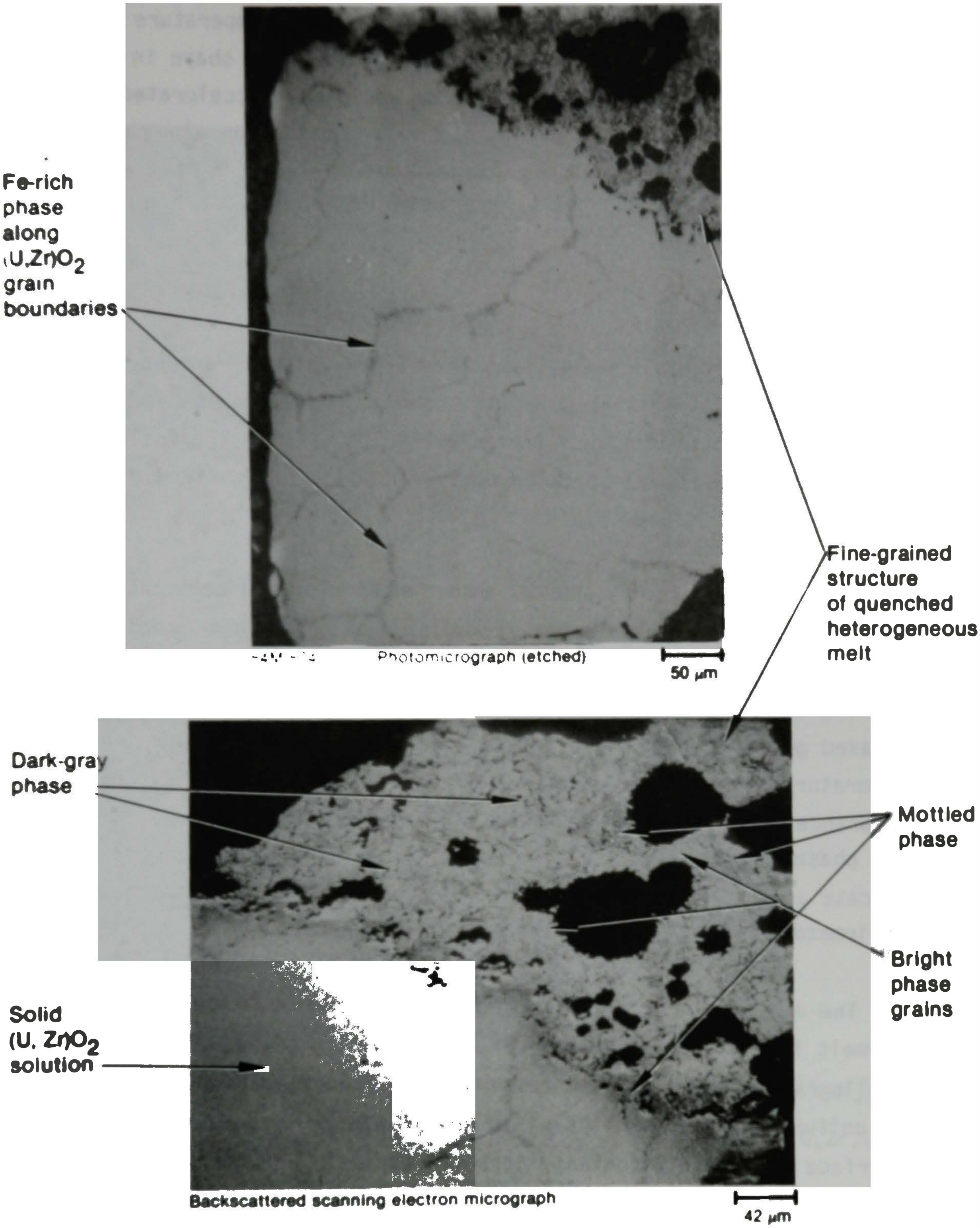

Figure 22. Particle 1H--metallographic (top) and SEM (bottom) images of (U,Zr)O$_2$ dissolution along grain boundaries by superheated, iron-rich melt phase.

probably eutectic decomposition. However, the melt temperature may also have been higher than 2873 K--as suggested by the bulb shape in Figure 21--in which case $(U,Zr)O_2$ melting would have accelerated the dissolution process. In any event, the melt penetration along grain boundaries in Figures 21 and 22 confirms that the $(U,Zr)O_2$ had definitely solidified before melt contact occurred.

3.2.4 Particle 6D

Particle 6D (Figure A-19) is a large fuel pellet fragment with a tiny portion of (U,Zr,O) melt attached at one end. As shown in Figure 23, the fracture surfaces appear very irregular for UO_2, while the fuel matrix has a distinctly unusual speckled cast. The external surface of the particle appears "glazed."

Figure 24 shows that the UO_2 experienced elevated temperatures, since considerable porosity has accumulated at grain boundaries. This phenomenon is also observed in fuel operated at standard reactor conditions, after burnups of approximately 15 to 20 GWd/t. The extent of equiaxed grain growth is negligible, indicating that the peak fuel temperature did not exceed 1900 K. Figure 23 also shows the fuel appearance after etching to expose grain boundaries, whereupon a second fuel phase emerged. This second phase is most likely U_4O_9, which would indicate an oxidizing environment while the fuel was at temperature; but confirmatory Auger and MOLE measurements have not yet been made.

The adherent melt was also of major interest. As shown in Figure 25, the melt is composed of smooth ceramic-appearing grains exhibiting only one metallographic phase at room temperature. The EDS-derived melt composition was uniformly measured at 66-wt% U and 34-wt% Zr, except near the fuel interface where the U content increased abruptly. No traces of Fe, Cr, Sn, or other alloying ingredients were found. Therefore, the melt is probably stoichiometric $(U,Zr)O_2$. The grain texture and composition suggest that the mixed oxide represents a metallic (U,Zr,O) melt oxidized as a liquid

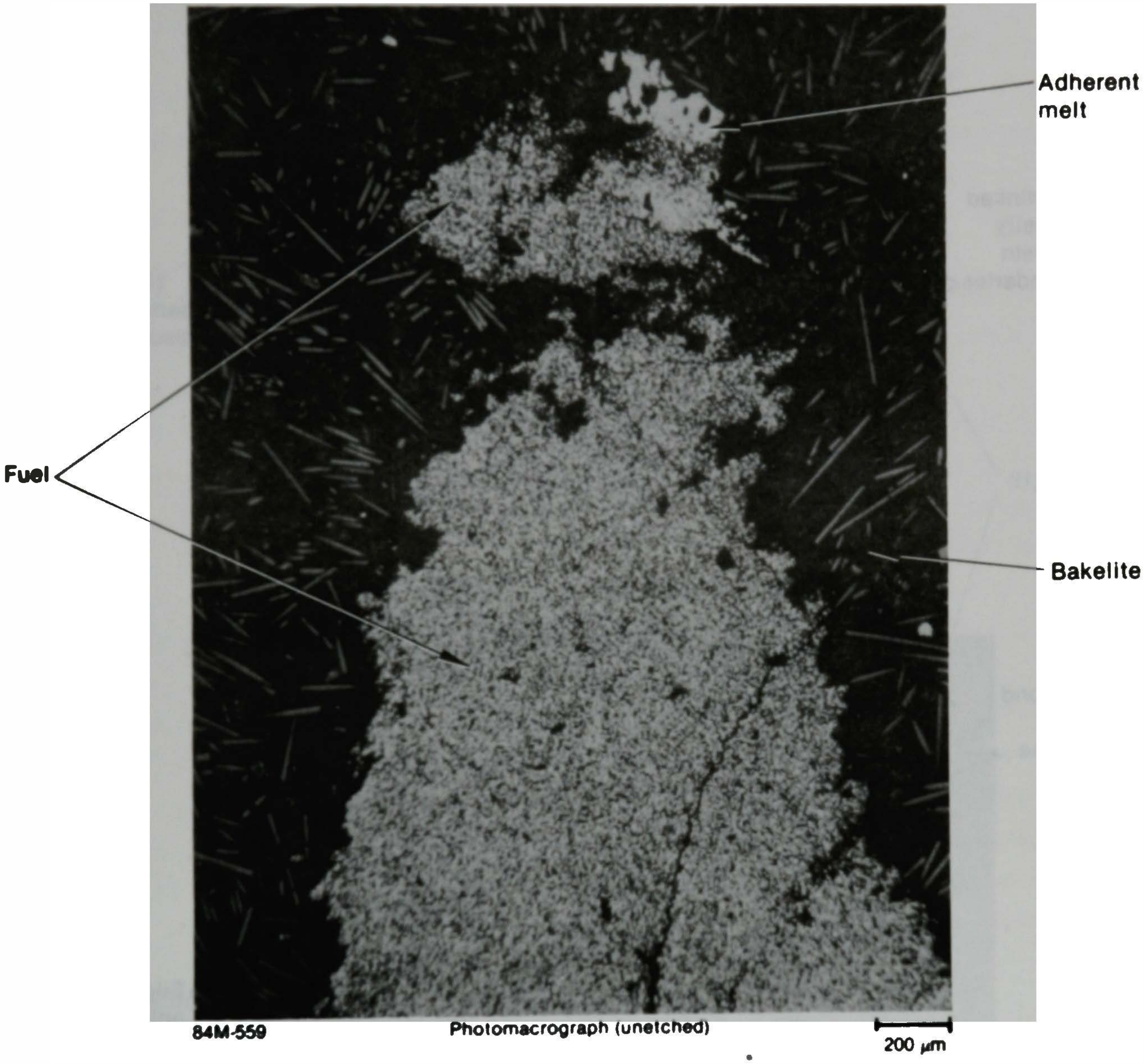

Figure 23. Particle 6D, possibly oxidized fuel with adherent (U,Zr,O) melt.

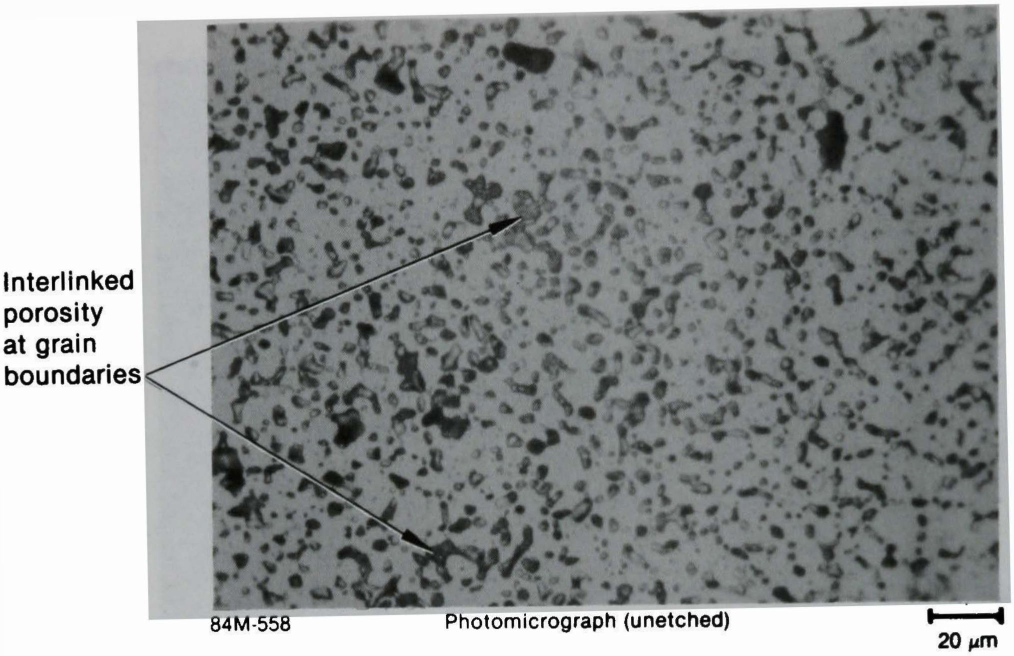

84M-558 Photomicrograph (unetched)

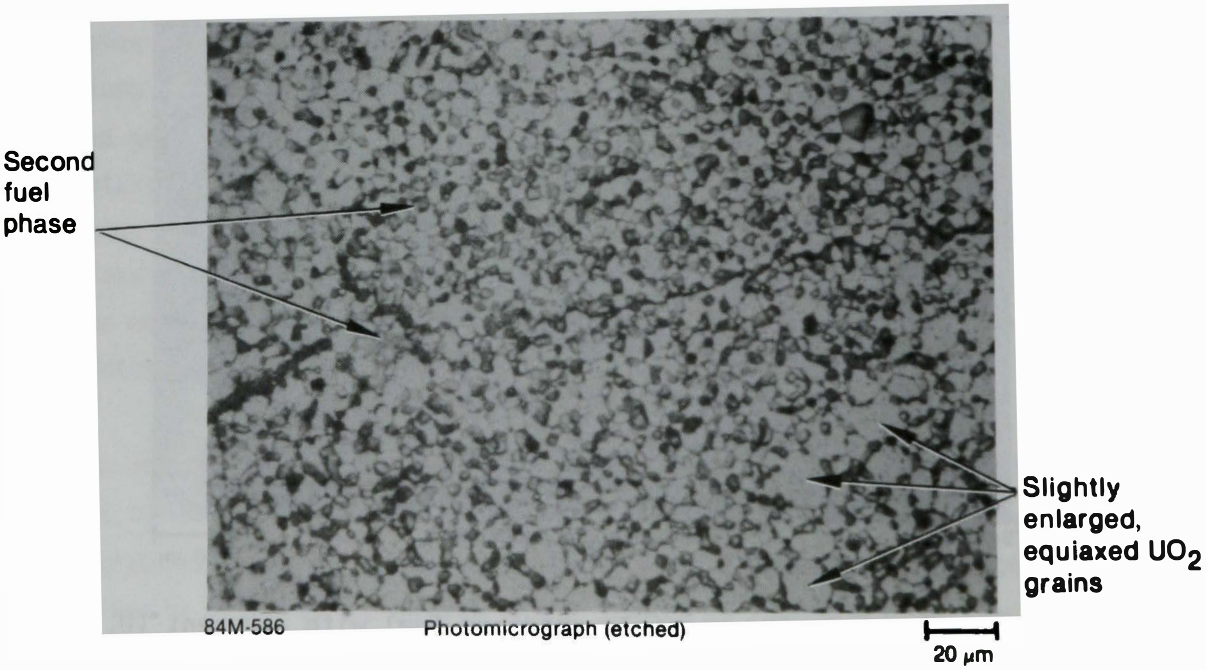

84M-586 Photomicrograph (etched)

Figure 24. Typical fuel grain structure of Particle 6D before and after etching.

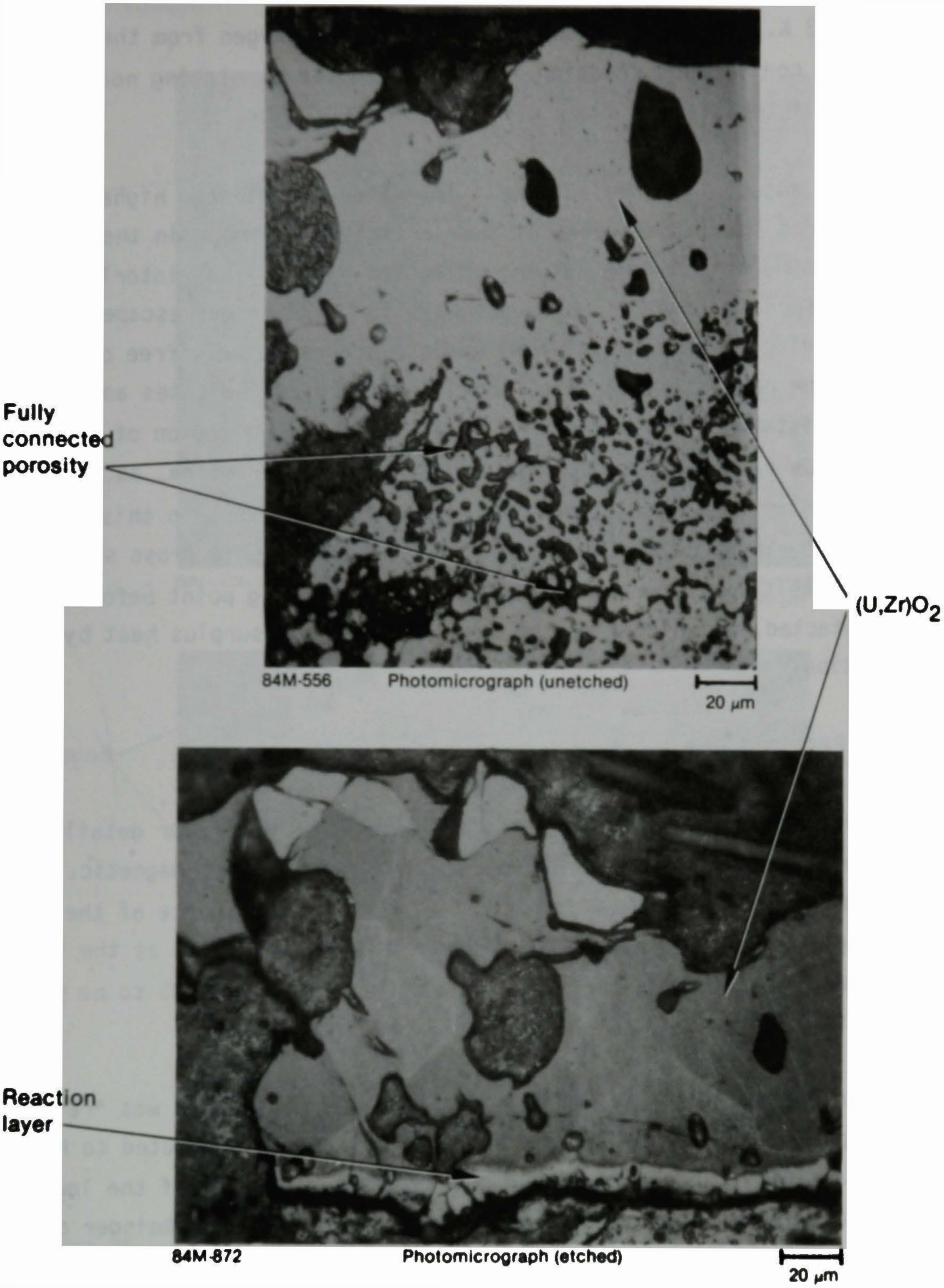

Figure 25. Highly magnified metallographic images of melt-fuel interface on Particle 6D.

below 2873 K. The melt evidently absorbed some oxygen from the fuel, because a conspicuous reaction layer was exposed by etching near the fuel-melt interface, as shown in the bottom of Figure 25.

Fuel adjacent to the fuel-melt interface experienced higher temperatures than other areas of the particle. As shown in the upper photomicrograph in Figure 25, the collected porosity has interlinked near the interface to form connected pathways for fission gas escape. Correspondingly, interfacial fuel regions are relatively free of individual pores. The backscattered image shown in Figure 26 indicates another such region exists well below the interface. This second region of brighter, less porous fuel is also a consequence of melt interaction, as confirmed by the zirconium x-ray image shown in Figure 26. However, in this second case, the melt is below the plane of the metallographic cross section. The metallic melt was superheated well above its melting point before the fuel was contacted, at which time the fuel received the surplus heat by conduction.

3.2.5 Particle 6F

Particle 6F (Figure A-21a) was originally selected for detailed characterization after it was found to be partially ferromagnetic. Despite the complicated overall appearance in Figure 27, the source of the ferromagnetic nature of Particle 6F was readily identified as the three large metallic ingots. These ingots were determined by EDS to be 96-wt% Ni and 4-wt% Fe, with a small additional amount of Sn.

The process whereby Inconel-718 (initially 52-wt% Ni) was "refined" to nearly pure Ni is not definitely known but is probably related to higher oxygen affinity for the Fe and Cr constituents. Because of the low extent of oxidation, the Ni-rich melt presumably contacted the remainder of Particle 6F late in its evolution, penetrating along large pores and solidifying from heat losses to a cooler matrix. Thus, the temperature of the oxidized particle portions was almost certainly well below 1725 K (the melting point of Ni) when the Ni-rich melt arrived.

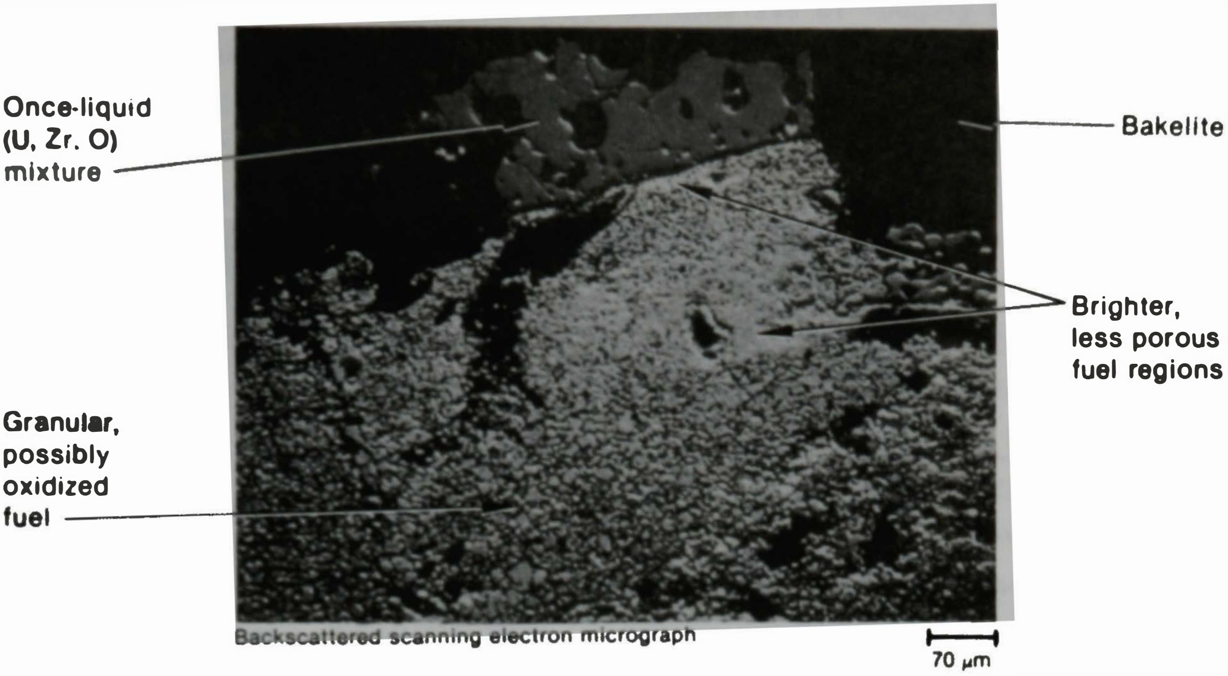

Backscattered scanning electron micrograph

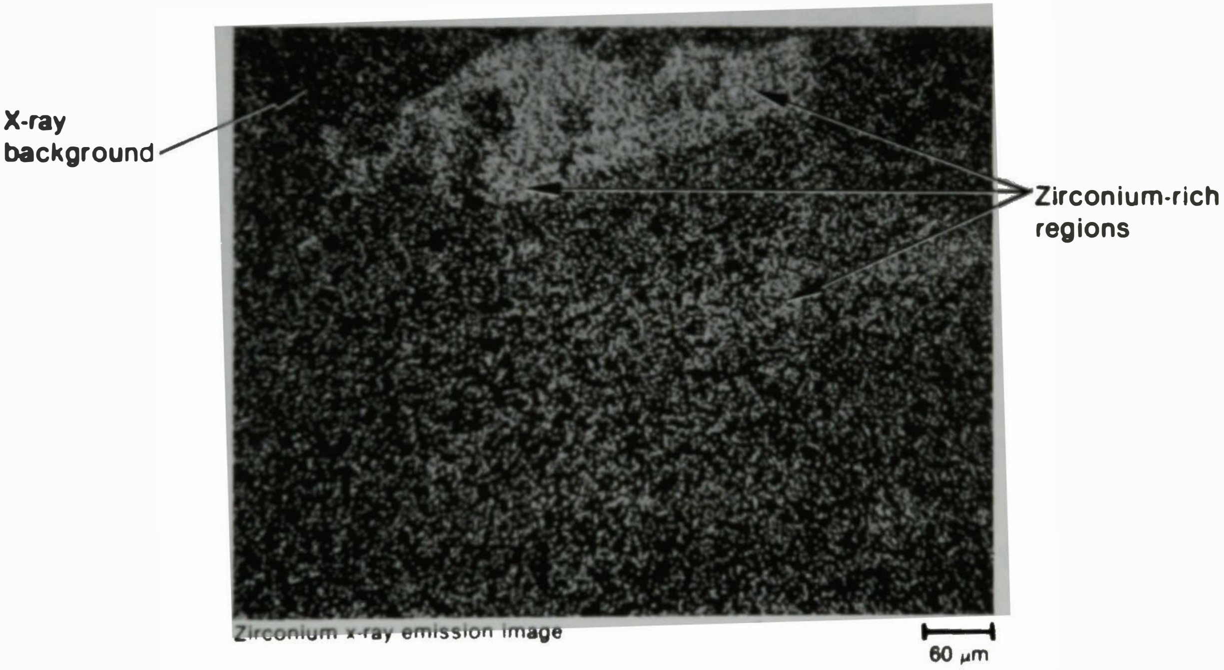

Zirconium x-ray emission image

Figure 26. Particle 6D--relationship between less porous fuel regions and zirconium content.

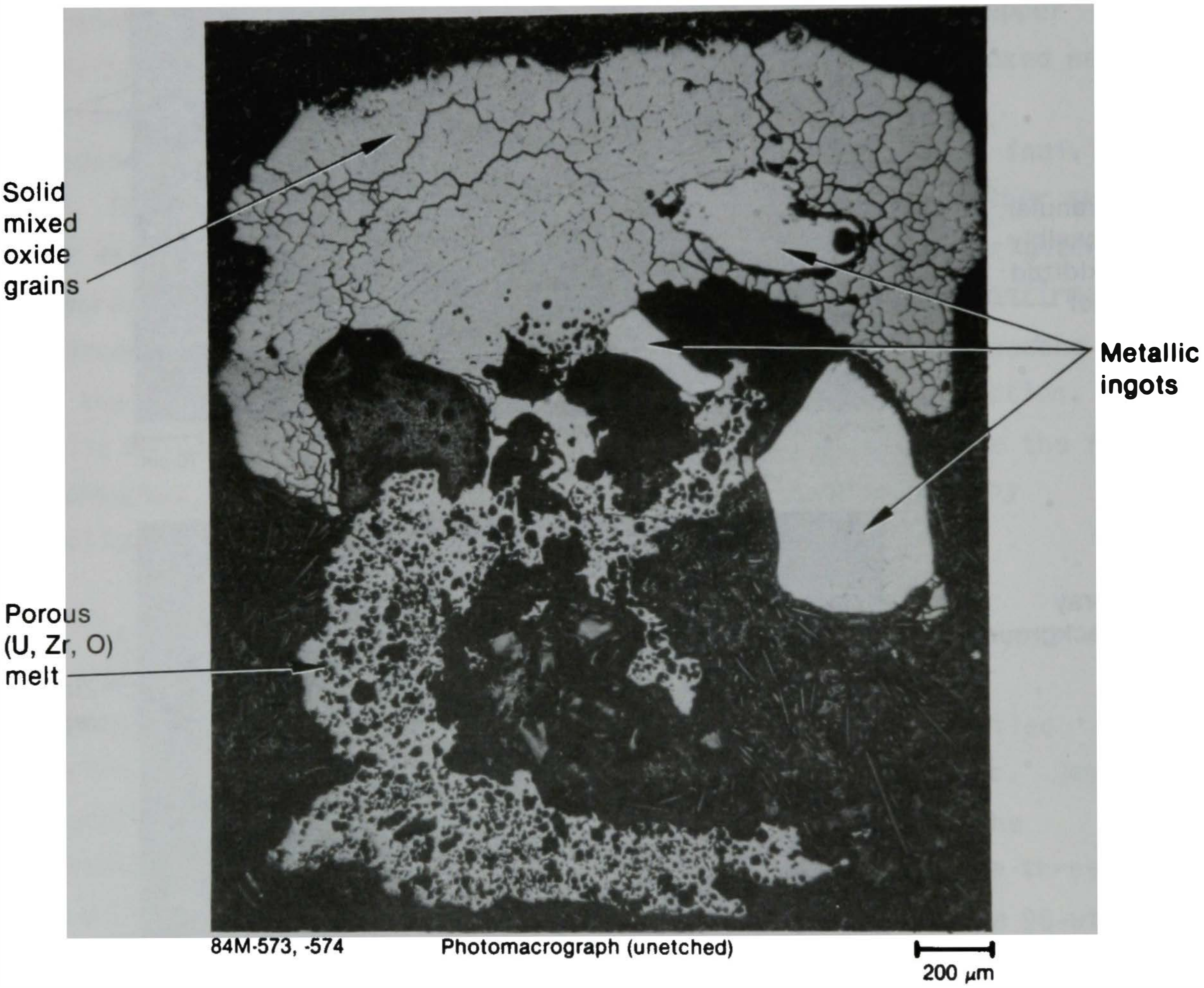

Figure 27. Particle 6F, an agglomerate of porous and solid (U,Zr,O) melts, both highly oxidized, and metallic, ferromagnetic ingots.

In addition to the ingots, Particle 6F consists of roughly equal amounts of porous and solid (U,Zr,O) materials at the cross-sectional orientation studied. The granular, relatively pore-free structure evidently solidified before contact with the porous melt. The metallographic appearances and etching behavior of both types of (U,Zr,O) material suggest a high degree of oxidation.

The backscattered electron micrograph at the top of Figure 28 illustrates major differences in average atomic number of Particle 6F. The composition of the solid-grained structure was determined by EDS to be approximately 32-wt% U and 68-wt% Zr (neglecting oxygen), while the porous heterogeneous melt ranged between 50- and 60-wt% U and 45- to 35-wt% Zr, with the remaining 5-wt% composed of varying amounts of Fe, Cr, Ni, and Al. [Fe and Cr tend to dominate the impurities, which suggests prior interaction with stainless steel.] Therefore, most of the gray-level contrast between the solid-grained and porous structures in Figure 27 is due to a marked difference in U content. However, the porous melt could conceivably be less oxidized, because oxygen concentrations have not yet been measured by Auger spectroscopy.

The large solid grains are almost definitely $(U,Zr)O_2$. The mixed oxide contains no detectable alloying impurities, as with comparable pore-free $(U,Zr)O_2$ in Particles 1H and 6D, and unlike the adherent mixed oxide in Particle 1E. The preponderance of shrinkage pores and the absence of grains in the bright, irregularly shaped melt confirms solidification on cooling.

Figure 27 also shows several bright regions lacking both shrinkage pores and grain structure. These regions represent diffusion bonding between the solid $(U,Zr)O_2$ and the partially liquid heterogeneous melt. Much of this diffusional interaction was caused by melt-solid contact outside the plane of study, because the interfacial area at this orientation is quite small. One such bonding region is shown in closer detail at the bottom of Figure 28. Note the absence of diffusional exchange with the Ni ingots, which confirms that the heterogeneous melt had cooled and solidified before the Ni-rich melt arrived. Note also that the heterogeneous melt has not attacked the $(U,Zr)O_2$ grain boundaries.

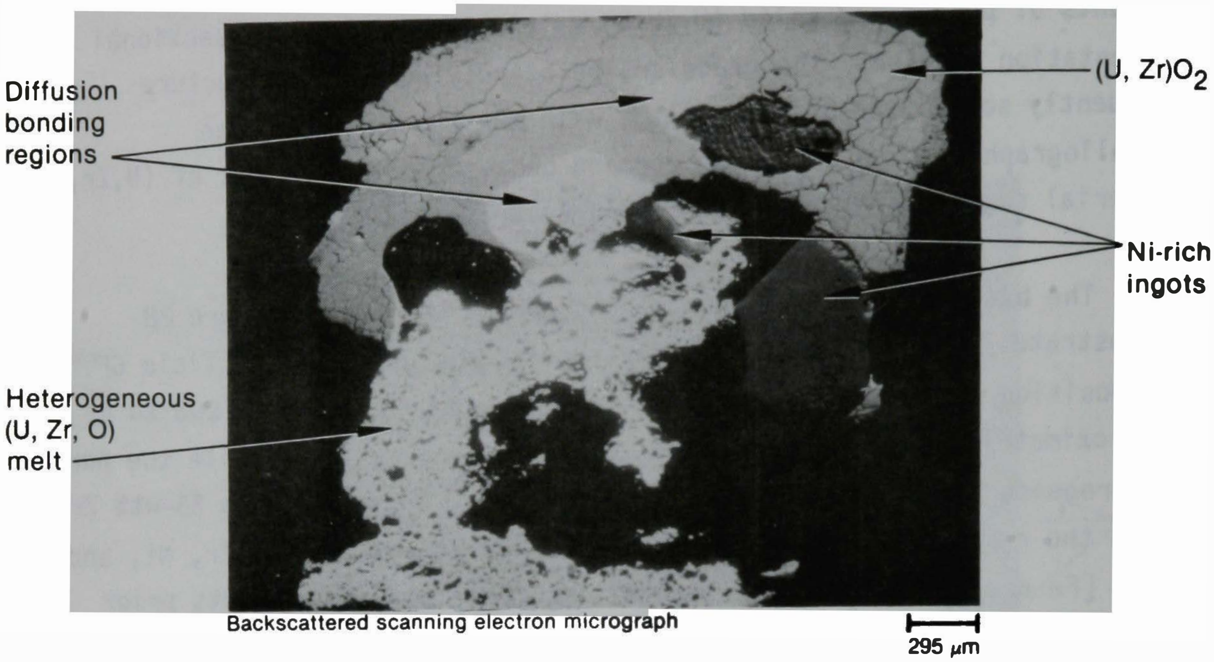

Backscattered scanning electron micrograph

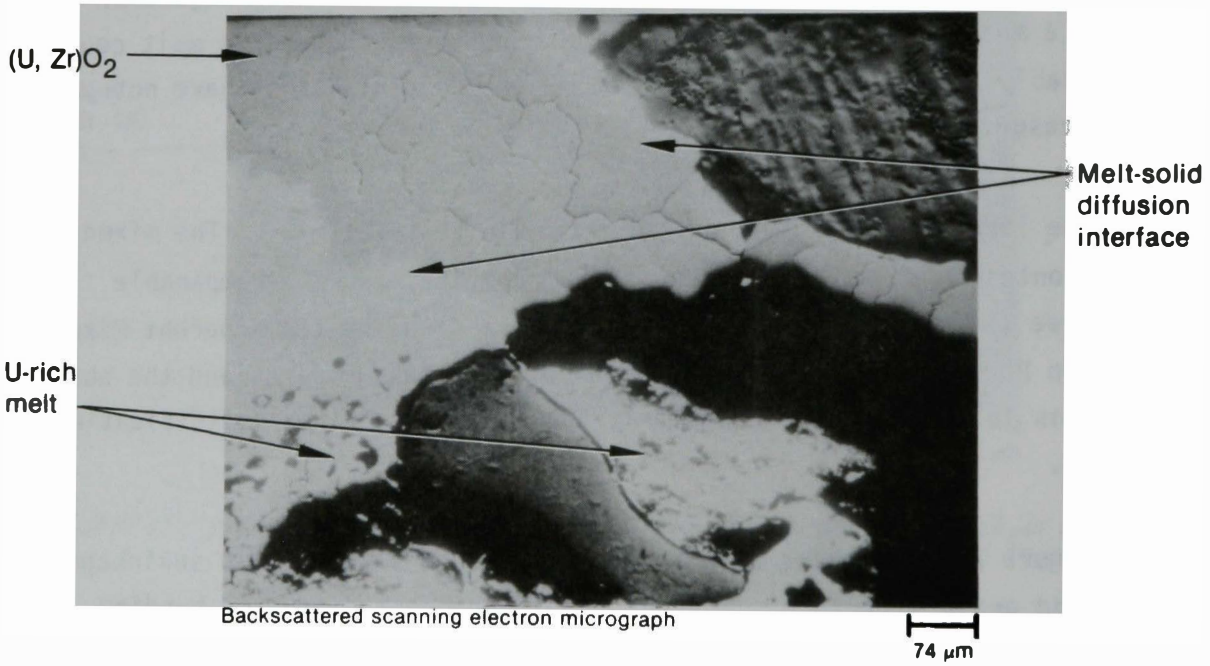

Backscattered scanning electron micrograph

Figure 28. Pronounced compositional differences in Particle 6F, with regions of low average atomic number appearing darkest.

Figure 29 provides close-up views of the room-temperature heterogeneous melt microstructure. Metallic ingots present during initial metallography were evidently dislodged or dissolved by etching, so the small inclusions only appear in the upper image. Two phases are apparent on the lower backscattered electron micrograph: the (U,Zr,O) matrix and the dark-gray stringers. The matrix composition at this position is approximately 57-wt% U, 38-wt% Zr, 4-wt% Fe, and 1-wt% Ni (plus a substantial concentration of oxygen), while the stringers here are composed of 34-wt% Cr, 33-wt% Fe, 17-wt% Al, and 16-wt% Ni.

Based on the metallographic appearance and immunity to etchants, the matrix seems to be mostly $(U,Zr)O_2$. Much of this mixed oxide would have been in the form of $(U,Zr)O_{2-x}$ at temperature, so the metallic inclusions could conceivably be (U,Zr) alloy that emerged as the $(U,Zr)O_{2-x}$ dissociated upon cooling. However, it is more likely that the inclusions were relatively inert metals like Sn or Ni whose low oxygen affinity prevented incorporation within the matrix.

Despite incomplete understanding of the melt structure, the makeup of Particle 6F resembles Particle 1H in that a porous melt has contacted previously solidified $(U,Zr)O_2$. Nevertheless, the melt-solid interactions in these two cases are very different. In Particle 6F the two materials have bonded by diffusion, whereas in Particle 1H the melt has dissolved substantial amounts of the $(U,Zr)O_2$. The heterogeneous melt composition is quite similar in the two particles, although the U content of the mixed oxide is lower in Particle 6F. Therefore, the major distinction between the two situations seems to be the melt temperature. The heterogeneous melt in Particle 1H was apparently liquefied and superheated above the $(U,Zr)O_2$ melting point--thus accounting for the extensive grain boundary penetration and dissolution of the solid mixed oxide. By comparison, the heterogeneous melt in Particle 6F was evidently a viscous slurry at a temperature well below 2873 K, so only diffusional interactions occurred where the two materials were in contact.

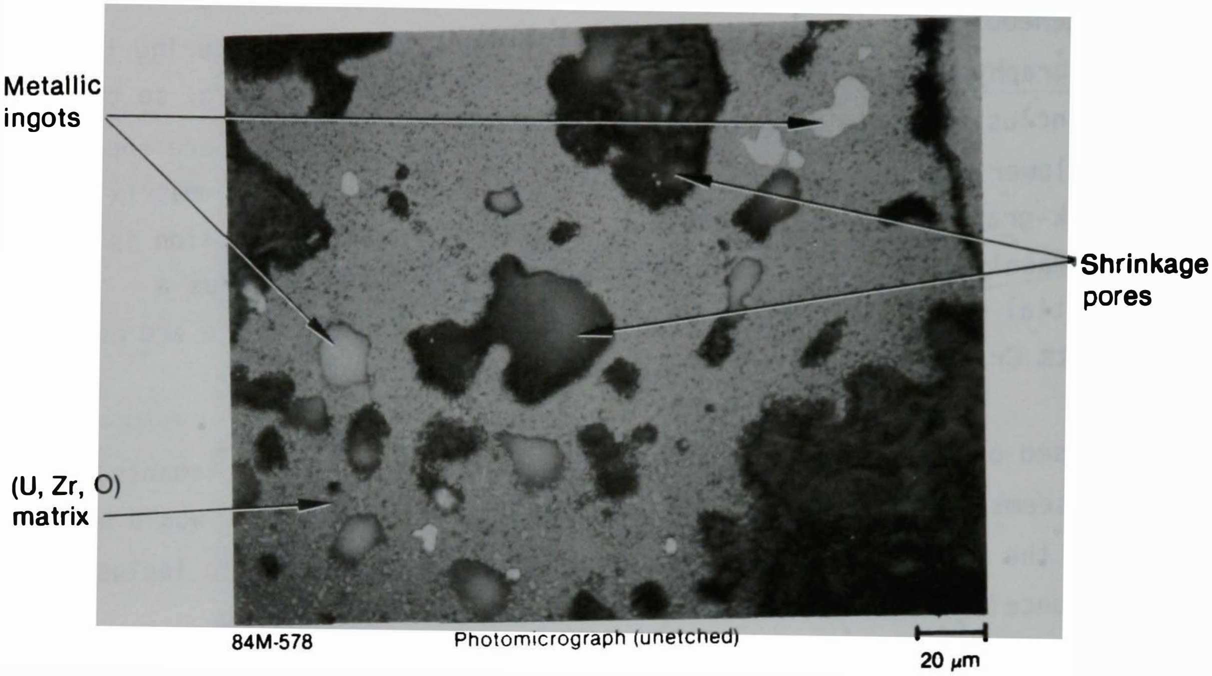

Photomicrograph (unetched)

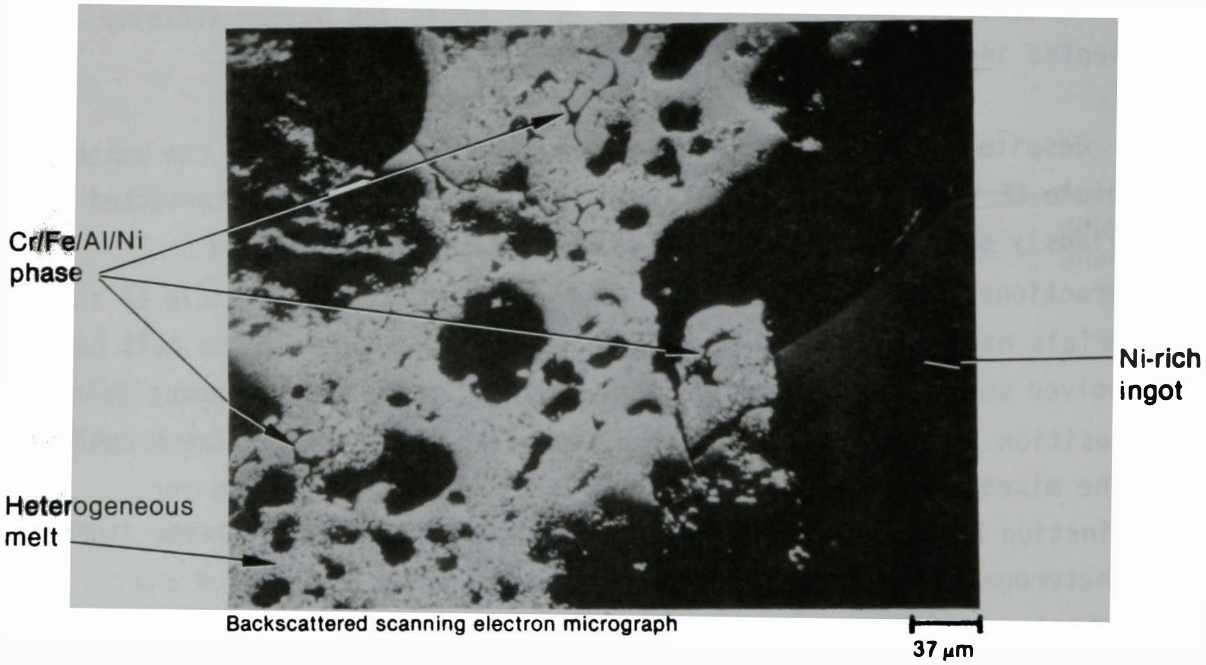

Backscattered scanning electron micrograph

Figure 29. Metallographic (top) and SEM (bottom) images of heterogeneous melt structure in Particle 6F.

4. FERROMAGNETIC MATERIAL ANALYSIS

The quantity of ferromagnetic material present in the sieve fractions was measured for Sample 6 (obtained 22 in. into the debris bed at core location E9). This analysis was performed by placing a small (2-lb pull) magnet in a small (100-mL) pyrex beaker and then placing the beaker in contact with each sieve fraction. After stirring the beaker in the sample material, the magnet, beaker, and attached magnetic material were removed and placed in a container. The magnet then was removed from the beaker, allowing the magnetic material to drop into the container. No material adhered to the beaker after removing the magnet; therefore, it was assumed that all material in the container had a ferromagnetic component. Figure 30 is a photograph of a magnetic particle (Particle 6F) which was removed for radiochemical analysis. The rough exterior is characteristic of most ferromagnetic particles.

The quantity of ferromagnetic material in each of the individual size fractions of Sample 6 is listed in Table 2. From these data, the quantity of ferromagnetic material present can be divided into two size groups. The first group (297 to 4000 µm) contains 95% of the total weight, and the second group (74 to 297 µm) contains 5%. For this sample, the conditions forming these materials produced no large (i.e., >4000 µm) chunks of material that were demonstratively magnetic.

Stainless steel was the principal core material containing iron. There were approximately 1.6 x 10^3 kg of stainless steel (~68% Fe) present in the core area.[14] This compares with the total core material mass of 1.25 x 10^5 kg. The fraction of ferromagnetic material found in the sample was approximately 0.9%, and the form was magnetite.

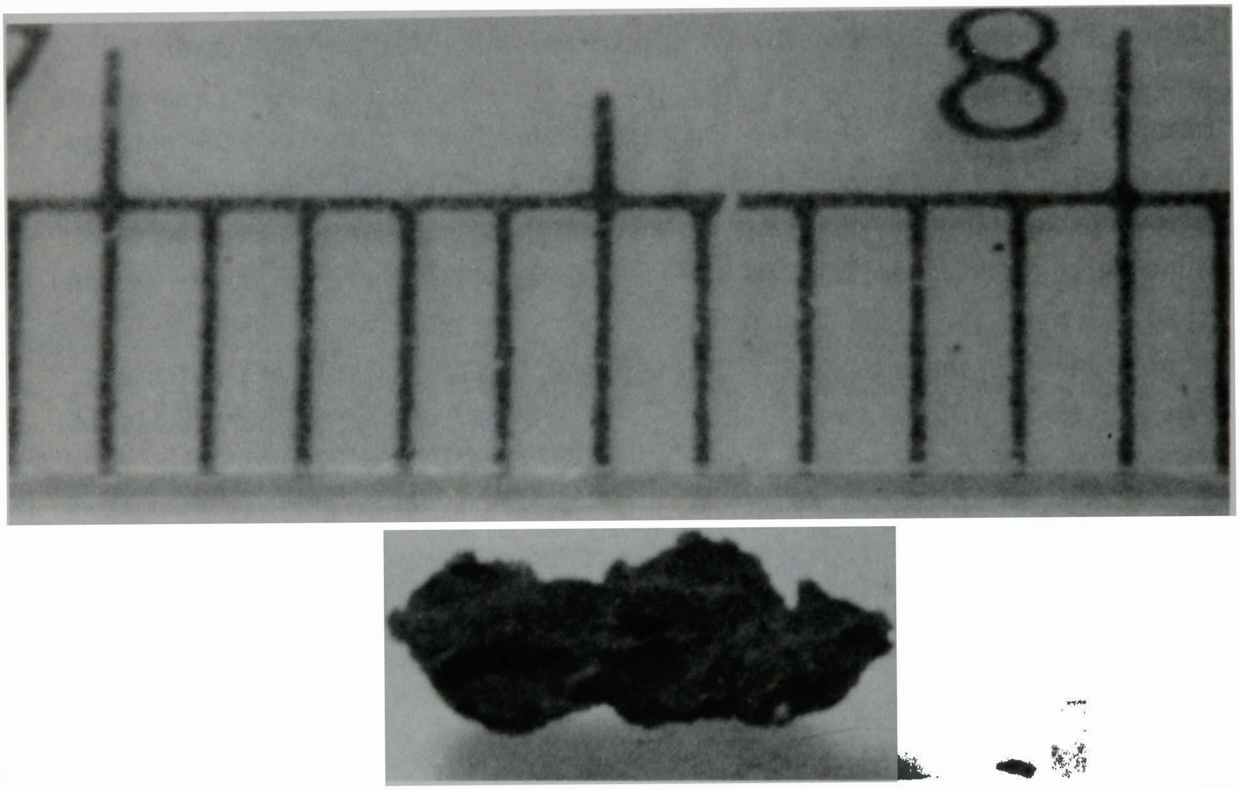

84-199-4-6

Figure 30. Ferromagnetic particle (Particle 6F) removed from Sample 6.

5. PYROPHORICITY TESTS

Pyrophoricity (i.e., pilot ignition) tests were performed on selected core debris materials to evaluate potential safety hazards to core recovery operations. To demonstrate the procedure, preliminary tests were performed on zirconium hydride powder using a small Tesla coil (Fisher Scientific Company Model BD10) rated at 5×10^4 V. The ignition of this powder was recorded by both video tape and still photography before beginning the actual core debris pyrophoricity tests. An additional method used to produce higher temperatures (a propane torch) also was tested on the same type powder before beginning the actual pyrophoricity tests.

The sieve fractions from Samples 3 and 6 were chosen for pyrophoricity testing. Tests were performed on material removed from all size fractions from 30 to 4000 µm. The quantity of material used for each test rangeo from 0.25 to 0.5 g. A small quantity of material was used in oroer to maintain radiation exposure to personnel within reasonable limits. Tests were performed under both dry and wet conditions. The dry condition was attained by warming the material for approximately 30 min at 100°C. The wet condition was attained by adding two drops of water to the material.

Tests were performed on individual wet and dry portions of the samples. The same portion was used for both analyses. Figure 31 shows a portion of Sample 3 being exposed to the Tesla coil to determine if pilot ignition occurs. No visible pilot ignition was observed for any size fraction of either sample. Figure 32 shows a particle from one of the samples being heated with a propane torch. One particle of what appeared to be core structural material from each of the two samples was exposed to the propane torch, and no pilot ignition was observed for either particle.

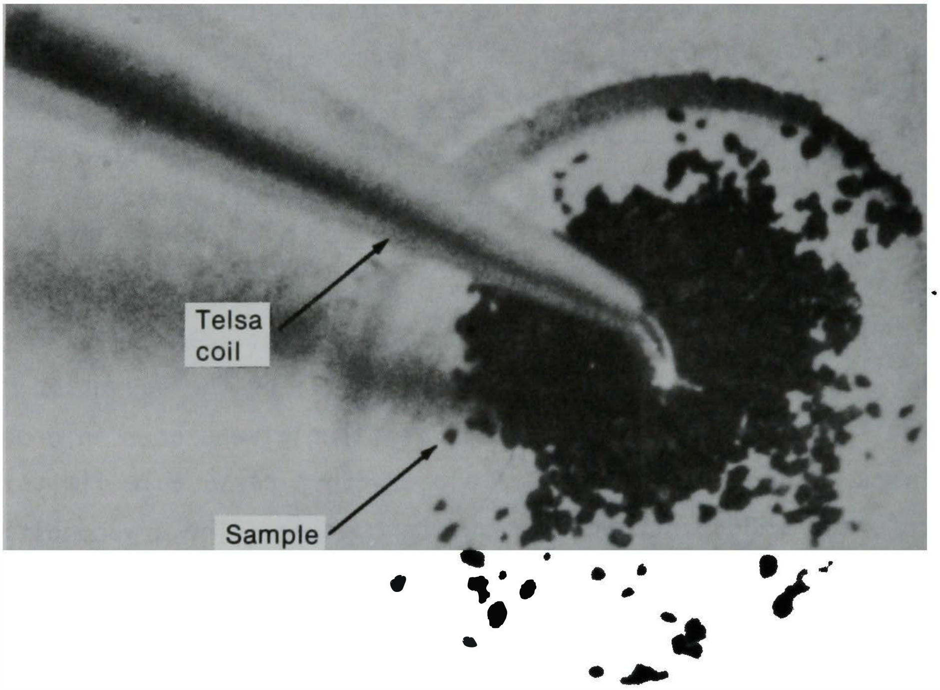

Figure 31. Tesla coil pilot ignition test on material removed from the 149-297 μm size fraction from Sample 3, using a Fisher Scientific Company Model BD10 Tesla coil rated at 5 x 10^4 V maximum.

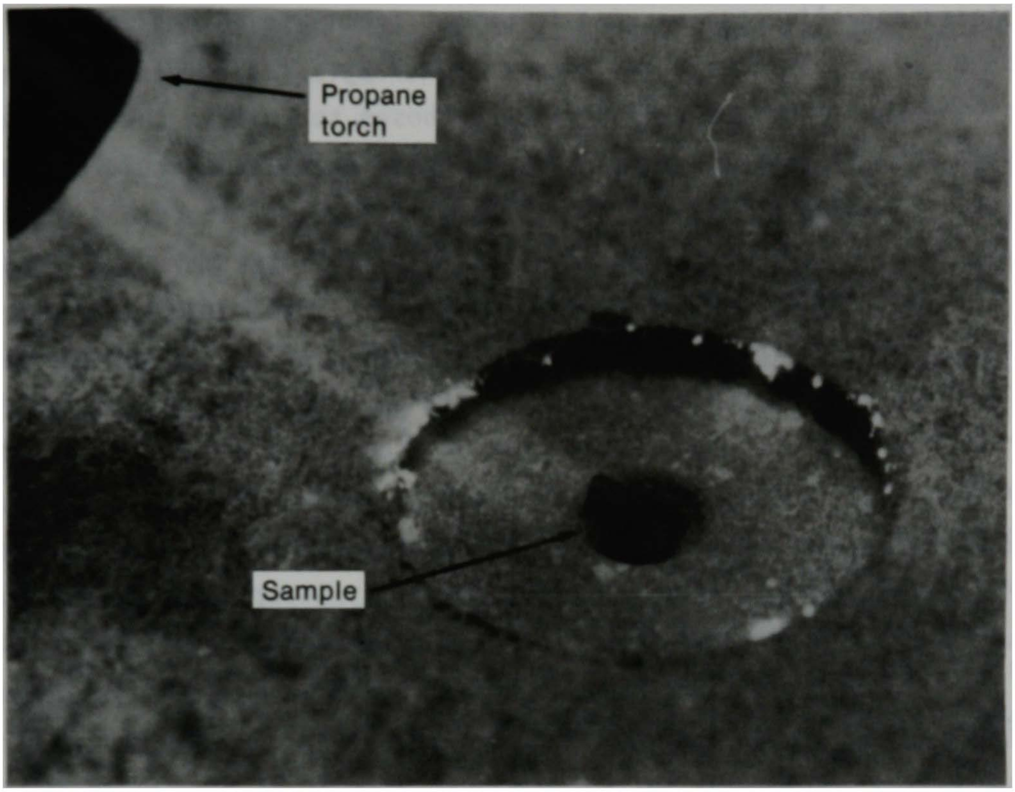

Figure 32. Propane torch pilot ignition test on a particle of core structural material.

6. GAMMA SPECTRAL MEASUREMENTS

Fragmented pieces from the large particles and aliquots from the smaller particle size fractions were removed from each of the five bulk samples for quantitative gamma spectrometry analysis. The fragmented pieces and aliquots, ranging in weight from 5 to 50 mg, were analyzed after being placed in individual 1-cm-diameter by 5-cm-long sealed aluminum cylinders. Aluminum cylinders were chosen to contain the materials for this analysis so subsequent fissile/fertile analysis could be performed without transferring the materials.

The results were corrected for gamma-ray attenuation caused by the mass of the material analyzed. This correction was performed using a calculation comparing high and low energy gamma rays from specific radionuclides. The correction factor accounting for effect of mass attenuation in the gross analysis was calculated from ^{144}Ce data, primarily. The only radionuclide for which significant mass attenuation was expected was ^{155}Eu, and its uncertainty is approximately 20%. Data for ^{241}Am are not included in this report because an effective correction factor is quite uncertain due to the low energy (∼60 keV) of gamma rays emitted from this radionuclide.

The following gamma-ray energies were used to determine the radionuclide concentration of each fragmented piece or aliquot: ^{60}Co (1332 keV), ^{106}Ru (622 keV), ^{110m}Ag (885 keV), ^{125}Sb (601 keV), ^{134}Cs (605 keV), ^{137}Cs (662 keV), ^{144}Ce (2185 keV), ^{154}Eu (1274 keV), and ^{155}Eu (80 keV).

The gamma spectrometry data for each of the five samples are tabulated by particle size fraction in Appendix B. Analysis of the data is given in Section 8.

7. FISSILE/FERTILE MATERIAL ANALYSIS

The fissile/fertile material analysis determined the fissile material ($^{235}U + ^{239}Pu$) and total fertile material (principally ^{238}U) content of the fragmented pieces and aliquots described in Section 6. The analysis was performed at the Coupled Fast Reactivity Measurement Facility (CFRMF) using delayed neutron analysis.[15]

The total fissile/fertile material content was measured by remotely exposing the individual 1- by 5-cm aluminum cylinders containing the pieces and aliquots to a fast spectrum neutron flux located in the central region of the core in CFRMF. The cylinder was then removed after a 1-min exposure, and the delayed neutrons being emitted were measured after a specific time (~40 s) using a ^{3}He detector in a hydrogen moderator.

To obtain the distribution between fissile and fertile material content, the cylinders containing the pieces and aliquots were then exposed to a thermal spectrum neutron flux, which causes only the ^{235}U and ^{239}Pu elements to fission and emit delayed neutrons. It was assumed that the quantity of ^{239}Pu was insignificant. Based on theoretical predictions discussed in Section 8, the ^{239}Pu content should be less than 0.2 wt%. However, a 5 to 8% bias may result. The fragmented pieces and aliquots were then analyzed using the ^{3}He detection system. The fertile material content was determined by subtracting the measured fissile material content from the total fissile/fertile material content, using appropriate calibrations.

Calibration standards were prepared from highly enriched uranium, depleted uranium, and light water reactor grade enriched uranium (~4.3 wt%). In addition, calibration standards of different weights (between 5 mg and 1 g) were prepared to correct the data for neutron attenuation caused by the mass of each fragmented piece or aliquot.

The measured fissile/fertile material data available at this time are presented in Appendix C. These data are discussed in Section 8.

8. DISCUSSION OF RESULTS

The following are discussed in this section: (a) particle size analysis of the core debris samples, (b) radionuclide concentrations of the individual size fractions, (c) fissile/fertile material content of specific particles and aliquots, and (d) core fission product inventory calculated using the ORIGEN-2 code.[16] The high temperature interactions of the debris material were discussed in Section 3.

The following preliminary observations concerning characteristics of the debris material can be made from the particle size data:

- There is no significant difference in particle size distribution between the H8 and E9 deep samples (Samples 3 and 6)
- Only about 0.3 wt% of the sample particles are smaller than 100 μm in size
- The E9 surface sample (Sample 4) and the E9 near surface sample (Sample 5) are similar in that they contain only large particles greater than 1000 μm size.

Particle size data were presented in Table 2 of Section 2. These data have been plotted to aid interpretation. Figure 33 is a frequency distribution histogram showing the weight fraction of particles within a size range relative to the average particle size of the range for Samples 1 and 3 (H8 surface and H8 deep).

The gamma spectrometry analysis of the fragmented pieces and aliquots can be used to estimate the fission product inventory remaining in the core debris bed. The gamma spectrometry results for all fragmented pieces and aliquots examined are summarized by particle size fraction in Tables 3 through 7. For particle size fractions where more than one particle was analyzed (i.e., >4000, 1680-4000, and 1000-1680 μm) the data are presented both as an average radionuclide concentration (μCi/g) and as

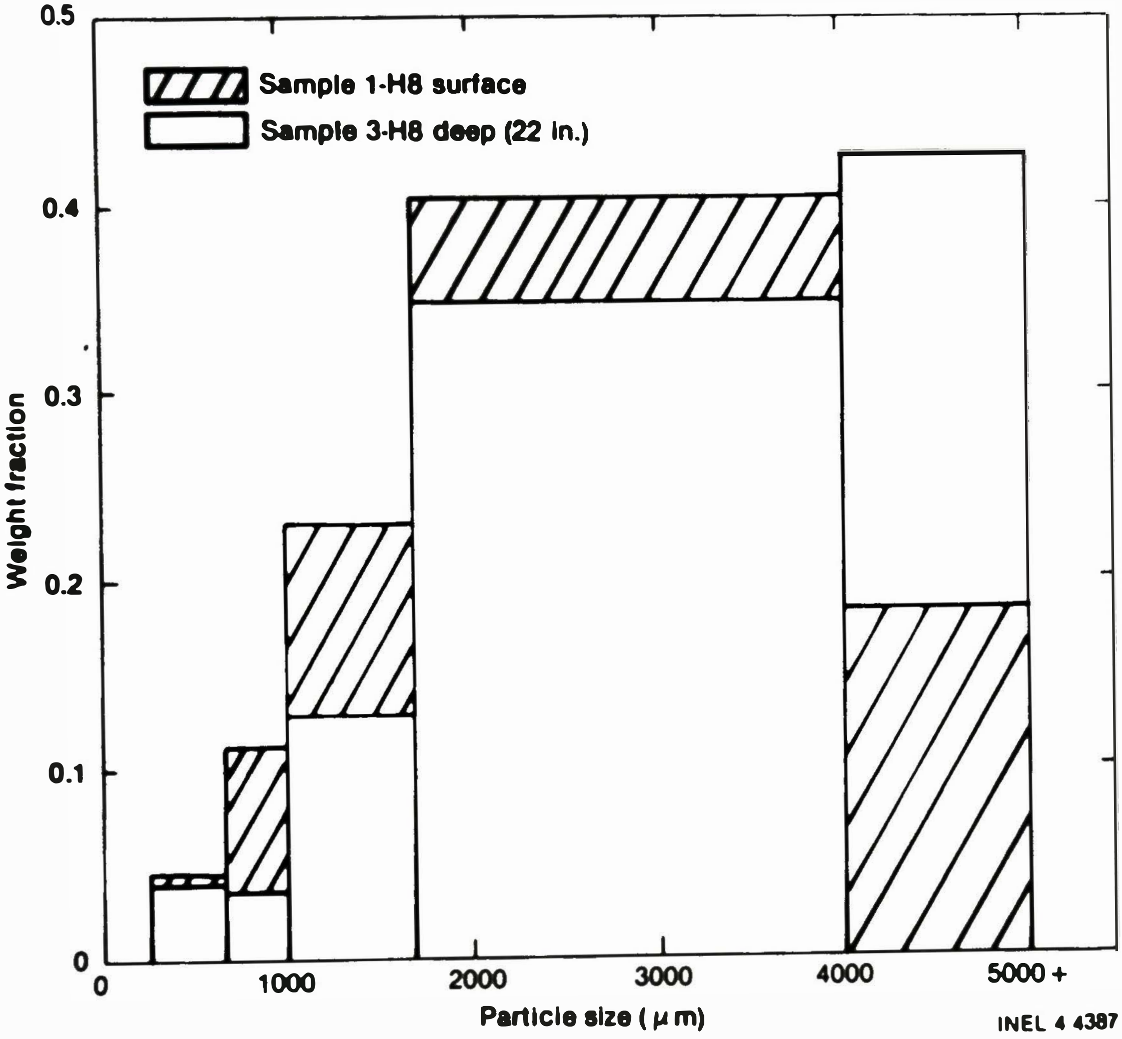

Figure 33. Frequency distribution histogram for Samples 1 and 3.

TABLE 3. RADIONUCLIDE CONCENTRATIONS AND RANGES FOR SAMPLE 1[a] (μCi/g)

	Particle Size Fraction (μm)					
	>4000[b]		1680-4000		1000-1680	
Radionuclide	Average	Range	Average	Range	Average	Range
^{60}Co	1.8 E+1	8.7 E+0 - 2.6 E+1	3.2 E+1	8.1 E+0 - 7.8 E+1	8.9 E+0	1.9 E+0 - 1.7 E+1
^{106}Ru	5.7 E+2	6.7 E+1 - 1.6 E+3	7.5 E+1	4.4 E+1 - 1.1 E+2	4.2 E+1	8.9 E+0 - 7.0 E+1
^{110m}Ag	ND[c]	--	ND	--	7.4 E+0[d]	--
^{125}Sb	6.3 E+1	1.4 E+1 - 1.2 E+2	1.8 E+1	1.5 E+1 - 1.8 E+1	7.2 E+2	1.1 E+0 - 2.2 E+3
^{134}Cs	2.6 E+1	3.7 E+0 - 7.6 E+1	7.3 E+1	6.3 E+0 - 1.1 E+2	2.4 E+1	3.1 E+0 - 6.3 E+1
^{137}Cs	5.4 E+2	6.7 E+1 - 1.3 E+3	1.3 E+3	1.1 E+2 - 2.0 E+3	4.3 E+2	5.5 E+1 - 1.1 E+3
^{144}Ce	2.1 E+3	1.7 E+2 - 3.8 E+3	2.5 E+3	2.2 E+3 - 3.1 E+3	9.4 E+2	0 - 2.5 E+3
^{154}Eu	3.3 E+1	8.0 E-1 - 5.9 E+1	4.1 E+1	3.0 E+1 - 5.7 E+1	1.8 E+1	9.8 E-1 - 4.8 E+1
^{155}Eu	6.8 E+1	1.2 E+1 - 1.6 E+2	1.0 E+2	9.5 E+1 - 1.2 E+2	3.7 E+1	0 - 1.0 E+2

Radionuclide	707-1000	297-707	149-297	74-149	30-74
^{60}Co	2.3 E+2	4.9 E+1	8.1 E+1	1.1 E+2	6.6 E+1
^{106}Ru	5.6 E+3	1.5 E+2	1.5 E+2	2.7 E+2	1.1 E+2
^{110m}Ag	3.7 E+0	1.1 E+0	1.3 E+0	1.8 E+0	1.0 E+0

TABLE 3. (continued)

	Particle Size Fraction (μm)				
Radionuclide	707-1000	297-707	149-297	74-149	30-74
^{125}Sb	1.9 E+3	2.2 E+2	3.4 E+2	4.8 E+2	2.0 E+2
^{134}Cs	5.6 E+1	2.7 E+1	4.4 E+1	5.1 E+1	3.2 E+1
^{137}Cs	1.1 E+3	6.5 E+2	9.1 E+2	1.0 E+3	6.1 E+2
^{144}Ce	2.3 E+3	2.4 E+3	1.6 E+3	1.7 E+3	7.1 E+2
^{154}Eu	4.5 E+1	4.3 E+1	2.4 E+1	3.4 E+1	1.1 E+1
^{155}Eu	1.1 E+2	9.7 E+1	6.7 E+1	6.9 E+1	2.6 E+1

---

a. Listed radionuclide concentrations are for the individual particles and fractions analyzed, which were obtained to provide examples of specific particle types and size fractions rather than be representative of the entire sample.

b. Two pieces of zircaloy were included in the average concentration; therefore, the average will not be representative of the size fraction.

c. ND = radionuclide not detected.

d. Only one particle showed ^{110m}Ag. It was not measurable in other samples.

TABLE 4. RADIONUCLIDE CONCENTRATIONS AND RANGES FOR SAMPLE 3[a] (μCi/g)

	Particle Size Fraction (μm)					
	>4000		1680-4000		1000-1680	
Radionuclide	Average	Range	Average	Range	Average	Range
^{60}Co	4.8 E+1	2.0 E+0 - 1.3 E+2	6.1 E+0	3.3 E+0 - 8.6 E+0	3.1 E+1	6.4 E+0 - 7.1 E+1
^{106}Ru	7.8 E+2	3.8 E+0 - 1.5 E+3	9.4 E+2	5.1 E+1 - 2.6 E+3	1.4 E+2	4.2 E+1 - 2.4 E+2
^{125}Sb	6.6 E+1	6.9 E+0 - 1.3 E+2	4.0 E+1	6.1 E+0 - 9.6 E+1	2.3 E+1	9.0 E+0 - 4.4 E+1
^{134}Cs	2.3 E+1	5.0 E-1 - 5.7 E+1	4.9 E+1	1.1 E+1 - 9.2 E+1	2.1 E+1	4.6 E+0 - 4.8 E+1
^{137}Cs	3.8 E+2	4.6 E+1 - 9.5 E+2	9.1 E+2	3.9 E+2 - 1.6 E+3	4.0 E+2	7.3 E+1 - 9.3 E+2
^{144}Ce	2.2 E+3	5.8 E+1 - 3.9 E+3	3.2 E+3	5.7 E+2 - 7.0 E+3	2.0 E+3	9.3 E+2 - 2.6 E+3
^{154}Eu	3.7 E+1	7.1 E-1 - 6.8 E+1	5.3 E+1	4.3 E+0 - 1.2 E+2	3.5 E+1	1.6 E+1 - 4.7 E+1
^{155}Eu	8.8 E+1	2.9 E+0 - 1.6 E+2	1.4 E+2	2.8 E+1 - 3.1 E+2	8.7 E+1	4.0 E+1 - 1.1 E+2

Radionuclide	707-1000	297-707	149-297	74-149	30-74	<30
^{60}Co	9.2 E+1	2.2 E+1	6.6 E+1	8.6 E+1	1.4 E+2	1.0 E+2
^{106}Ru	2.1 E+2	1.2 E+2	3.1 E+2	2.3 E+2	6.5 E+2	2.5 E+2
^{125}Sb	3.4 E+1	1.9 E+1	1.1 E+2	1.9 E+2	2.2 E+2	1.8 E+2
^{134}Cs	3.1 E+1	3.5 E+1	4.3 E+1	5.2 E+1	5.2 E+1	2.9 E+1

TABLE 4. (continued)

	Particle Size Fraction (μm)					
	>4000		1680-4000		1000-1680	
Radionuclide	Average	Range	Average	Range	Average	Range
^{137}Cs	5.4 E+2	8.4 E+2	9.0 E+2	9.0 E+2	8.9 E+2	6.6 E+2
^{144}Ce	2.4 E+3	1.8 E+3	1.6 E+3	1.5 E+3	1.2 E+3	7.5 E+2
^{154}Eu	4.5 E+1	3.2 E+1	2.6 E+1	2.3 E+1	1.7 E+1	1.0 E+1
^{155}Eu	1.0 E+2	3.8 E+1	8.2 E+3	6.3 E+1	4.9 E+1	3.1 E+1

---

a. Listed radionuclide concentrations are for the individual particles and fractions analyzed, which were obtained to provide examples of specific particle types and size fractions rather than be representative of the entire sample.

TABLE 5. RADIONUCLIDE CONCENTRATIONS AND RANGES FOR SAMPLE 4[a] (μCi/g)

	Average	Range
^{60}Co	8.6 E+1	2.8 E+0 - 2.5 E+2
^{106}Ru	1.5 E+3	2.4 E+2 - 3.3 E+3
^{125}Sb	9.9 E+1	6.8 E+0 - 2.0 E+2
^{134}Cs	6.5 E+1	1.7 E+0 - 1.8 E+2
^{137}Cs	1.3 E+3	3.6 E+0 - 3.9 E+3
^{144}Ce	4.3 E+3	7.8 E+2 - 8.6 E+3
^{154}Eu	6.5 E+1	9.3 E+0 - 1.5 E+2
^{155}Eu	1.4 E+2	3.0 E+1 - 3.2 E+2

---

a. Sample 4 consisted mostly of large particles.

TABLE 6. RADIONUCLIDE CONCENTRATIONS AND RANGES FOR SAMPLE 5[a] (µCi/g)

	Particle Size Fraction (µm)						
	>4000		1680-4000		1000-1680		<1000
Radionuclide	Average	Range	Average	Range	Average	Range	
^{60}Co	4.9 E+1	2.8 E+0 - 1.2 E+2	1.6 E+1	2.1 E+0 - 3.1 E+1	3.4 E+1	6.6 E-1 - 1.0 E+2	5.5 E+1
^{106}Ru	1.2 E+3	6.4 E+2 - 2.2 E+3	6.2 E+2	5.6 E+2 - 6.9 E+2	1.8 E+3	1.3 E+3 - 2.8 E+3	6.5 E+2
^{125}Sb	1.4 E+2	2.5 E+1 - 3.0 E+2	3.8 E+1	1.3 E+1 - 6.3 E+1	2.8 E+2	1.0 E+2 - 6.1 E+2	8.0 E+1
^{134}Cs	1.5 E+1	6.8 E+0 - 2.3 E+1	1.6 E+1	2.9 E+0 - 2.9 E+1	1.4 E+2	3.2 E+1 - 3.6 E+2	9.9 E+1
^{137}Cs	3.4 E+2	1.5 E+2 - 3.9 E+2	4.1 E+2	3.8 E+1 - 7.9 E+2	2.5 E+3	5.1 E+2 - 6.5 E+3	1.7 E+3
^{144}Ce	3.5 E+3	1.8 E+3 - 6.6 E+3	2.1 E+3	1.9 E+3 - 2.4 E+3	6.0 E+3	3.6 E+3 - 1.1 E+4	2.2 E+3
^{154}Eu	5.5 E+1	1.6 E+1 - 1.2 E+2	2.3 E+1	1.7 E+1 - 2.9 E+1	1.1 E+2	6.2 E+1 - 2.2 E+2	3.5 E+1
^{155}Eu	1.4 E+2	8.1 E+1 - 2.7 E+2	8.8 E+1	7.4 E+1 - 1.0 E+2	2.7 E+2	1.4 E+2 - 5.1 E+2	1.1 E+2

---

a. Listed radionuclide concentrations are for the individual particles and fractions analyzed, which were obtained to provide examples of specific particle types and size fractions rather than be representative of the entire sample.

TABLE 7. RADIONUCLIDE CONCENTRATIONS AND RANGES FOR SAMPLE 6[a]
(μCi/g)

Radionuclide	Particle Size Fraction (μm)					
	>4000[b]		1680-4000		1000-1680	
	Average	Range	Average	Range	Average	Range
^{60}Co	2.5 E+0	0 - 6.1 E+0	1.9 E+0[c]	0 - 4.9 E+0	7.1 E+0	6.9 E+0 - 7.3 E+0
^{106}Ru	4.2 E+2	1.3 E+0 - 1.1 E+3	6.1 E+2	7.0 E+0 - 1.0 E+3	4.4 E+2	2.9 E+2 - 5.8 E+2
^{125}Sb	1.1 E+2	2.4 E+1 - 3.0 E+2	6.5 E+1	1.5 E+1 - 1.0 E+2	5.0 E+1	1.8 E+1 - 8.2 E+1
^{134}Cs	2.2 E+1	2.2 E+0 - 5.5 E+1	8.3 E+1	3.2 E+1 - 1.7 E+2	8.8 E+1	5.0 E-1 - 1.7 E+2
^{137}Cs	5.7 E+2	4.4 E+1 - 1.3 E+3	1.8 E+3	6.2 E+2 - 3.8 E+3	2.0 E+3	1.1 E+1 - 4.1 E+3
^{144}Ce	1.3 E+3	1.9 E+0 - 3.6 E+3	1.8 E+3	1.8 E+1 - 3.1 E+3	2.0 E+3	6.9 E+2 - 3.5 E+3
^{154}Eu	1.3 E+1[c]	0 - 3.2 E+1	2.3 E+1[c]	0 - 4.3 E+1	3.2 E+1	1.3 E+1 - 5.1 E+1
^{155}Eu	5.5 E+1[c]	0 - 1.5 E+2	8.7 E+1[c]	1.2 E+2 - 1.4 E+2	3.3 E+1	3.2 E+1 - 3.5 E+1

Radionuclide	707-1000	297-707	149-297	74-149	30-74
^{60}Co	1.4 E+2	5.2 E+1	9.2 E+1	1.1 E+2	1.2 E+2
^{106}Ru	4.2 E+2	2.2 E+2	2.9 E+2	3.7 E+2	5.2 E+2
^{125}Sb	8.8 E+1	9.8 E+1	1.5 E+2	1.9 E+2	1.7 E+2

TABLE 7. (continued)

	Particle Size Fraction (μm)					
	>4000[b]			1680-4000		1000-1680
Radionuclide	707-1000	297-707	149-297	74-149	30-74	
^{134}Cs	5.7 E+1	5.8 E+1	5.4 E+1	4.8 E+1	5.0 E+1	
^{137}Cs	1.2 E+3	1.1 E+3	1.1 E+3	9.6 E+2	9.5 E+2	
^{144}Ce	2.3 E+3	2.1 E+3	1.4 E+3	1.3 E+3	1.1 E+3	
^{154}Eu	3.6 E+1	3.6 E+1	2.2 E+1	2.1 E+1	1.8 E+1	
^{155}Eu	1.1 E+2	9.2 E+1	6.7 E+1	7.8 E+1	4.5 E+1	

---

a. Listed radionuclide concentrations are for the individual particles and fractions analyzed, which were obtained to provide examples of specific particle types and size fractions rather than be representative of the entire sample.

b. Average includes two zircaloy pieces (known).

c. Unmeasurable data included in average.

the range of the concentrations. Radionuclide concentrations for aliquots having particle sizes less than 1000 μm are relatively consistent for all five samples, indicating that the material in these size fractions is relatively homogeneous as to radionuclide concentration. For the large size fractions (i.e., $\geq$1000 μm), there appears to be a much wider range of radionuclide concentrations among individual particles. In some instances, these results are caused by the obvious presence of structural materials (see Appendix A). The structural materials have been included in the data to provide information on radionuclide concentrations in core materials other than fuel. Table 8 presents data from fragmented pieces determined by fissile material content to be nonfuel core material. These data indicate significantly lower radionuclide concentrations than for other particles which are composed at least partially of fuel material.

Table 9 lists the weight fraction of uranium (i.e., total fissile/fertile material content) for each sample. These data are calculated by dividing the weight of UO_2 in each sample fraction, as listed in Appendix C, by the weight of the sample fraction analyzed. The fissile material measurements include ^{239}Pu which is the equivalent of 5 to 8% of the total fissile content, according to ORIGEN-2 calculations.

Observations that can be made concerning these data are as follows: (a) less than 15% of the particles analyzed contain more than 90-wt% uranium dioxide, indicating that most particles analyzed are agglomerates of fuel and nonfuel materials, (b) particles smaller than 707 μm in size tend to have decreasing percents of fuel content with decreasing particle size, and (c) the smaller particle size ranges (<707 μm) display a relatively consistent fuel content, indicating that they may have all been formed by a similar mechanism.

Table 10 lists the average fissile/fertile enrichments for the samples analyzed to date. For comparison, the actual fuel enrichments at each location are listed in the footnote. These average data, which represent preliminary results, have a range of approximately 20%. There is a general trend in the data, indicating a higher average enrichment (2.8%) at the E9

TABLE 8. RADIONUCLIDE CONCENTRATIONS OF NONFUEL CORE MATERIAL (μCi/g)

Radionuclide	Sample 1 Particle 1J	Sample 3 Particle 3B	Sample 6 Particle 6E	Sample 6 Particle 6F
^{60}Co	1.9 E+0	5.9 E+1	1.2 E+0	4.9 E+0
^{106}Ru	8.9 E+0	3.8 E+0	1.3 E+0	7.0 E+0
^{125}Sb	1.1 E+0	6.9 E+0	2.4 E+1	1.5 E+1
^{134}Cs	3.1 E+0	5.0 E-1	2.2 E+0	3.2 E+1
^{137}Cs	5.5 E+1	1.2 E+1	4.4 E+1	6.2 E+2[a]
^{144}Ce	3.2 E+2	5.8 E+1	1.9 E+0	1.8 E+1
^{154}Eu	5.4 E+0	7.2 E-1	ND[b]	ND
^{155}Eu	1.2 E+1	2.9 E+0	ND	ND
^{241}Am	ND	3.6 E-1	ND	ND
Fissile Material (mg)	<0.02	<1.6 E-2	<0.02	<0.02

---

[a] This data point is higher than other ^{137}Cs concentrations. The reason is not known.

[b] ND = radionuclide not detected.

TABLE 9. WEIGHT FRACTION OF URANIUM FOR THE TMI-2 CORE DEBRIS GRAB SAMPLES[a,b]

Particle Size Fraction (μm)	Particle/Aliquot	Sample 1 (H8, surface)	Sample 3 (H8, 22 in.)	Sample 4 (E9, surface)	Sample 5 (E9, 3 in.)	Sample 6 (E9, 22 in.)
>4000	Particle (A)	0.11	0.44	NA[c]	NA	NA
>4000	Particle (B)	1.0	0	0.22	1.0	NA
>4000	Particle (C)	0.66	NA	NA	NA	0.41
>4000	Particle (D)	0.98	0.94	NA	NA	0.88
>4000	Particle (E)	0.22	0.94	NA	0.43	0
1680-4000	Particle (F)	0.79	NA		0.66	0
1680-4000	Particle (G)	0.63	NA		NA	0.90
1680-4000	Particle (H)	0.53	0.62		NA	0.99
1000-1680	Particle (I)	0	NA		NA	0.11
1000-1680	Particle (J)	0.08	0.20		0.85	0.15
1000-1680	Particle (K)	0.61	0.47		0.82	0.84
<1000		--	--		0.52	--
707-1000	Aliquot	0.73	NA			0.64
297-707	Aliquot	0.65	NA			0.62
149-297	Aliquot	0.45	NA			0.42
74-149	Aliquot	0.52	NA			0.43
30-74	Aliquot	0.20	0.32			0.29
<30	Aliquot	--	0.37			--

---

a. Calculated assuming all fissile/fertile material was in the form of UO_2 and that the ^{239}Pu component of the fuel is a negligible component of the total fissile material content (i.e., 5 to 8%, from ORIGEN-2 calculations).

b. Total weights of uranium and particle/aliquot weights obtained from Appendix C.

c. NA = data not available at this time.

TABLE 10. AVERAGE MEASURED URANIUM ENRICHMENT FOR THE TMI-2 CORE DEBRIS GRAB SAMPLES[a]

Sample	Average Enrichment[b] (%)	Number of Analyses
1 (H8, surface)	2.4 ± 0.3	15
3 (H8, 22 in.)	2.3 ± 0.4	8
4 (E9, surface)	3.4	1
5 (E9, 3 in.)	2.8 ± 0.2	6
6 (E9, 22 in.)	2.8 ± 0.2	11

---

a. There were three fuel assembly enrichments in the TMI-2 core. The peripheral fuel assemblies were 2.96% enriched. The inner fuel assemblies alternated between 1.98 and 2.64% enriched. The H8 and E9 fuel assemblies were originally enriched to 2.64 and 1.98%, respectively. The average core enrichment was 2.57%.

b. The average enrichments for the measured samples were calculated by summing the individual particle and aliquot enrichments from Appendix C and dividing the sum by the number of analyses performed.

location. The data indicate a definite bias at the E9 core location for the particles and aliquots analyzed. These data indicate fuel mixing at the E9 core location for the 2.96%-enriched fuel from the core periphery. The data at the H8 location suggests a mixing of the 1.98- and 2.64%-enriched fuels to provide the measured average enrichment of 2.4%, which is closer to the core average of 2.57%.

Table 11 lists the fission product content per gram of UO_2 calculated by the ORIGEN-2 code. Table 12 lists the ratios of the measured fission product concentrations to the ORIGEN-2 predicted fission product content/gram UO_2 for Sample 1. These data were calculated using the following equation:

$$R = \frac{C_F}{C_u \times C_p}$$

where

R = ratio of measured to ORIGEN-2 predicted fission product content per gram UO_2

C_F = measured fission product concentration in μCi/g (see Appendix B)

C_u = measured fissile material content - ^{235}U content in grams (see Appendix C)

C_p = ORIGEN-2 predicted fission product concentration in μCi/g ^{235}U.

These data indicate that the there are radionuclides that remain principally associated with the fuel. These radionuclides are ^{144}Ce, ^{154}Eu, and ^{155}Eu. The ORIGEN-2 code analysis was done for the core average enrichment, which may account for some ratios being greater than 1.0. Actual measured enrichments for the listed sample fractions may vary

TABLE 11. TMI-2 CORE FISSION PRODUCT CONTENT PER GRAM UO_2 [a]

Radionuclide	Total Inventory (Ci)	Fission Product Content Per Gram UO_2 [b] (Ci)
^{60}Co[c]	6.97 E+4	7.49 E-4
^{106}Ru	1.02 E+5	1.10 E-3
^{110m}Ag[c]	1.25 E+5	1.77 E-4
^{125}Sb[c]	3.48 E+4	3.75 E-4
^{134}Cs	3.18 E+4	3.42 E-4
^{137}Cs	7.26 E+5	8.16 E-3
^{144}Ce	2.57 E+5	2.76 E-3
^{154}Eu[c]	5.47 E+3	5.88 E-5
^{155}Eu[c]	1.57 E+4	1.69 E-4

---

a. Data obtained from ORIGEN 2 code analysis of the core inventory, assuming 2.57% enrichment and 3250 MWd/tU on 1 May 1984.

b. ^{235}U content is 2.27×10^{-2} g/g UO_2.

c. Activation and/or fission product.

TABLE 12. MEASURED TO PREDICTED FISSION PRODUCT/UO_2 RATIOS FOR SAMPLE 1

	Particle Size Fraction (μm)					
Radionuclide	>4000 Particle 1A	>4000 Particle 1B	>4000 Particle 1C	>4000 Particle 1D	>4000 Particle 1E	1680-4000 Particle 1F
^{60}Co	2.8 E-1	2.9 E-2	1.9 E-2	3.0 E-2	8.6 E-2	1.5 E-2
^{106}Ru	5.2 E-1	1.7 E+0	9.9 E-2	9.3 E-1	1.2 E+0	5.2 E-2
^{110m}Ag	--	--	--	--	--	--
^{125}Sb	2.6 E+0	2.6 E-1	5.5 E-2	4.3 E-2	1.2 E+0	8.0 E-2
^{134}Cs	1.3 E-1	1.3 E-2	3.6 E-1	3.6 E-2	4.9 E-1	4.6 E-1
^{137}Cs	2.8 E-2	9.8 E-3	2.6 E-1	2.8 E-2	4.9 E-1	3.5 E-1
^{144}Ce	5.1 E-1	1.7 E+0	1.7 E+0	1.3 E+0	1.3 E+0	1.6 E+0
^{154}Eu	1.1 E-1	1.2 E+0	1.3 E+0	8.9 E-1	8.5 E-1	1.4 E+0
^{155}Eu	4.6 E-1	1.1 E+0	1.1 E-1	8.4 E-1	9.8 E-1	1.0 E+0
Fissile Material (g UO_2/ g sample)	2.8 E-3	1.9 E-2	1.4 E-2	2.0 E-2	4.8 E-3	1.6 E-2

TABLE 12. (continued)

	Particle Size Fraction (μm)				
Radionuclide	1680-4000 Particle 1G	1680-4000 Particle 1H	1000-1680 Particle 1I	1000-1680 Particle 1J	1000-1680 Particle 1K
^{60}Co	2.6 E-2	1.8 E-1	ND	3.7 E-2	1.9 E-2
^{106}Ru	1.4 E-1	1.7 E-1	ND	1.1 E-1	7.3 E-2
^{110m}Ag	--	--	--	--	--
^{125}Sb	1.0 E-1	6.9 E-2	ND	4.2 E-2	2.3 E-2
^{134}Cs	6.0 E-1	3.2 E-2	ND	1.3 E-1	2.6 E-2
^{137}Cs	4.3 E-1	2.5 E-2	ND	9.6 E-2	1.9 E-2
^{144}Ce	1.7 E+0	1.4 E+0	ND	1.6 E+0	1.6 E+0
^{154}Eu	1.2 E+0	9.0 E-1	ND	1.3 E+0	1.4 E+0
^{155}Eu	1.2 E+0	8.6 E-1	ND	1.0 E+0	1.0 E+0
Fissile Material (g UO_2/ g sample)	1.1 E-2	1.3 E-2	0	1.6 E-3	1.3 E-2

TABLE 12. (continued)

	Particle Size Fraction (μm)				
Radionuclide	707-1000 Aliquot	297-707 Aliquot	149-297 Aliquot	74-149 Aliquot	30-74 Aliquot
^{60}Co	4.6 E-1	1.1 E-1	2.7 E-1	3.3 E-1	5.4 E-2
^{106}Ru	7.7 E+0	2.2 E-1	3.4 E-1	5.7 E-1	6.1 E-2
^{110m}Ag	3.2 E+2	1.0 E-2	1.8 E-2	2.3 E-2	3.5 E-3
^{125}Sb	7.7 E+0	9.6 E-1	2.3 E+0	2.9 E+0	3.3 E-1
^{134}Cs	2.5 E-1	1.3 E-1	3.2 E-1	3.4 E-1	5.8 E-2
^{137}Cs	2.0 E-1	1.3 E-1	2.8 E-1	2.8 E-1	4.6 E-2
^{144}Ce	1.3 E+0	1.4 E+0	1.4 E+0	1.4 E+0	1.6 E-1
^{154}Eu	1.2 E+0	1.2 E+0	1.0 E+0	1.3 E+0	1.2 E-1
^{155}Eu	9.9 E-1	9.3 E-1	9.9 E-1	9.3 E-1	9.3 E-2
Fissile Material (g UO_2/ g sample)	1.5 E-2	1.4 E-2	9.1 E-3	1.0 E-2	3.7 E-2

ND = none detected.

by 20% from the average. A discussion with individuals familiar with the ORIGEN-2 code indicated that the listed values are well within the expected range of values.[17] Less than 50% of the ORIGEN-2 predicted core inventory concentrations of the fission products ^{134}Cs, ^{137}Cs, ^{110m}Ag, ^{106}Ru, and ^{125}Sb were found.

9. CONCLUSIONS/OBSERVATIONS

The following is a summary of conclusions and observations based on preliminary analysis of the available core debris grab sample data:

- Because there are no significant differences in particle size between the H8 and E9 deep samples (Samples 3 and 6), those samples may be typical of the subsurface debris bed.
- Only about 0.3 wt% of the core debris samples consists of particles smaller than 100 μm in size.
- The E9 surface sample (Sample 4) and the E9 near surface sample (Sample 5) are similar. They are composed mostly of larger sized particles (>1000 μm).
- The fission product concentrations (μCi/g) are relatively consistent for all sample aliquots less than 707 μm.
- The fission product concentrations for nonfuel materials are significantly less than for fuel materials.
- Based on delayed neutron analyses, very few of the particles are strictly UO_2. Less than 15% of the particles measured contain more than 90% uranium, indicating that both fuel and nonfuel materials are generally contained in the particles.
- The average $^{235}U/^{238}U$ enrichment data indicate that the core samples at E9 had some contamination from the peripheral 2.96% enrichment fuel, whereas this was not observed at the H8 location.
- The measured concentrations of the ^{144}Ce, ^{154}Eu, and ^{155}Eu associated with fuel material agreed with the ORIGEN-2 code predictions; whereas, the measured concentrations of ^{134}Cs, ^{137}Cs, ^{110m}Ag, ^{106}Ru, and ^{125}Sb were less than 50% of the ORIGEN-2 predicted values.

- There are no overwhelming differences between melt-bearing particles obtained from the rubble bed surface near the radial core center (Particles 1A, 1E, and 1H) and those extracted at mid-radius at a bed depth of 22 in. (Particles 6D and 6F).

- Melt structures are generally high in impurities from prior reaction with Inconel and/or stainless steel.

- All five melt-bearing particles discussed in Section 3 (Particles 1A, 1E, 1H, 6D, and 6F) show evidence of prolonged elevated temperatures (cladding oxidation, pore migration to fuel grain boundaries, liquid-state oxidation of heterogeneous melts). Examination of all five particles suggests brief exposure to very high temperatures (fuel-bearing melts). However, only results from examining Particle 1H infer that locally high temperatures were maintained for a substantial period. The lack of equiaxed UO_2 grain growth, incomplete cladding oxidation, and so forth, strongly suggest that some local regions stayed relatively cool ($T << 2000$ K).

- Several instances were found where fuel liquefied and then solidified before being contacted by a second fuel-bearing melt.

- None of the five particles show clear signs of steam starvation. Contrariwise, the formation of $(U,Zr)O_2$ by diffusion of oxygen and the presumed oxidation of UO_2 to U_4O_9 imply ample steam availability throughout the high temperature portion(s) of the TMI-2 transient.

- Preliminary examination of selected large particles (e.g., Particles 1E and 1H) indicates peak core temperatures during the accident exceeded 2900 K.

10. REFERENCES

1. J. H. Carlson (ed.), *TMI-2 Core Examination Plan*, EGG-TMI-6169, Rev. 1, July 1984.

2. L. S. Beller and H. L. Brown, *Design and Operation of the Core Topography Data Acquisition System for TMI-2*, GEND-INF-012, May 1984.

3. S. L. Seiffert and G. R. Smolik, *Postirradiation Examination Results for the Power-Cooling-Mismatch Test-2A*, TREE-NUREG-1029, February 1977

4. S. A. Ploger et al., *Postirradiation Examination Results for the Irradiation Effects Test 2*, TREE-NUREG-1195, January 1978.

5. D. L. Hagrman et al., *MATPRO-Version A Handbook of Materials Properties for Use in the Analysis of Light Water Reactor Fuel Rod Behavior*, NUREG/CR-0479, August 1981, p. 136.

6. P. Hofmann and D. K. Kerwin-Peck, "Chemical Interactions of Solid and Liquid Zircaloy With UO_2 Under Transient Nonoxidizing Conditions," *International Meeting on LWR Severe Accident Evaluation, Cambridge, MA, August 28-September 1, 1983*.

7. P. Hofmann and D. K. Kerwin-Peck, *UO_2/Zry-4 Chemical Interactions and Reaction Kinetics from 1000 to 1700°C Under Isothermal Conditions*, KfK Report 3552, 1983.

8. P. Hofmann and D. K. Kerwin-Peck, "UO_2/Zry-4 Chemical Interactions from 1000 to 1700°C Under Isothermal and Transient Temperature Conditions," *Journal of Nuclear Materials, 124*, 1984, pp. 80-105.

9. P. Hofmann and H. J. Neitzel, "External and Internal Reaction of Zry Tubing with Oxygen and UO_2 and Its Modeling," *5th International Meeting on Thermal Nuclear Reactor Safety, Karlsruhe, Germany, September 9-13, 1984*.

10. W. Dienst, P. Hofmann, D. K. Kerwin-Peck, "Chemical Interactions Between UO_2 and Zry-4 from 1000 to 2000°C," *Nuclear Technology, 65*, 1984, pp. 109-124.

11. P. Hofmann and C. Politis, "The Kinetics of the UO_2-Zry Reactions at High Temperatures," *Journal of Nuclear Materials, 87*, 1979, pp. 375-397.

12. P. Hofmann, "Transient Temperature UO_2/Zry-4 Interaction Experiments Under Oxidizing Conditions up to About 2000°C," The Annual Report of the Nuclear Safety Project (1984), KfK-3550, 1985, (to be published).

13. P. Hofmann et al., "Liquid Zry/Liquid UO_2 Interaction Experiments," *The Annual Report of the Nuclear Safety Project (1983)*, KfK Report 3450, 1984, pp. 4200/126-4200/154.

14. D. L. Evans, TMI-2 Fuel Recovery Plant Feasibility Study, EGG-TMI-6130, December 1982.

15. Y. D. Harker, Feasibility of Measuring the Fissile Content of Irradiated Fuel Samples, REA-83-022, February 16, 1983.

16. A. G. Groff, ORIGEN-2--A Revised and Updated Version of the Oak Ridge Isotope Generation and Depletion Code, ORNL-5621, July 1980.

17. Personal communication between D. W. Akers and B. G. Schnitzler, EG&G Idaho, Inc., May 29, 1984.

APPENDIX A

PHOTOGRAPHS OF DISCRETE PARTICLES

APPENDIX A

PHOTOGRAPHS OF DISCRETE PARTICLES

As part of the initial unpackaging, weighing, and visual examination of the core debris grab samples, several larger sized ($\geq$1000 µm) particles from each sample were selected for follow-on examination and analysis. These particles were individually weighed and photographed before performing the follow-on examinations. This appendix contains photographs of all particles from Samples 1, 4, 5, and 6. Photographs of the individual particles from Sample 3 were misplaced during processing. These particles will be rephotographed, and the photographs added to the final core debris grab sample report. Photographs of individual particles smaller than 1000 µm are not included in this report because of the lack of acuity in the photographs.

Photographs for the eleven particles from Sample 1 are shown in Figures A-1 though A-6. The five particles from Sample 4 are shown in Figures A-7 through A-10. The eleven particles from Sample 5 are shown in Figures A-11 through A-16, and the eleven particles from Sample 6 are shown in Figures A-17 through A-22. The scales shown on the photographs have divisions equal to 1 mm (1000 µm).

a. Front view of particle. 84-216-2-22

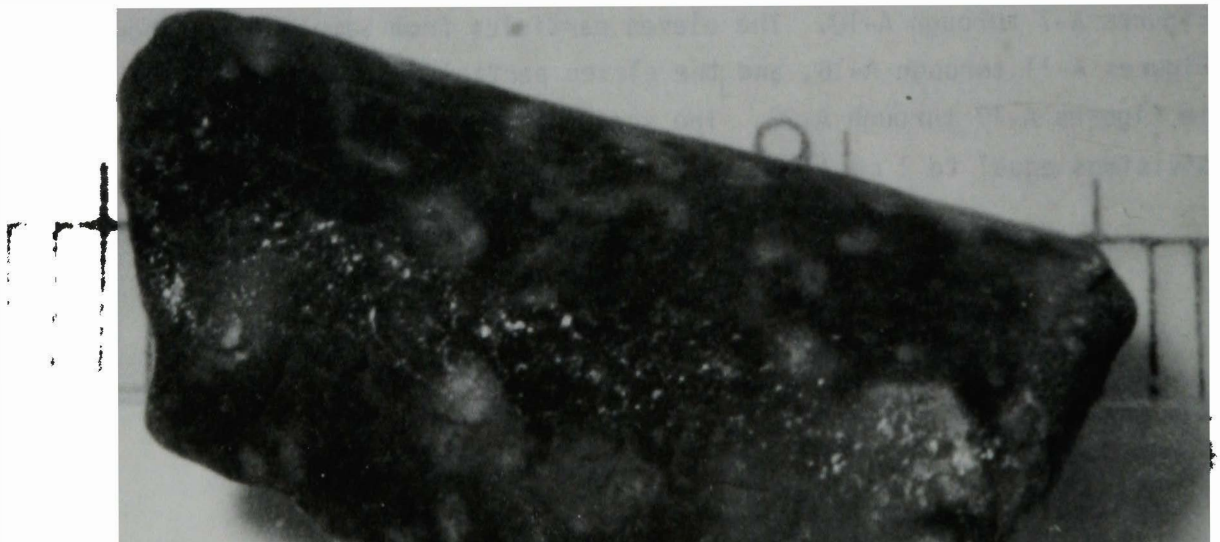

b. Back view of particle. 84-216-2-30

Figure A-1. Particle 1A from Sample 1 (surface of debris bed at H8 core location), size range: >4000 μm.

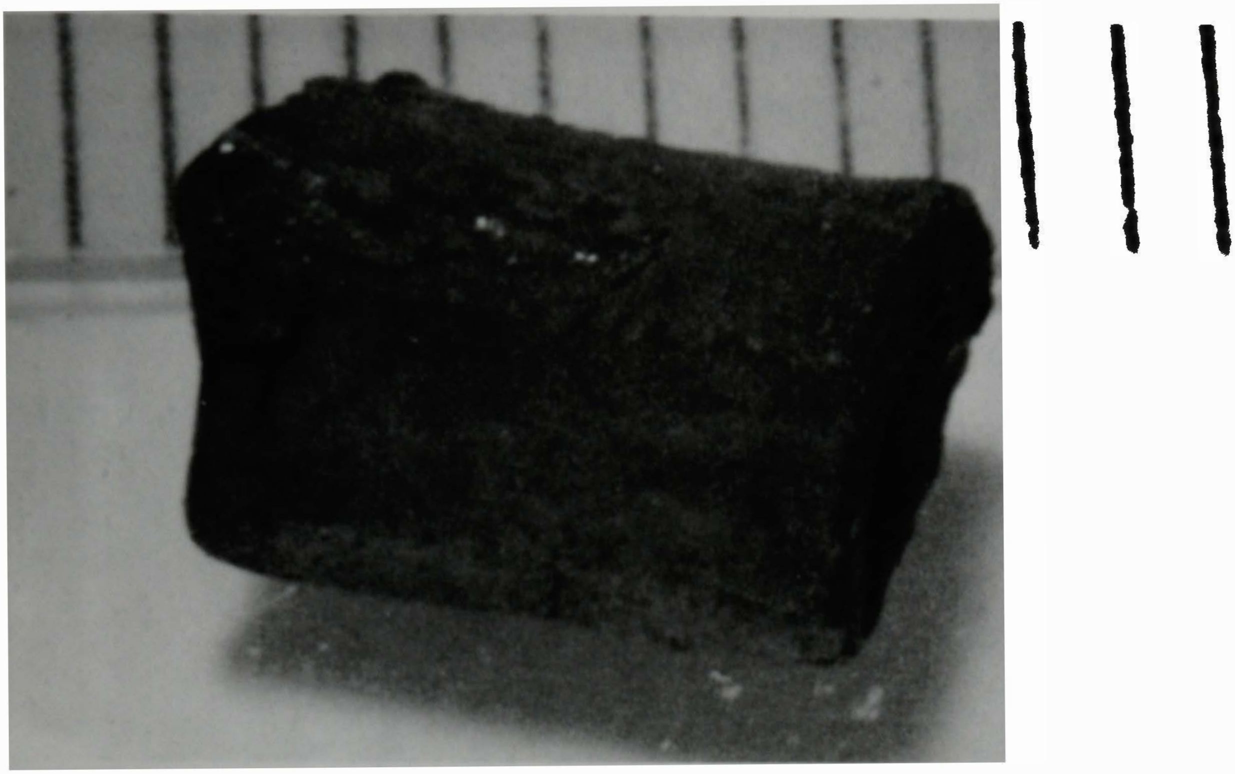

a. Particle 1B (size range: >4000 µm).

84-216-3-4

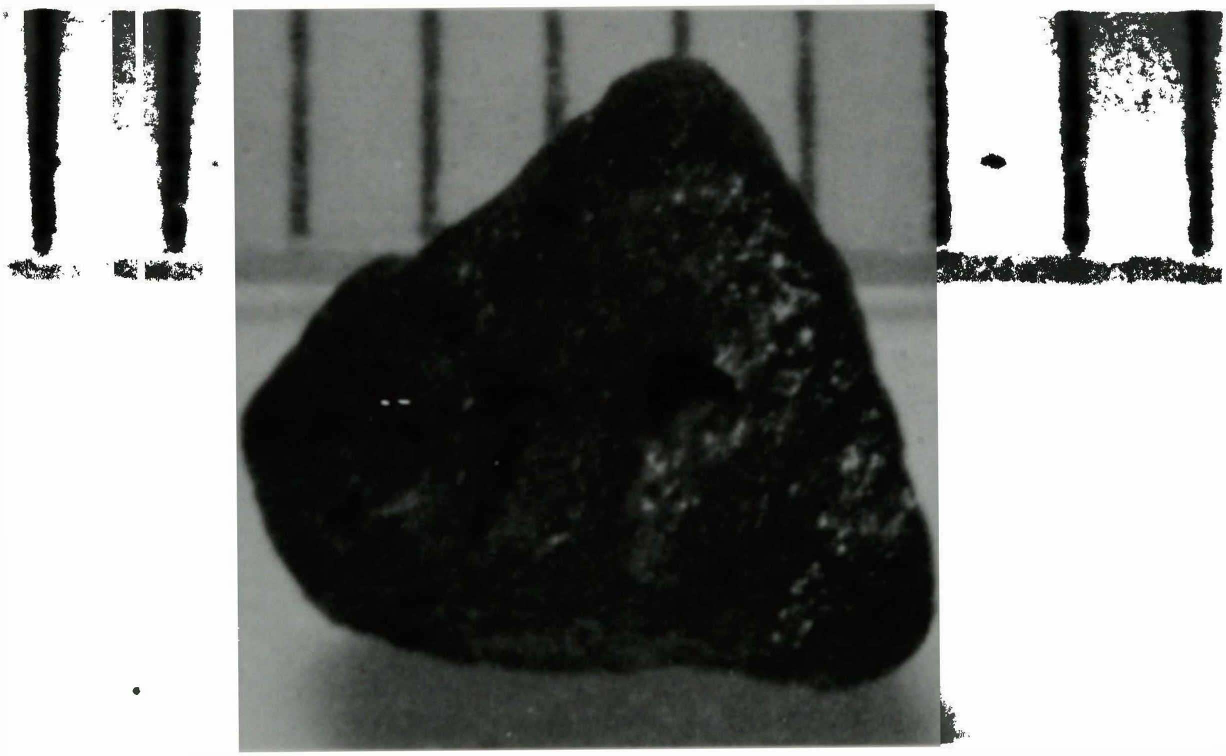

b. Particle 1C (size range: >4000 µm).

84-216-3-9

Figure A-2. Particles from Sample 1 (surface of debris bed at H8 core location).

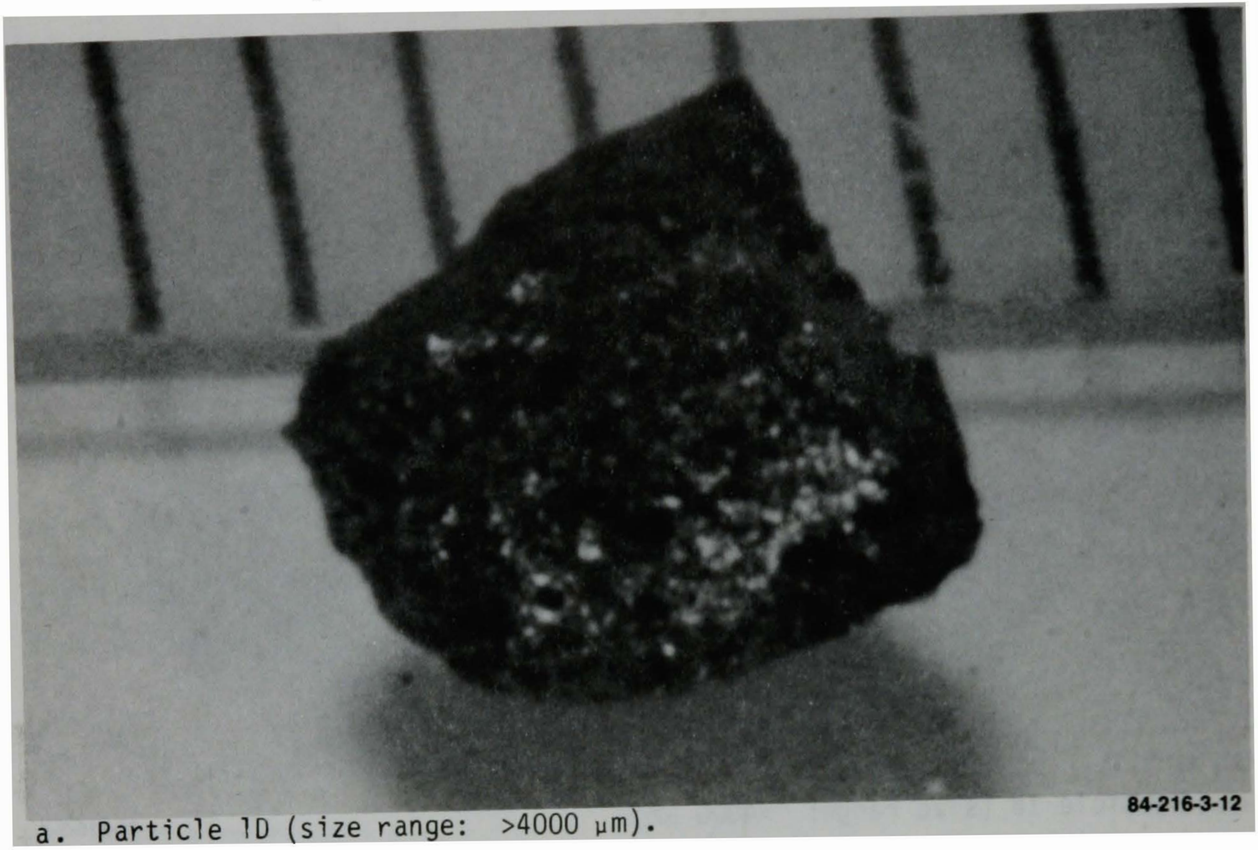

a. Particle 1D (size range: >4000 μm).

84-216-3-12

b. Particle 1E (size range: >4000 μm).

84-216-3-17

Figure A-3. Particles from Sample 1 (surface of debris bed at H8 core location).

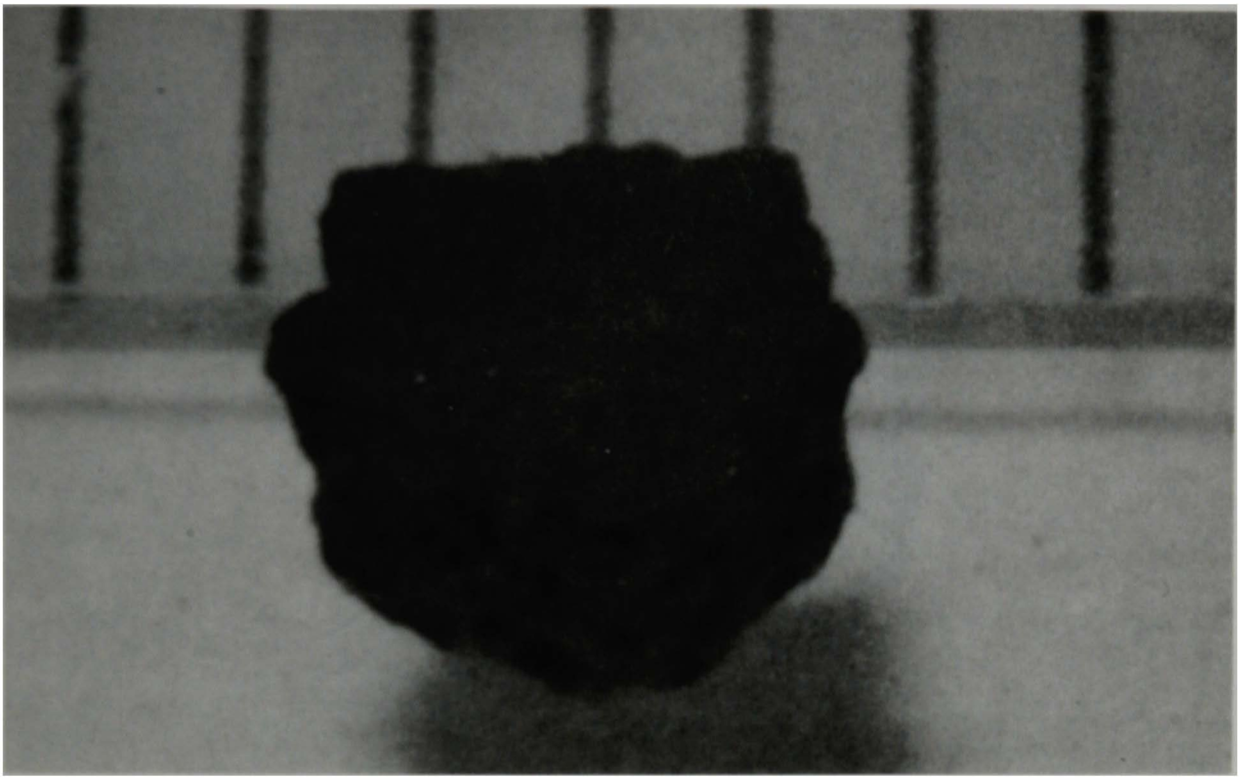

a. Particle 1F (size range: 1680-4000 µm). 84-216-3-18

b. Particle 1G (size range: 1680-4000 µm). 84-216-3-21

Figure A-4. Particles from Sample 1 (surface debris bed at H8 core location).

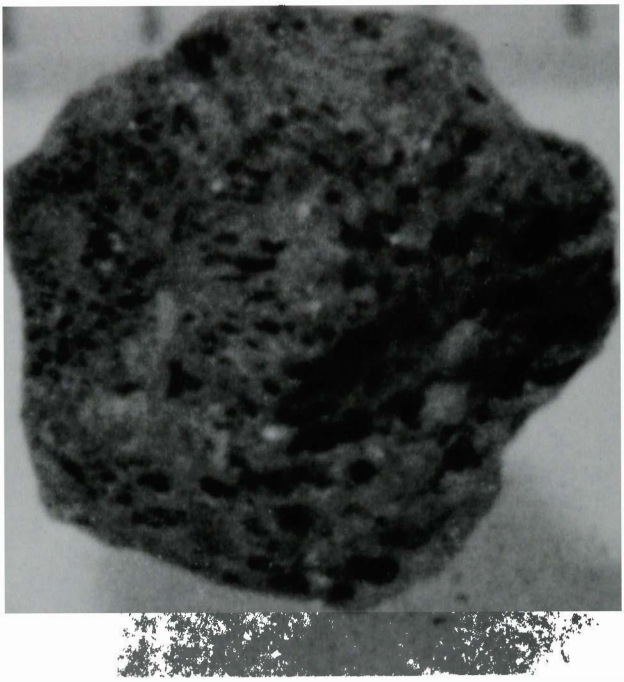

a. Particle 1H (size range: 1680-4000 μm).

84-216-3-23

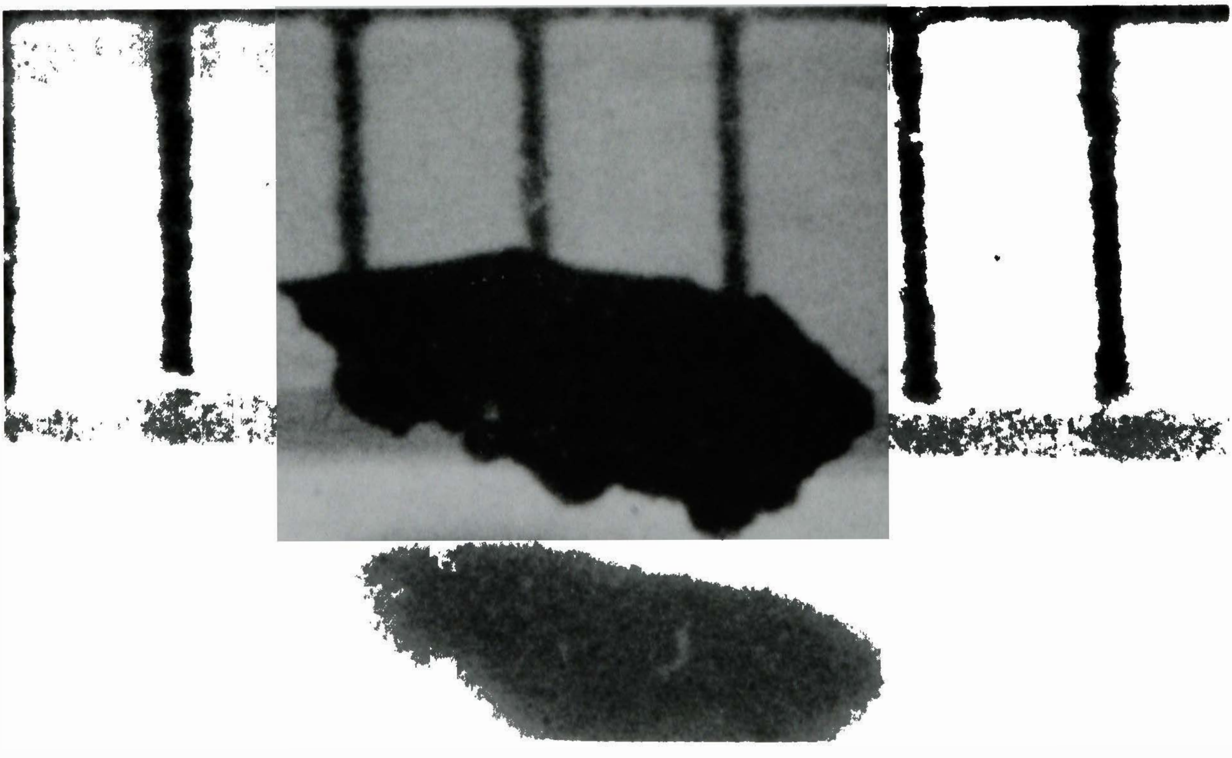

84-216-3-24

b. Particle 1I (size range: 1000-1680 μm).

Figure A-5. Particles from Sample 1 (surface of debris bed at H8 core location).

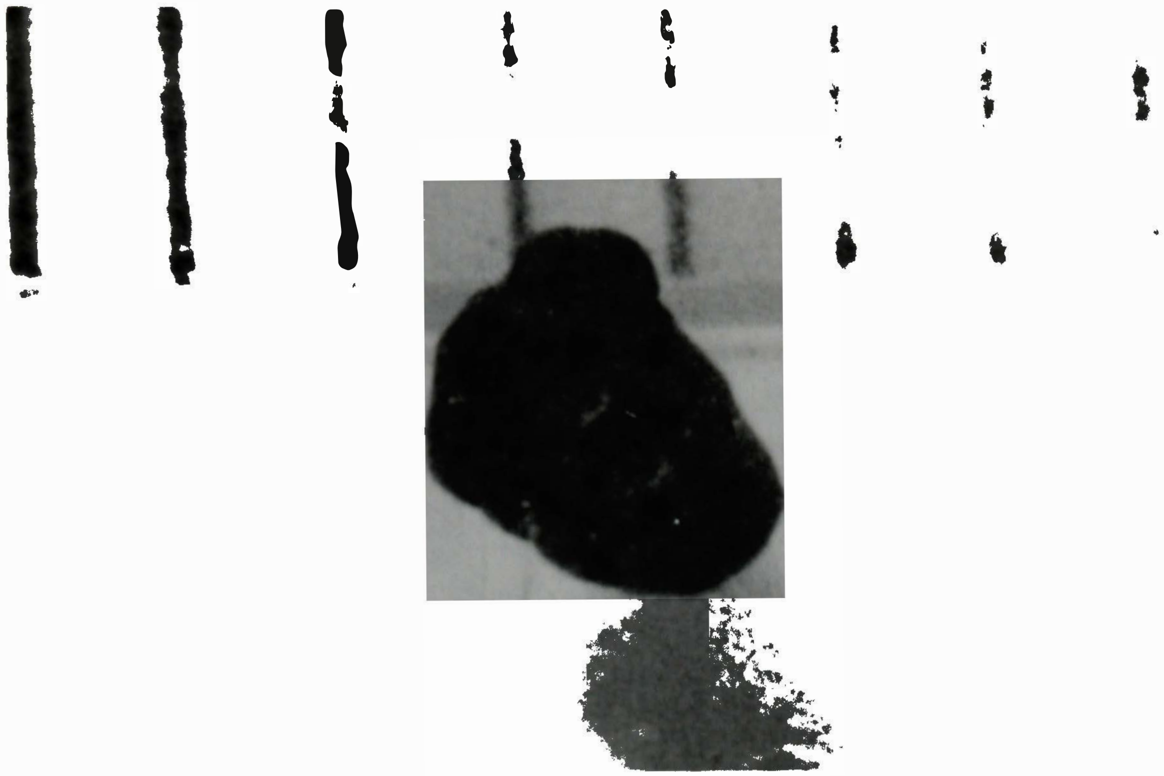

a. Particle 1J (size range: 1000-1680 µm). 84-216-3-28

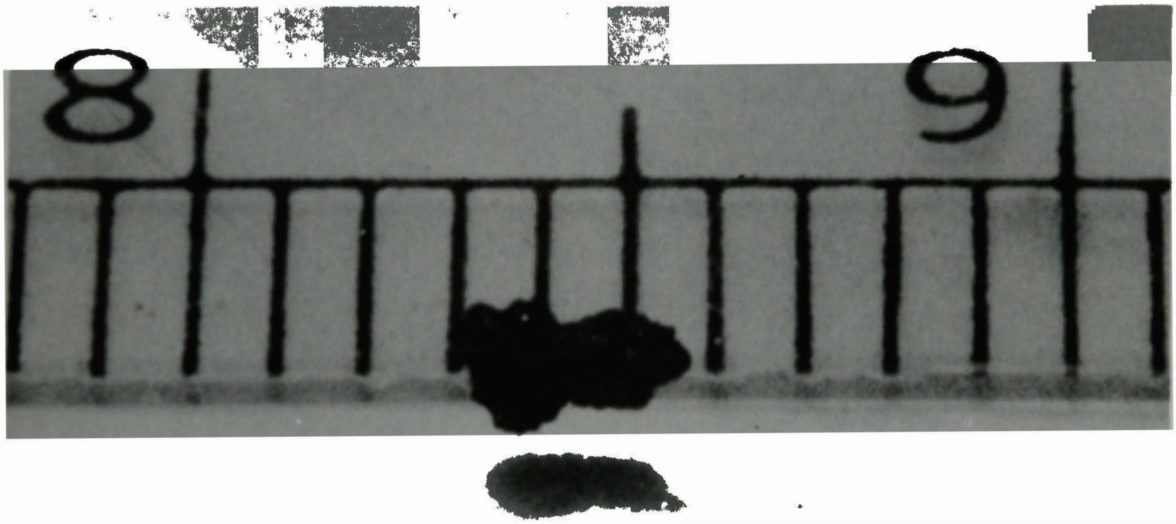

b. Particle 1K (size range: 1000-1680 µm). 84-216-3-27

Figure A-6. Particles from Sample 1 (surface of debris bed at H8 core location).

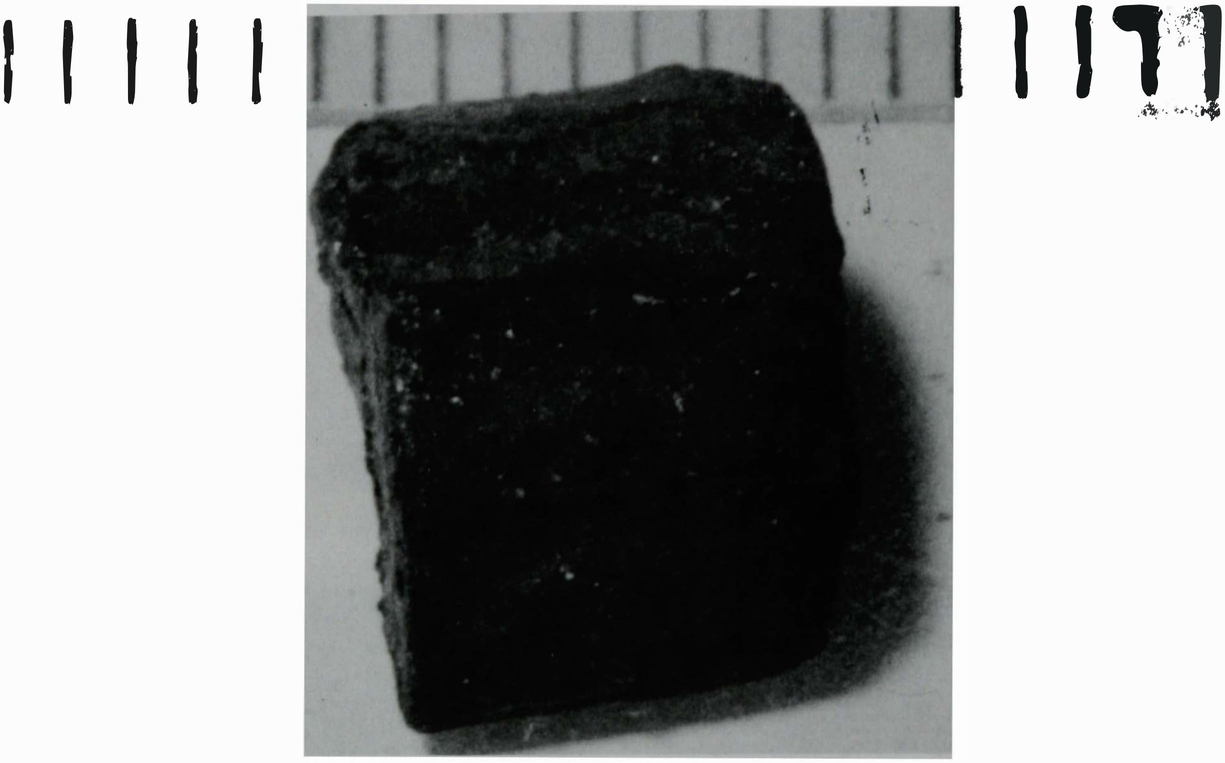

84-157-2-28

Figure A-7. Particle 4A from Sample 4 (surface of debris bed at E9 core location), size range: >4000 μm.

84-157-2-11

a. Front view of particle.

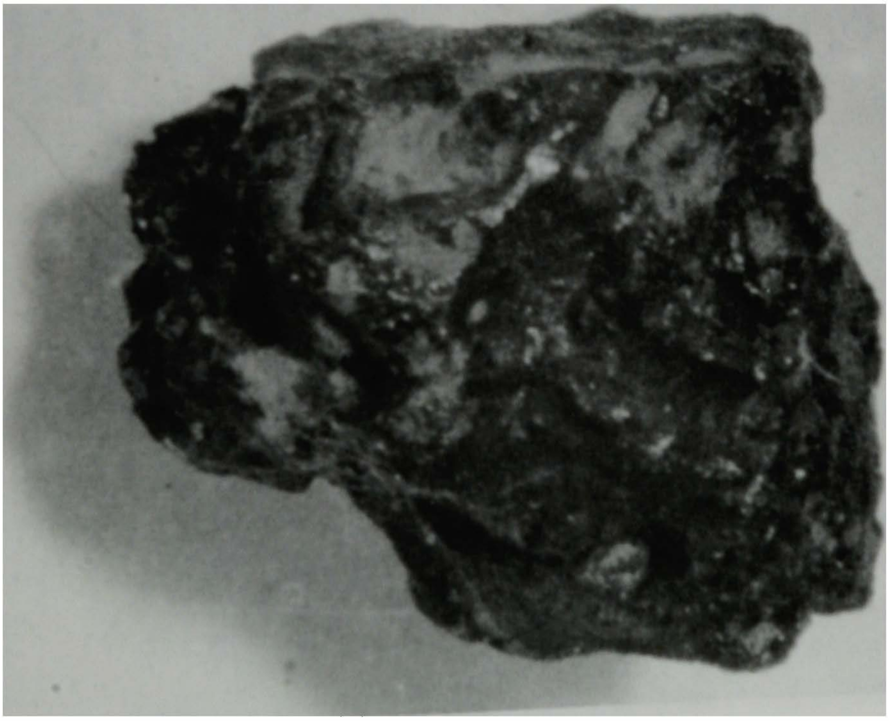

84-157-2-16

b. Back view of particle.

Figure A-8. Particle 4B from Sample 4 (surface of debris bed at E9 core location), size range: >4000 μm.

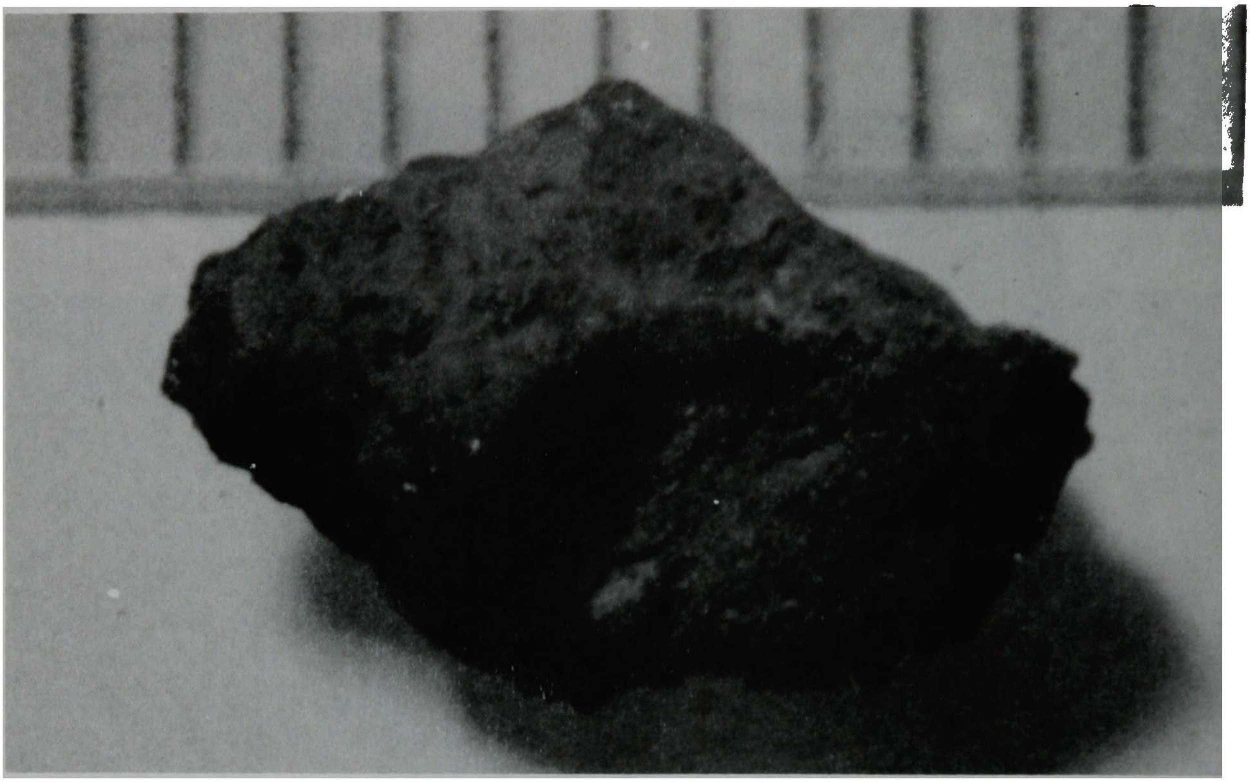

a. Particle 4C (size range: >4000 µm).

84-157-2-22

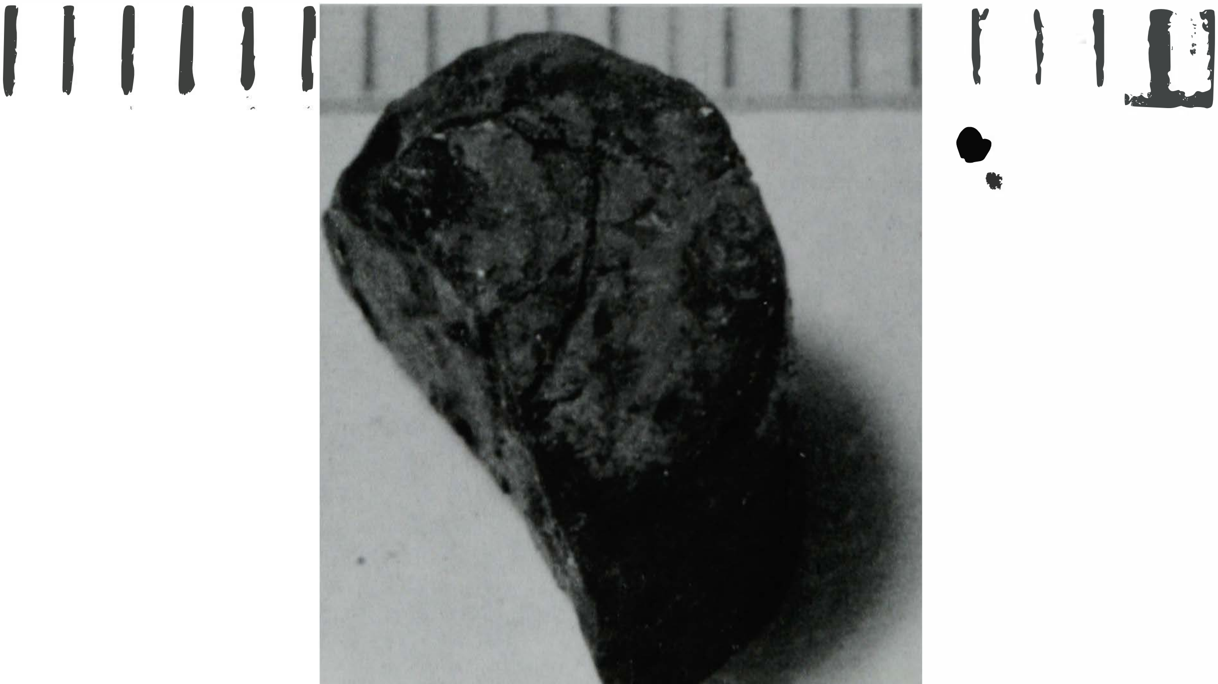

b. Particle 4D (size range: >4000 µm).

84-157-2-32

Figure A-9. Particles from Sample 4 (surface of debris bed at E9 core location).

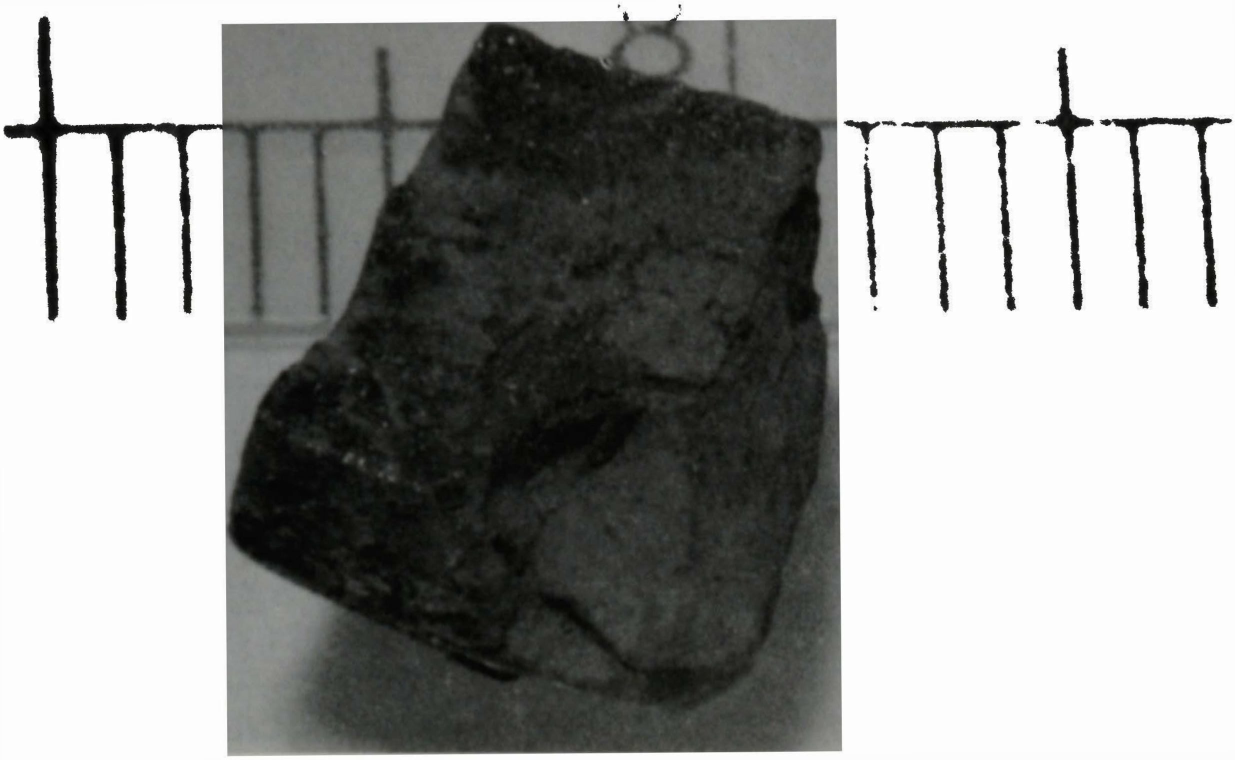

a. Front view of particle.

84-157-3-4

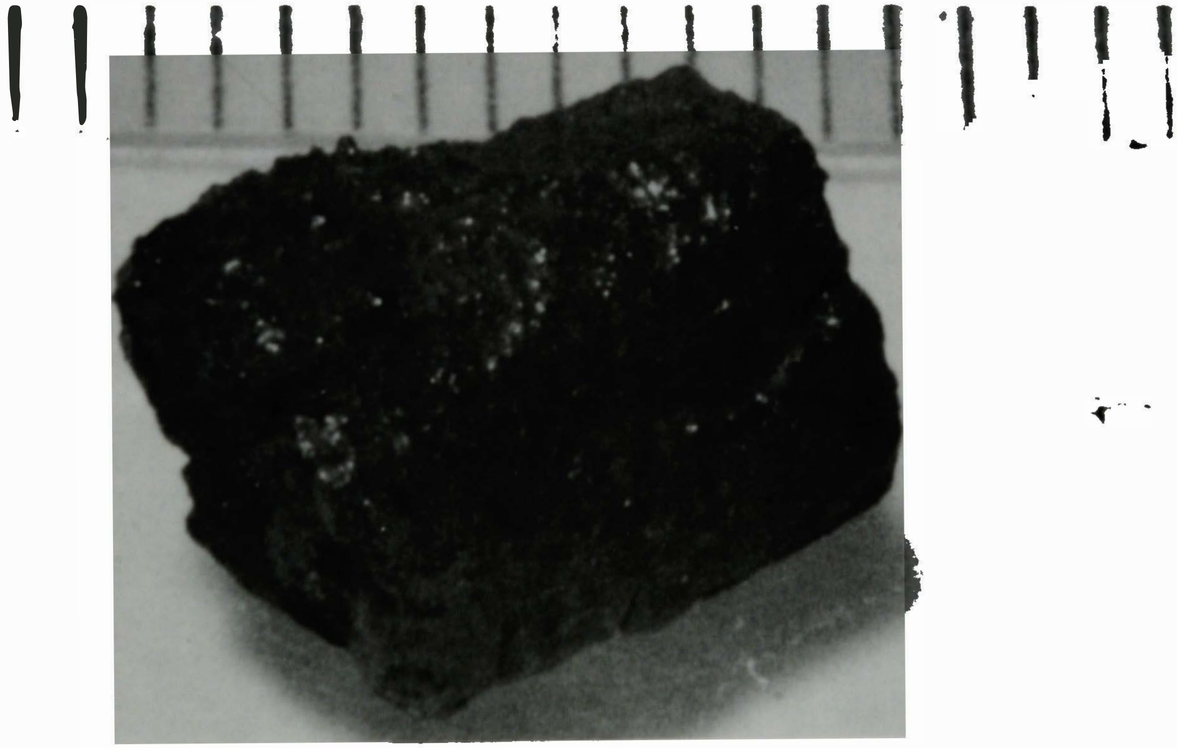

b. Back view of particle.

84-157-3-8

Figure A-10. Particle 4E from Sample 4 (surface of debris bed at E9 core location), size range: >4000 μm.

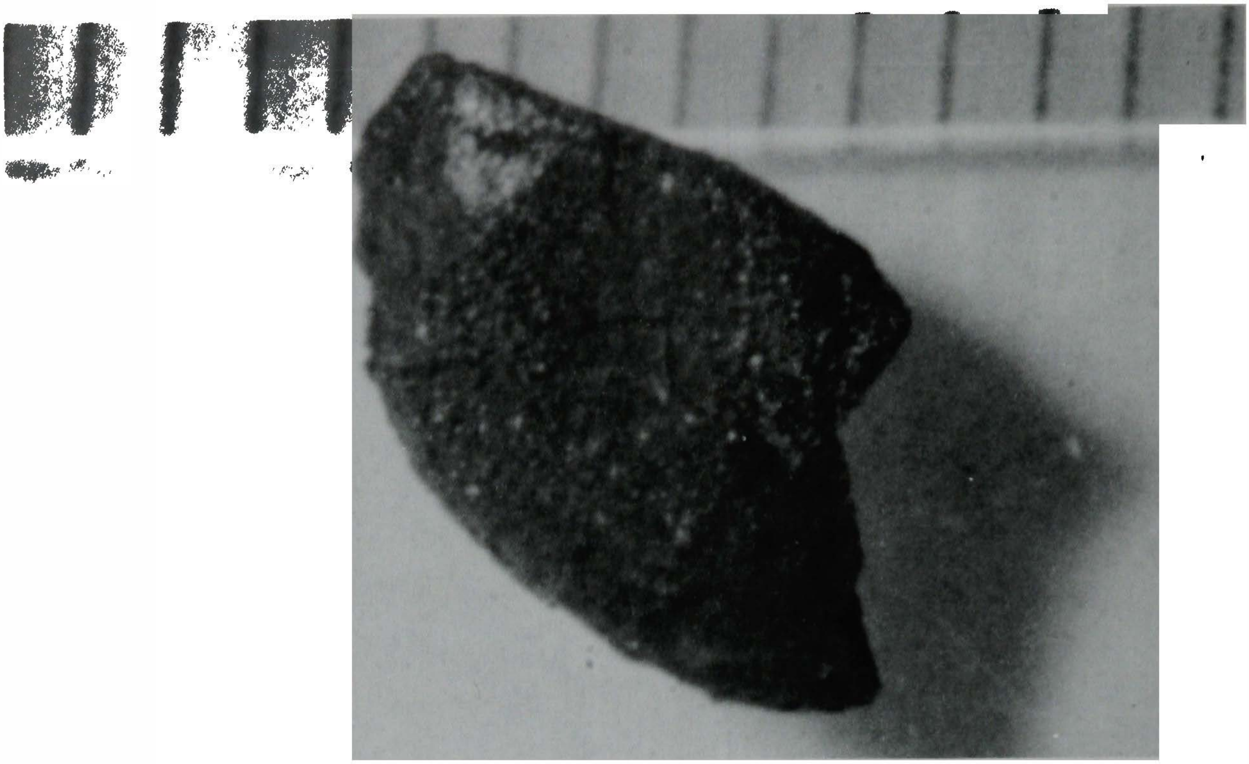

a. Front view of particle. 84-194-1-19

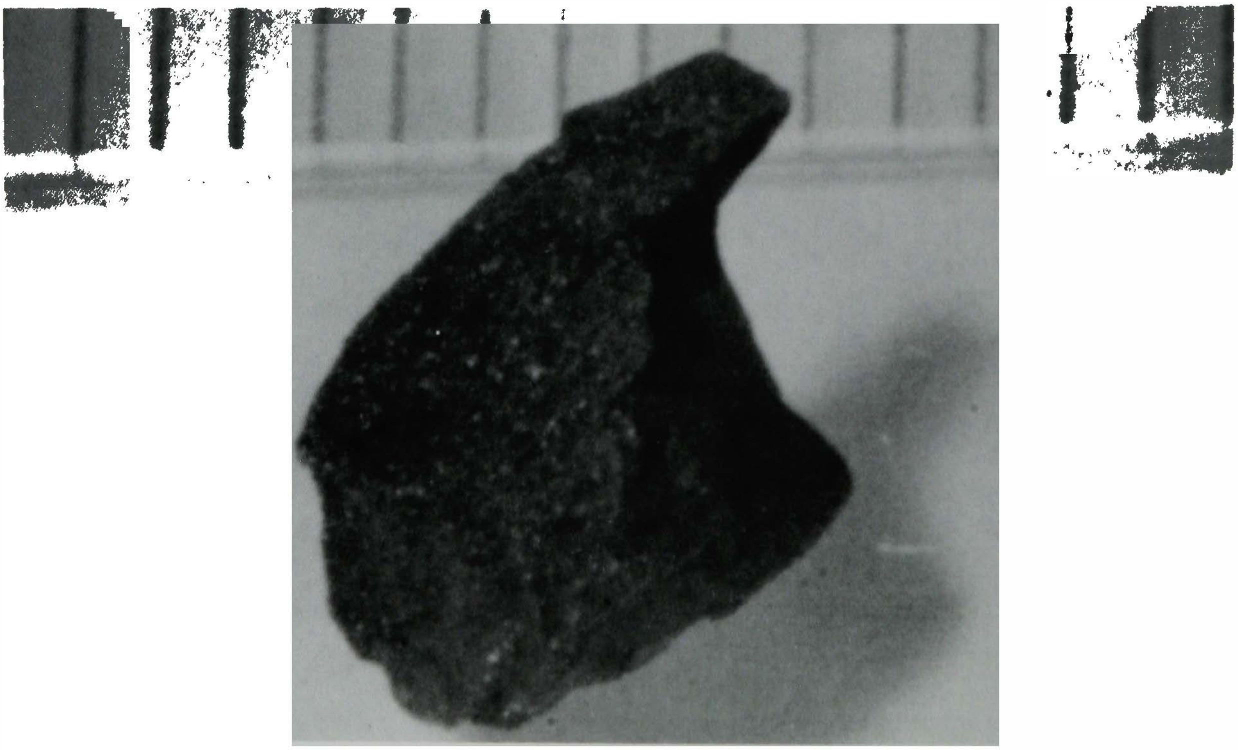

b. Back view of particle. 84-194-1-27

Figure A-11. Particle 5A from Sample 5 (3 in. into debris bed at E9 core location), size range: >4000 µm.

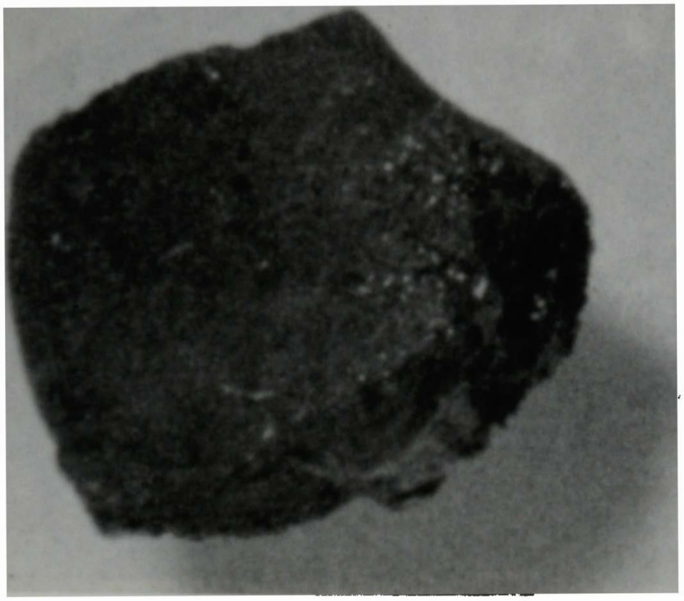

a. Particle 5B (size range: >4000 μm).

84-194-1-30

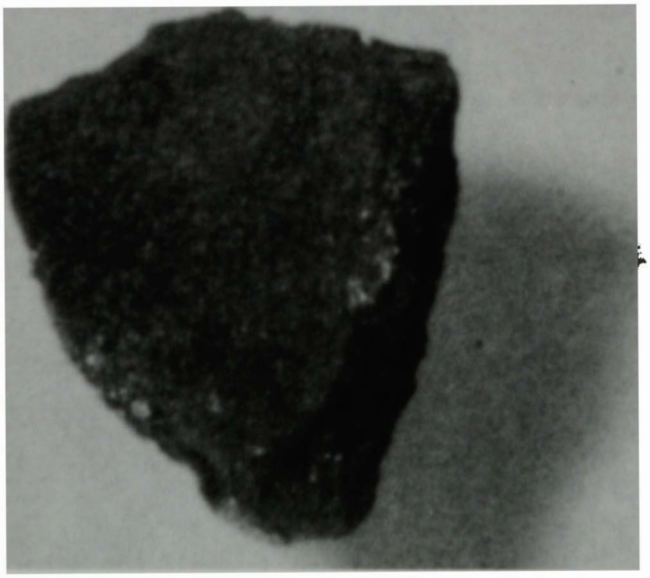

b. Particle 5C (size range: >4000 μm).

84-194-2-8

Figure A-12. Particles from Sample 5 (3 in. into debris bed at E9 core location).

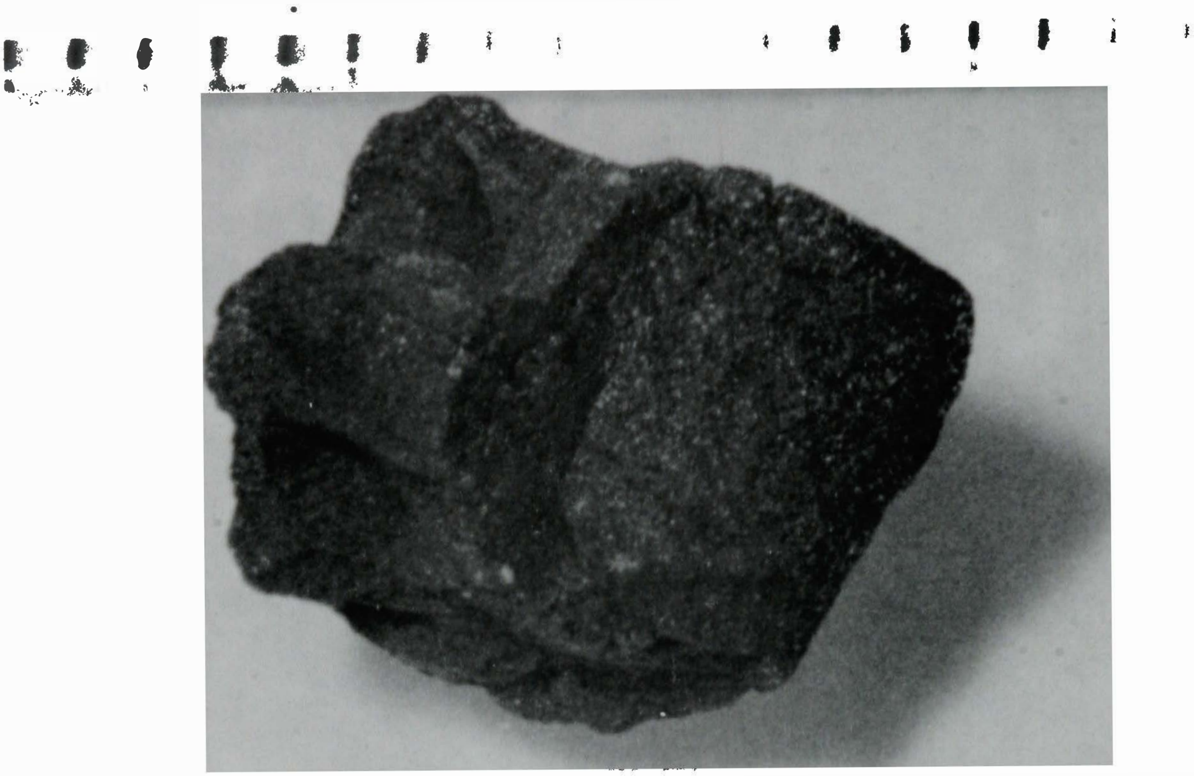

a. Particle 5D (size range: >4000 μm).

84-194-2-15

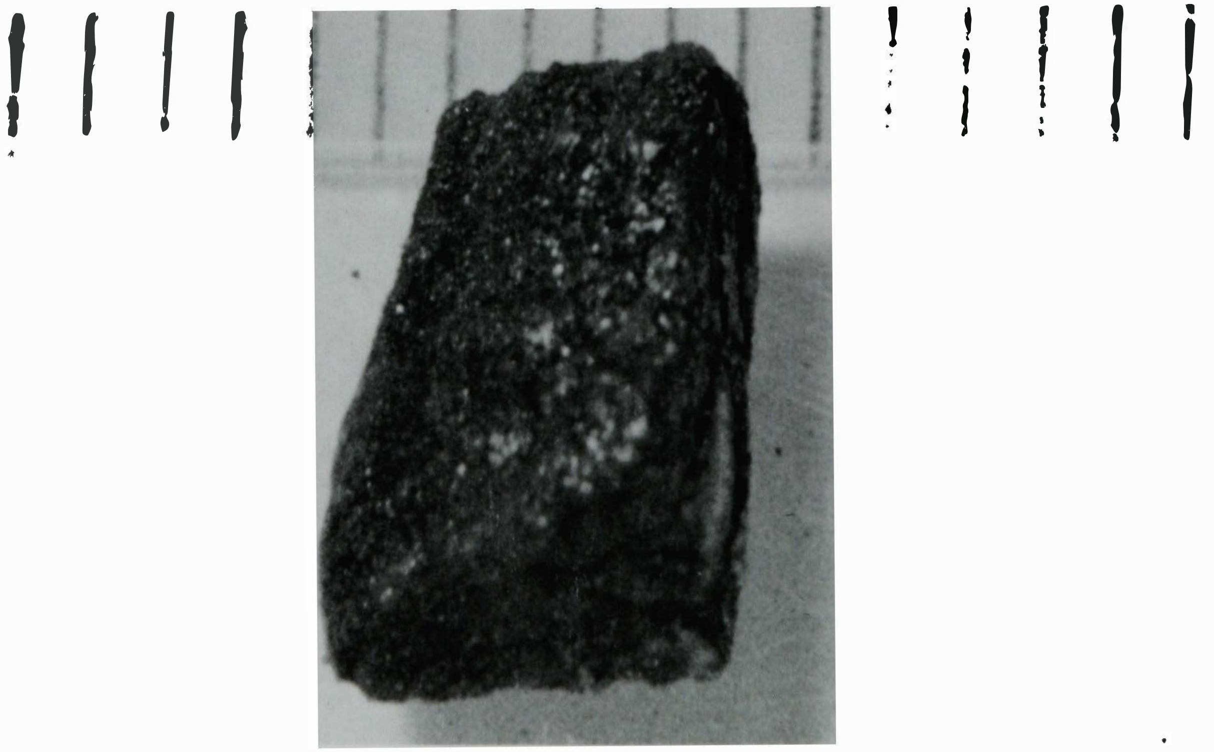

b. Particle 5E (size range: >4000 μm).

84-194-2-24

Figure A-13. Particles from Sample 5 (3 in. into debris bed at E9 core location).

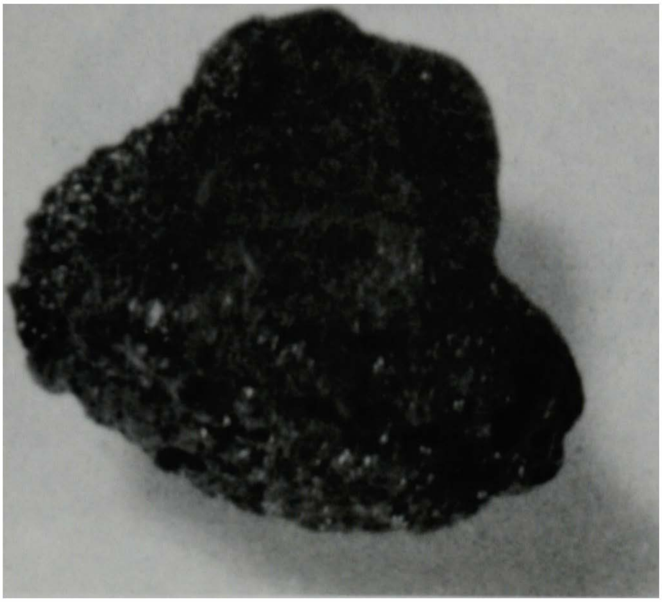

a. Particle 5F (size range: >4000 µm).

84-194-2-27

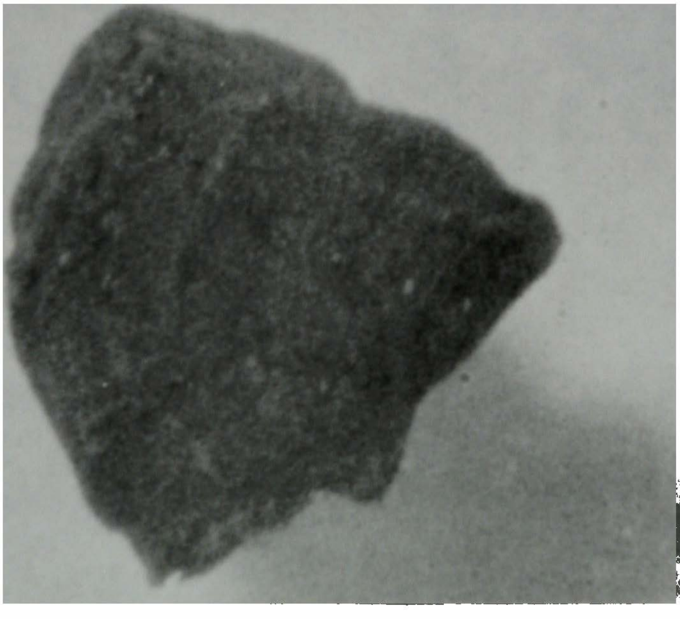

b. Particle 5G (size range: >4000 µm).

84-194-3-4

Figure A-14. Particles from Sample 5 (3 in. into debris bed at E9 core location).

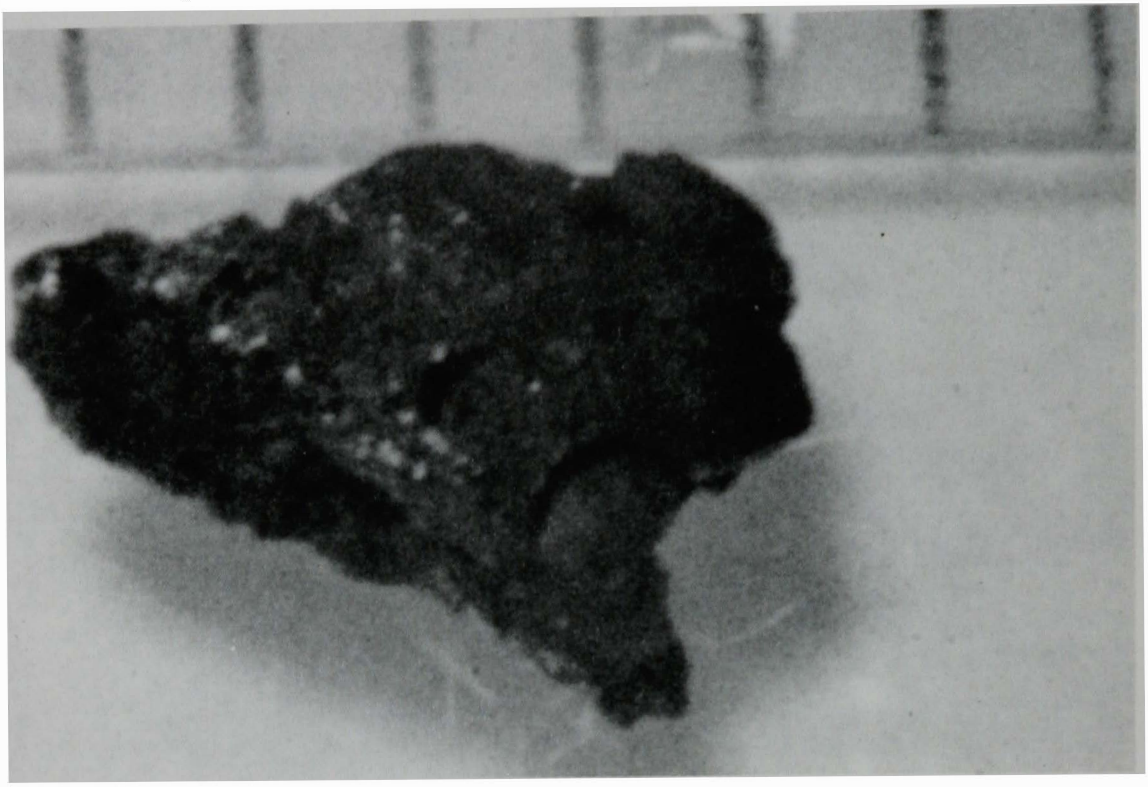

84-194-3-19

a. Particle 5H (size range: 1000-1680 μm).

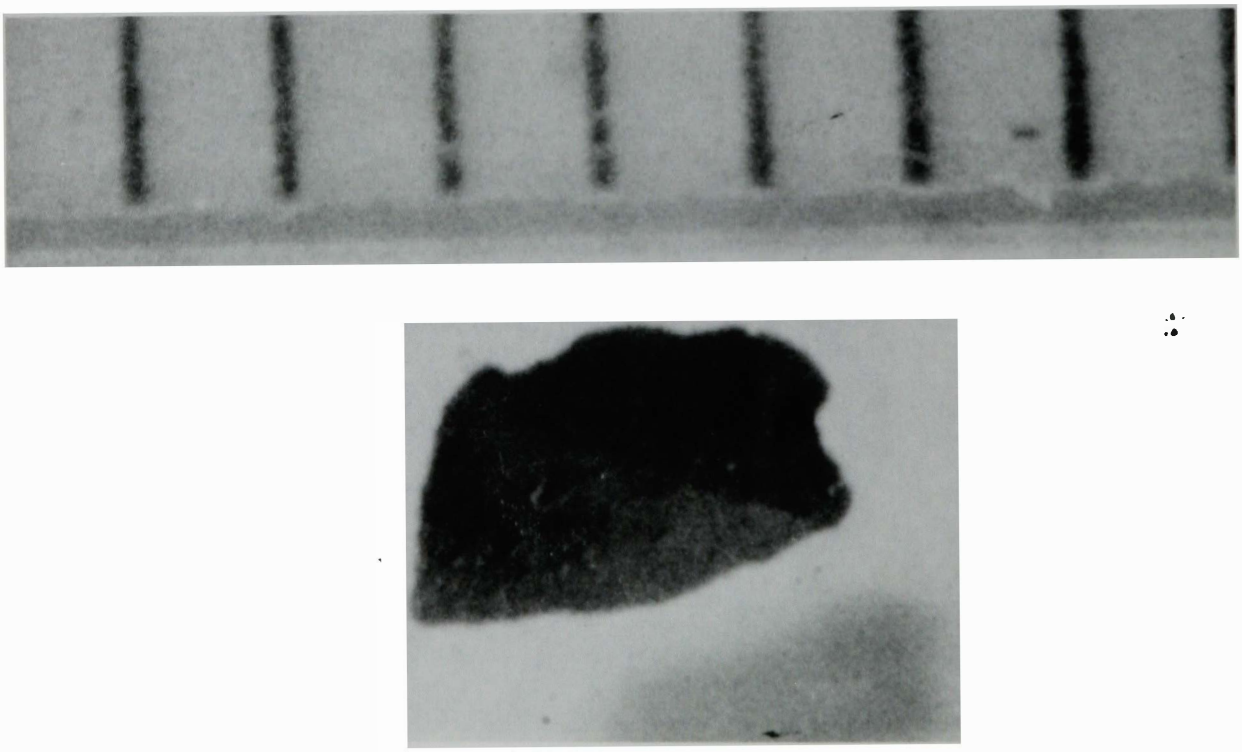

84-172-1-22

b. Particle 5I (size range: 1000-1680 μm).

Figure A-15. Particles from Sample 5 (3 in. into debris bed at E9 core location).

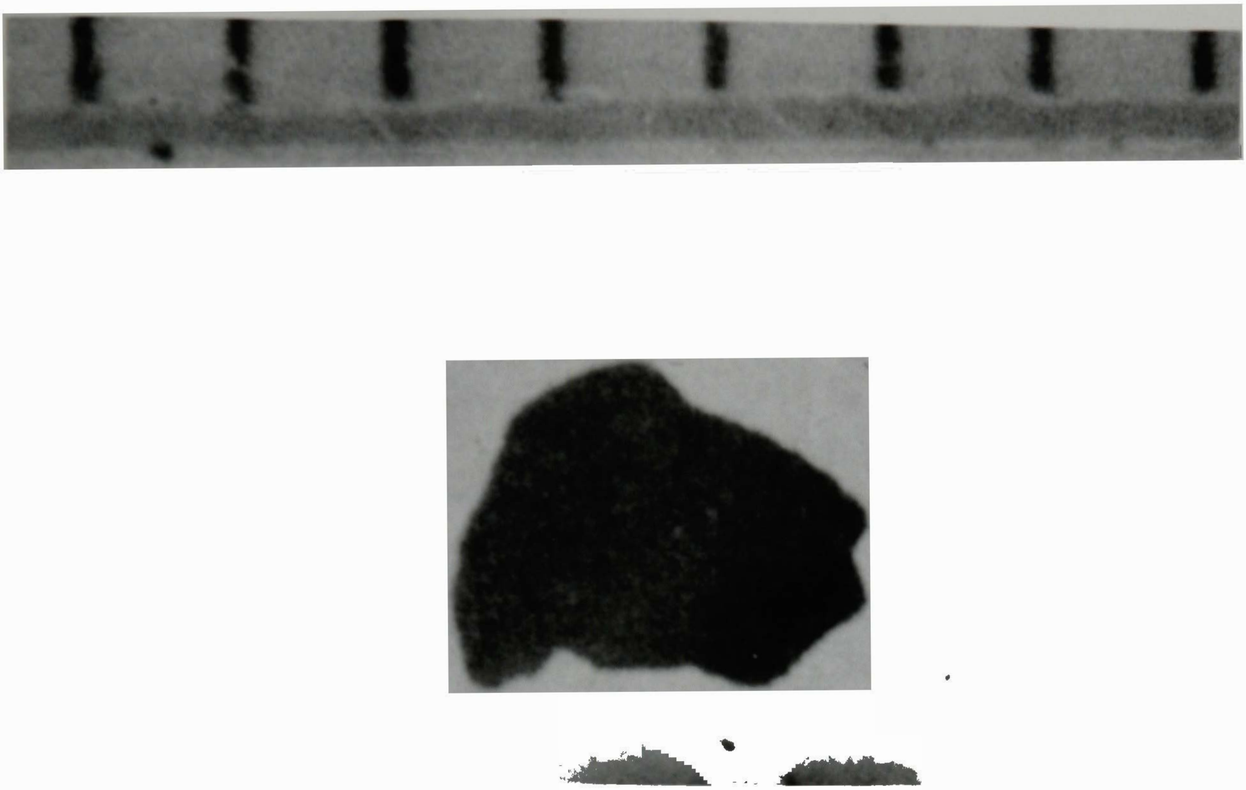

a. Particle 5J (size range: 1000-1680 μm). 84-172-1-24

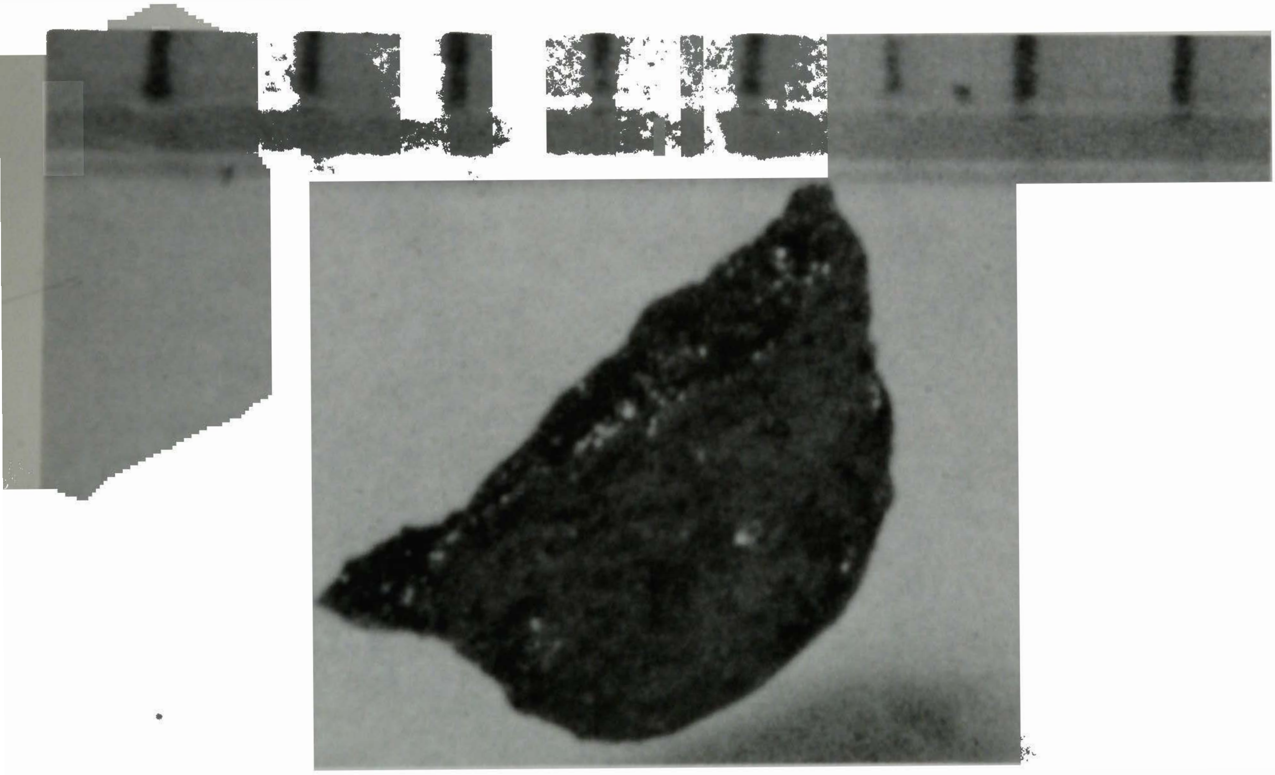

b. Particle 5K (size range: 1000-1680 μm). 84-122-1-26

Figure A-16. Particles from Sample 5 (3 in. into debris bed at E9 core location).

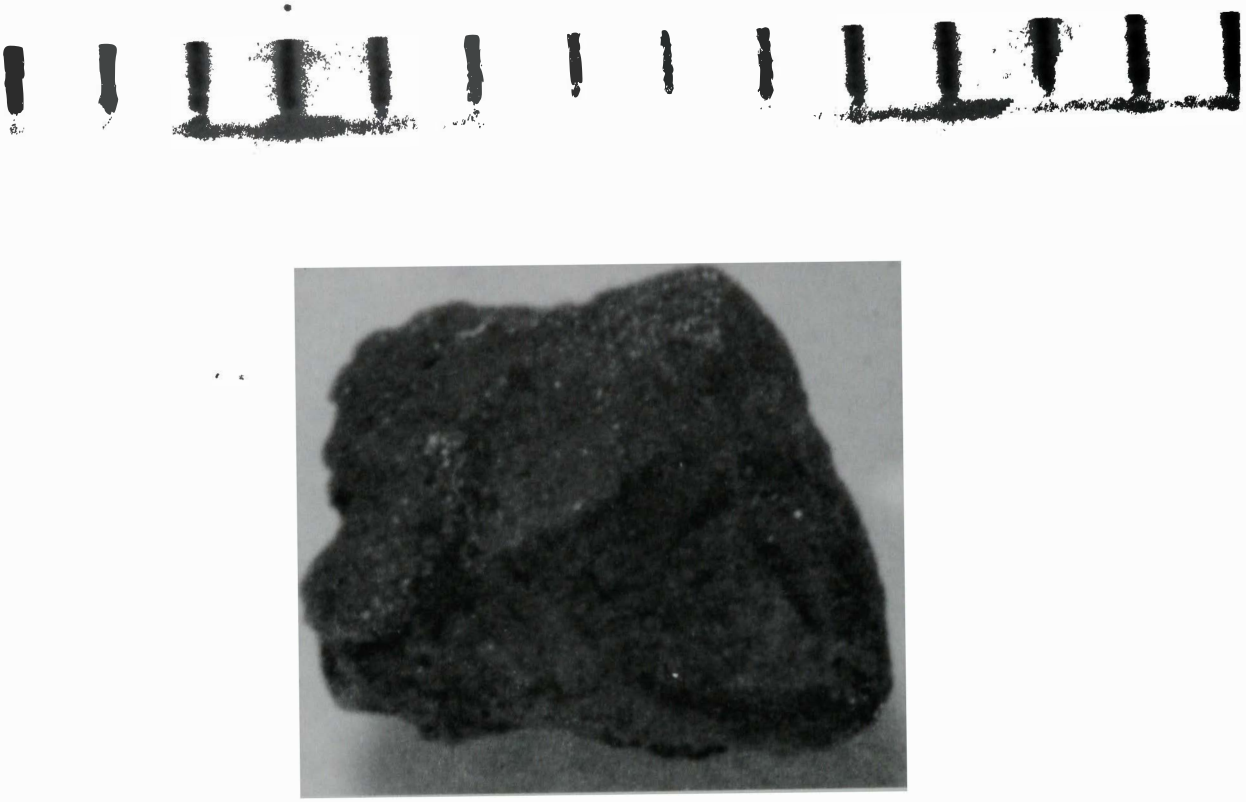

84-199-3-4

a. Front view of particle.

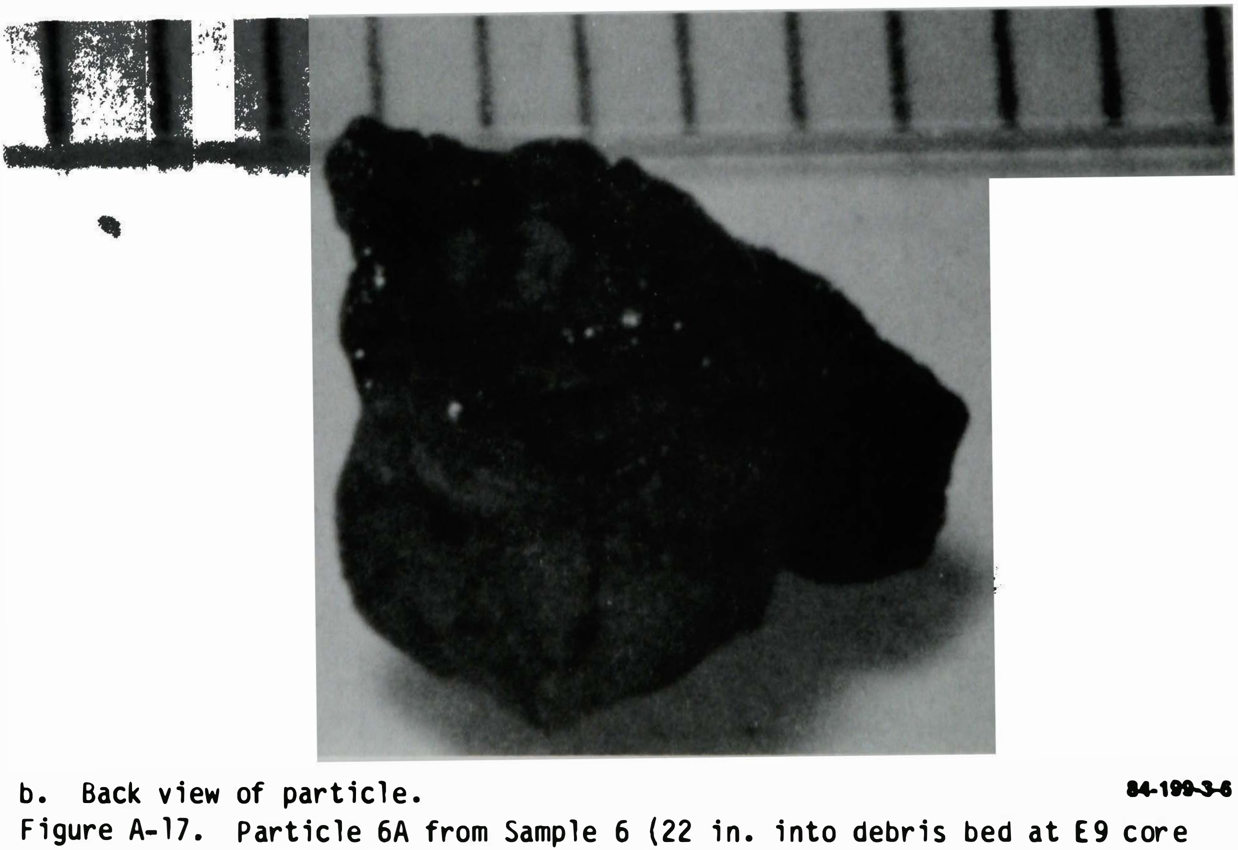

b. Back view of particle.

84-199-3-6

Figure A-17. Particle 6A from Sample 6 (22 in. into debris bed at E9 core location), size range: >4000 μm.

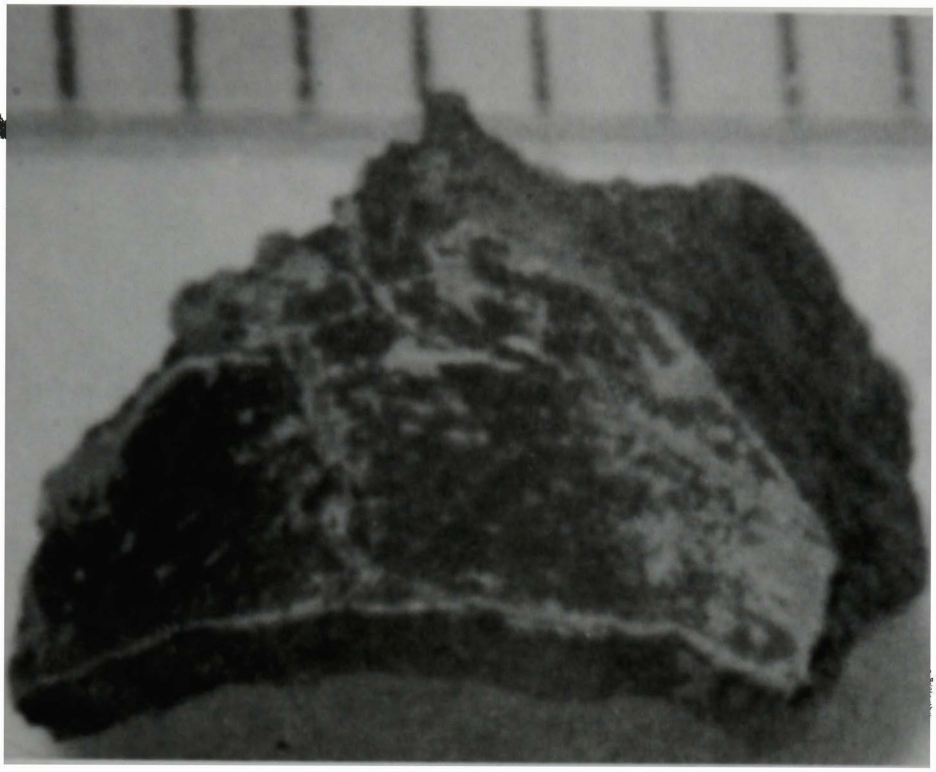

a. Particle 6B (size range: >4000 µm).

84-199-3-12

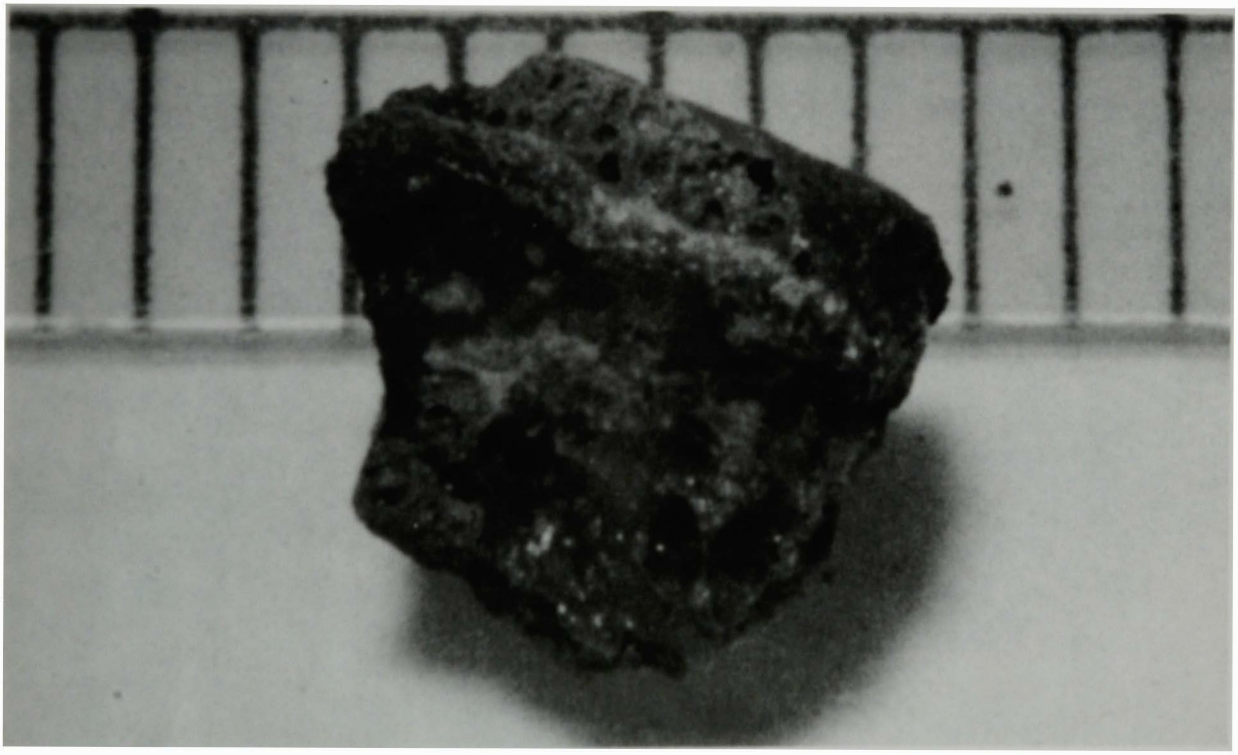

b. Particle 6C (size range: >4000 µm).

84-199-3-15

Figure A-18. Particles from Sample 6 (22 in. into debris bed at E9 core location).

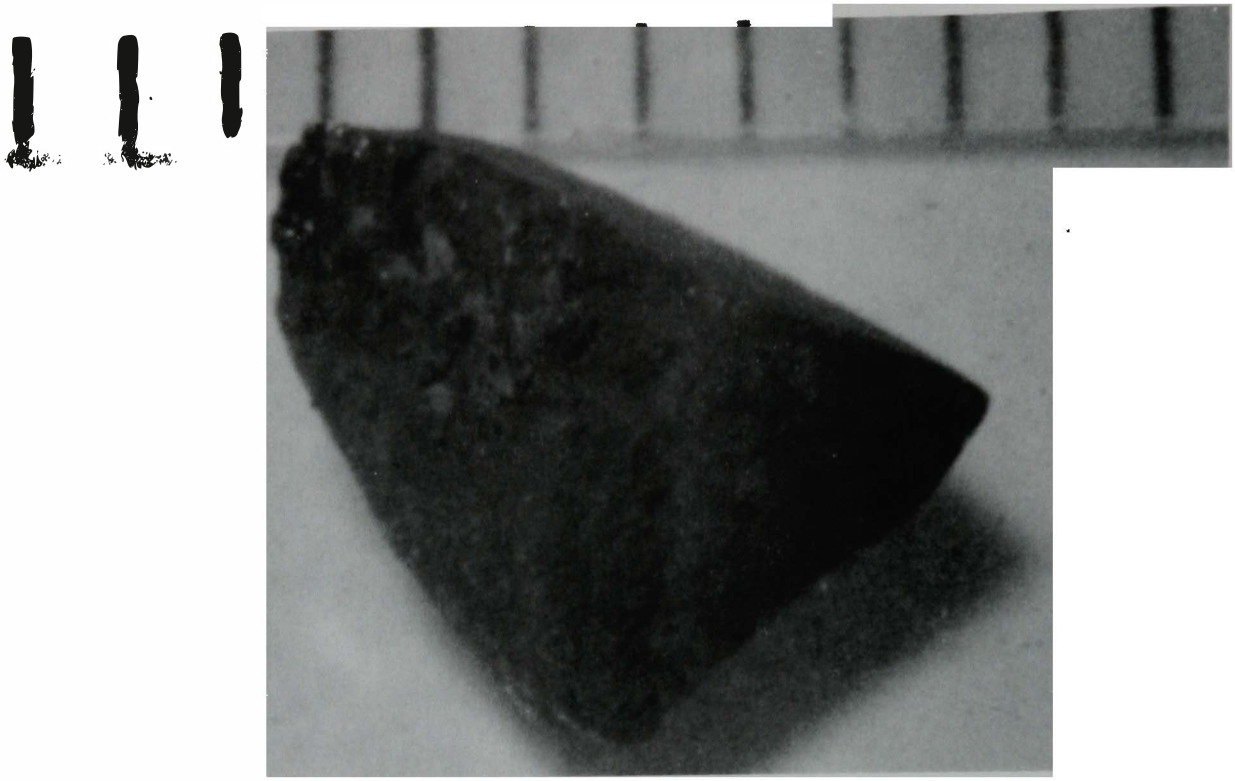

a. Front view of particle.

84-199-3-19

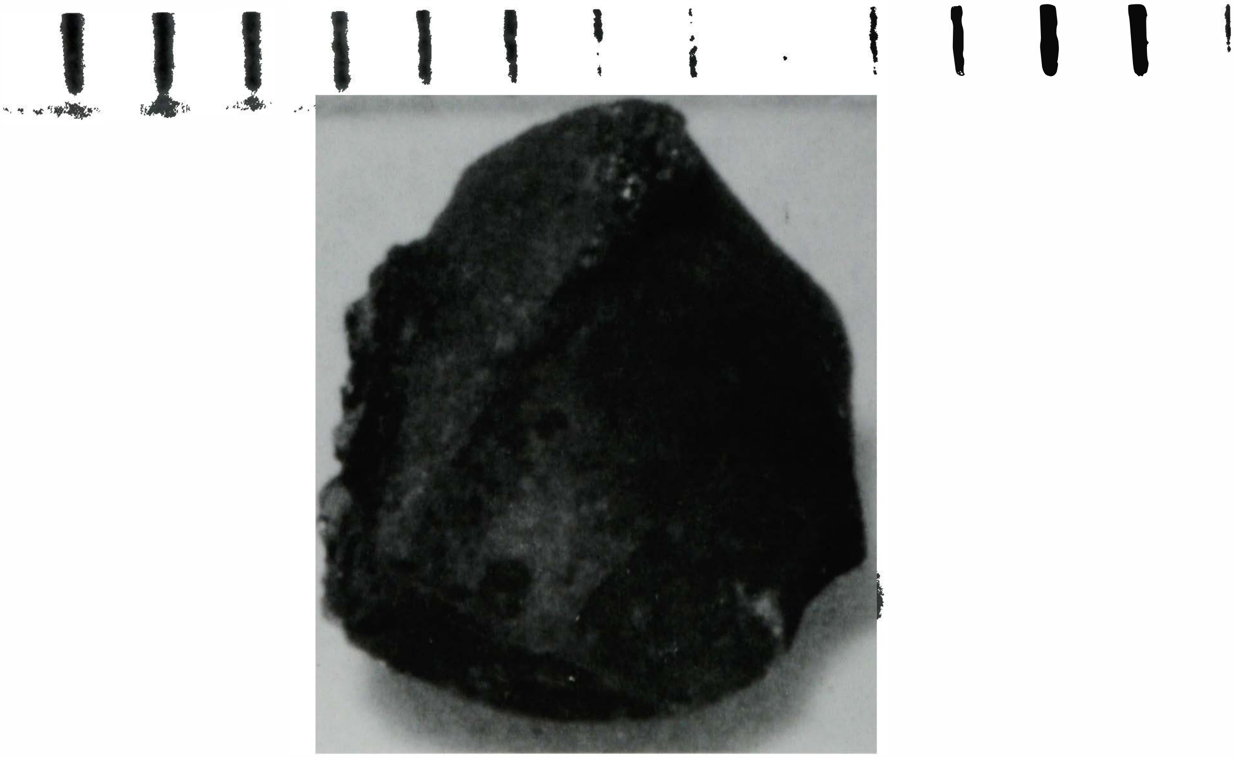

b. Back view of particle.

84-199-3-21

Figure A-19. Particle 6D from Sample 6 (22 in. into debris bed at E9 core location), size range: >4000 μm.

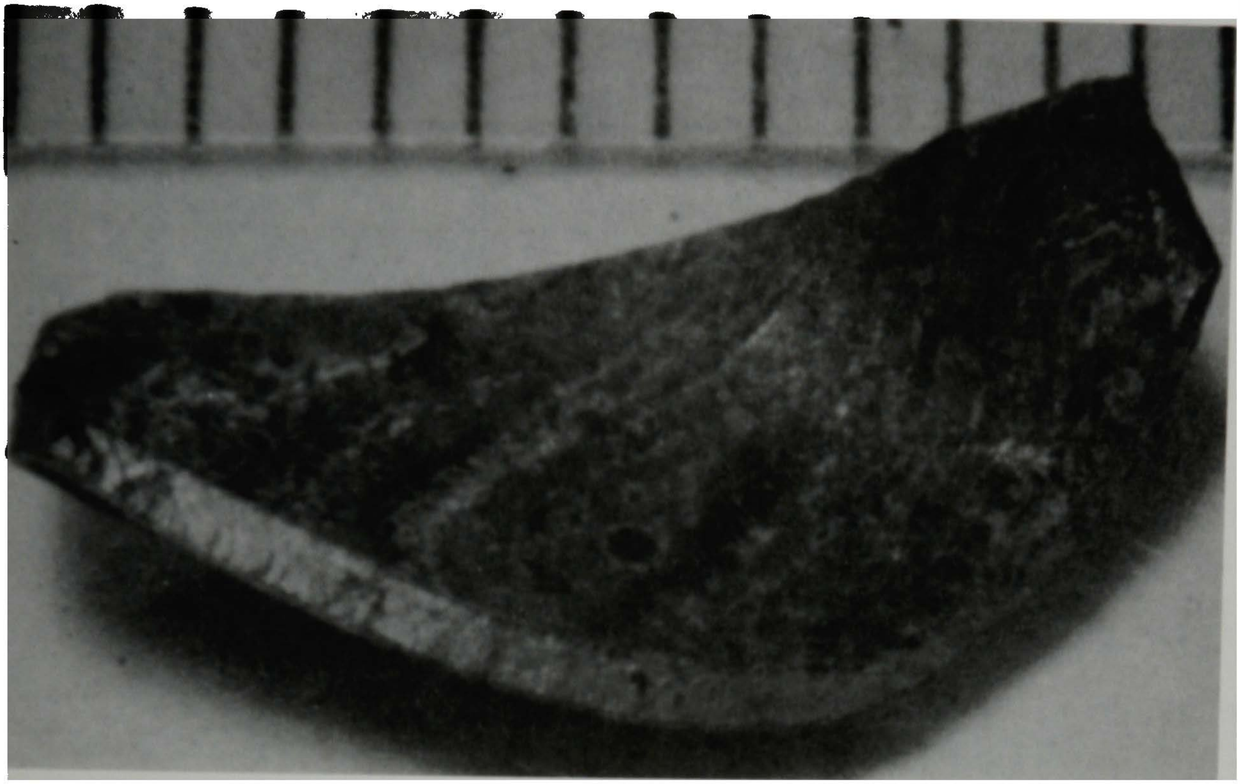

a. Front view of particle.

84-199-3-24

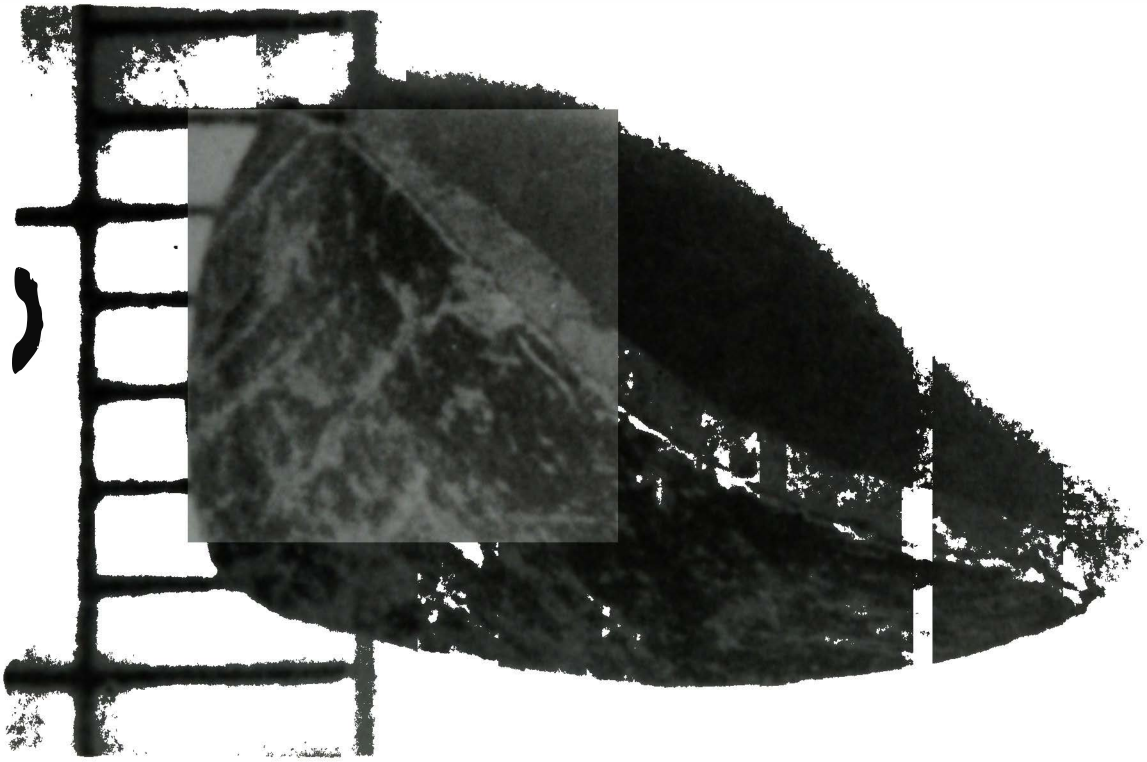

b. Back view of particle.

84-199-3-28

Figure A-20. Particle 6E from Sample 6 (22 in. into debris bed at E9 core location), size range: >4000µm.

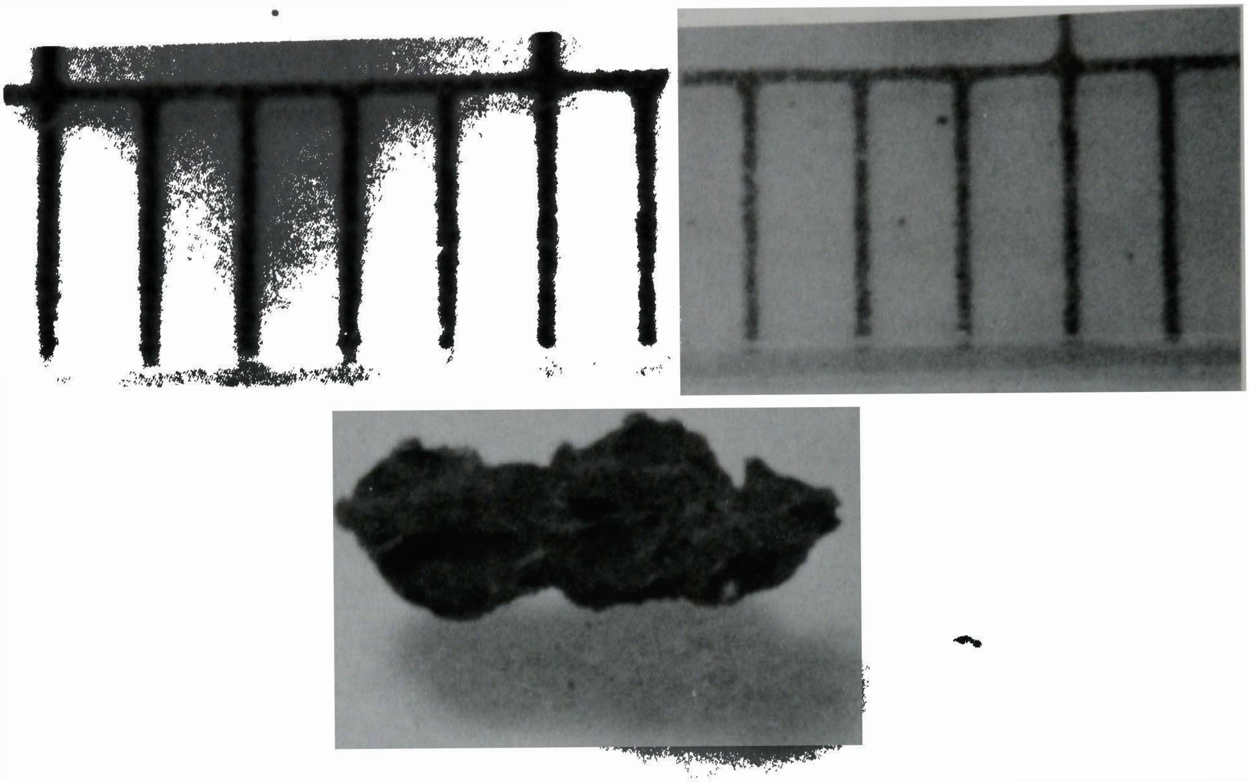

84-199-4-6

a. Particle 6F (size range: 1680-4000 μm).

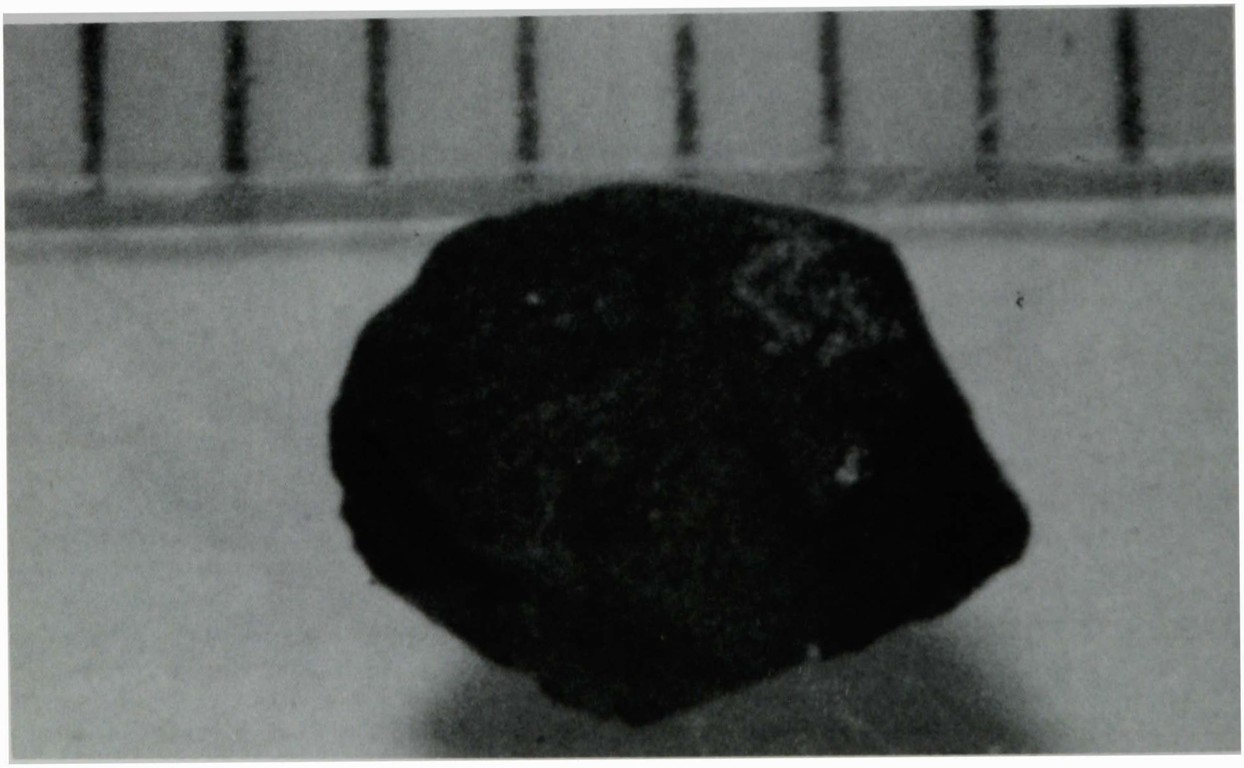

84-199-4-8

b. Particle 6G (size range: 1680-4000 μm).

Figure A-21. Particles from Sample 6 (22 in. into debris bed at E9 core location).

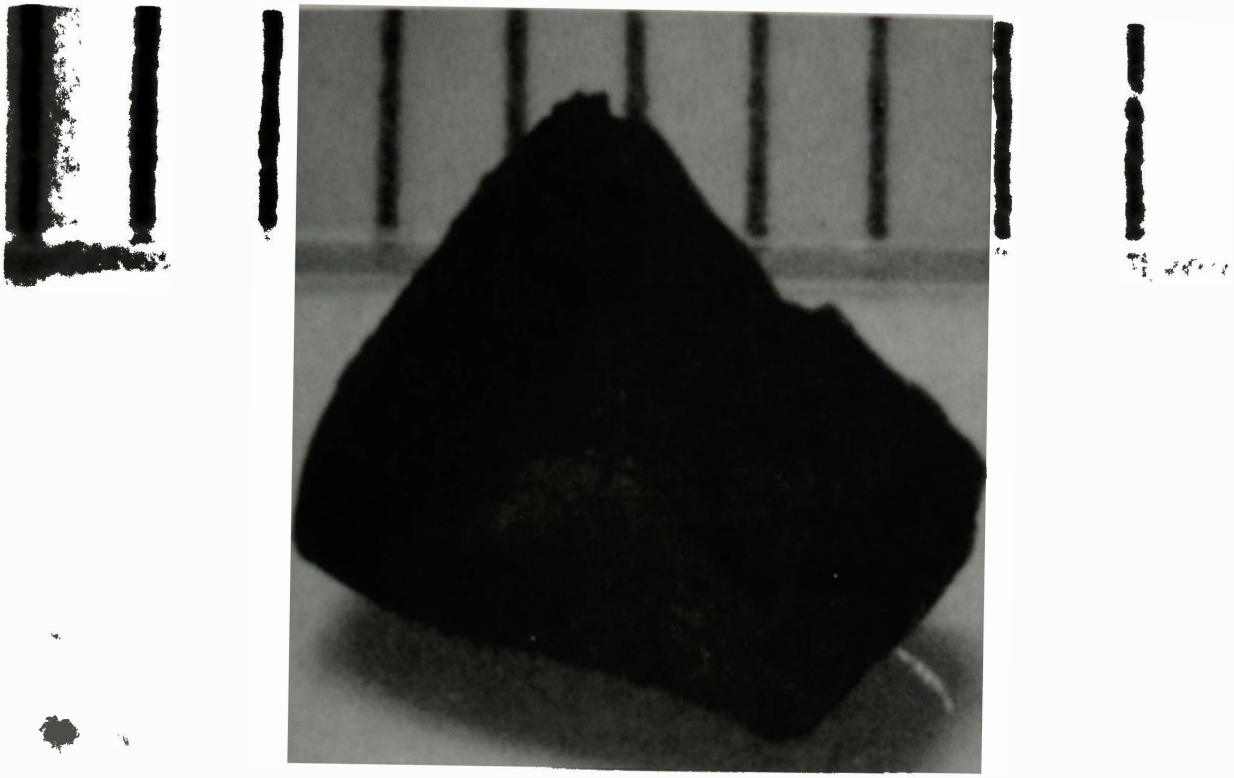

a. Particle 6H (size range: 1680-4000 µm). 84-199-4-10

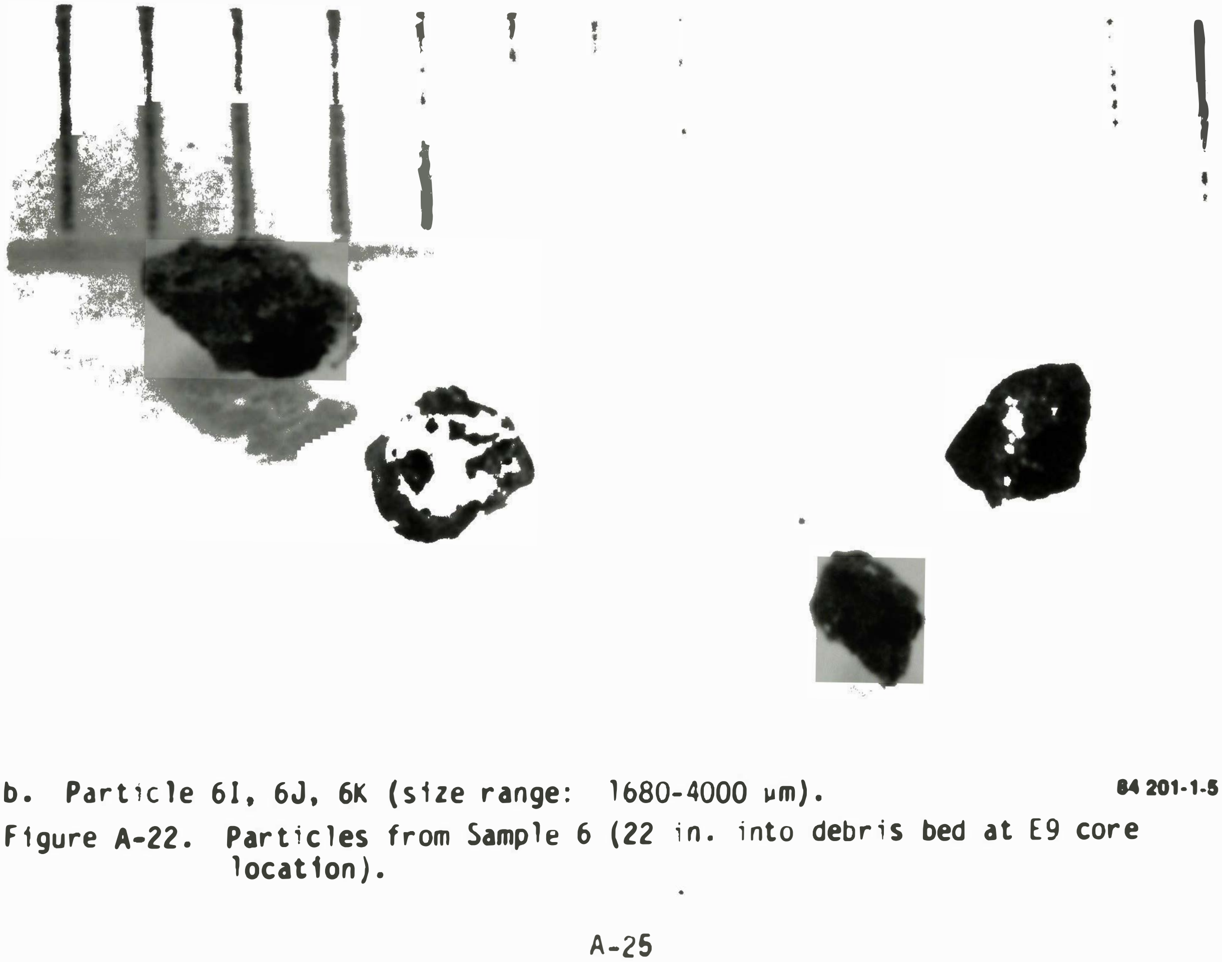

b. Particle 6I, 6J, 6K (size range: 1680-4000 µm). 84 201-1-5

Figure A-22. Particles from Sample 6 (22 in. into debris bed at E9 core location).

APPENDIX B

GAMMA SPECTROMETRY DATA

APPENDIX B

GAMMA SPECTROMETRY DATA

Included in this appendix are the gamma spectrometry results for the five core debris samples. The ^{241}Am is not reported because an effective correction factor has not yet been determined for this radionuclide. All uncertainties are reported at the one sigma value with only counting statistics incorporated, with the exception of ^{155}Eu. The ^{155}Eu data are based on extrapolated correction factors and have a listed uncertainty of 20%. The data are decay corrected to 1 April 1984, and the weights of individual samples are tabulated in Appendix C.

TABLE B-1. SAMPLE 1 RADIONUCLIDE CONCENTRATIONS[a] (μCi/g)

	Particle Size Fraction (μm)				
Radionuclide	>4000 Particle 1A	>4000 Particle 1B	>4000 Particle 1C	>4000 Particle 1D	>4000 Particle 1E
^{60}Co	2.55 ± 0.14 E+1	1.81 ± 0.19 E+1	8.7 ± 1.1 E+0	1.99 ± 0.31 E+1	1.37 ± 0.09 E+1
^{106}Ru	7.10 ± 0.40 E+1	1.55 ± 0.15 E+3	6.71 ± 0.86 E+1	8.99 ± 1.37 E+2	2.72 ± 0.18 E+2
^{110m}Ag	ND	ND	ND	ND	ND
^{125}Sb	1.20 ± 0.07 E+2	7.82 ± 0.82 E+1	1.23 ± 0.23 E+1	1.36 ± 0.22 E+1	9.24 ± 0.61 E+1
^{134}Cs	5.36 ± 0.31 E+0	3.69 ± 0.55 E+0	7.57 ± 0.86 E+1	1.08 ± 0.17 E+1	3.54 ± 0.23 E+1
^{137}Cs	2.98 ± 0.16 E+2	6.68 ± 0.67 E+1	1.31 ± 0.15 E+3	2.02 ± 0.31 E+2	8.38 ± 0.54 E+2
^{144}Ce	1.74 ± 0.14 E+2	3.84 ± 0.41 E+3	2.81 ± 0.34 E+3	3.14 ± 0.49 E+3	7.32 ± 0.59 E+2
^{154}Eu	7.98 ± 0.96 E-1	5.86 ± 0.61 E+1	4.78 ± 0.57 E+1	4.63 ± 0.71 E+1	1.05 ± 0.08 E+1
^{155}Eu	9.5 ± 1.9 E+0	1.6 ± 0.3 E+2	1.2 ± 0.2 E+2	1.25 ± 0.25 E+2	3.5 ± 0.7 E+1
^{60}Co	8.1 ± 0.8 E+0	9.34 ± 0.88 E+0	7.85 ± 0.49 E+1	1.67 ± 0.20 E+1	1.95 ± 0.11 E+0
^{106}Ru	4.39 ± 0.49 E+1	7.33 ± 0.74 E+1	1.07 ± 0.07 E+2	7.00 ± 0.85 E+1	8.9 ± 0.6 E+0
^{110m}Ag	ND	ND	ND	7.43 ± 0.92 E+0	ND
^{125}Sb	2.06 ± 0.23 E+1	1.84 ± 0.24 E+1	1.48 ± 0.13 E+1	2.17 ± 0.25 E+2	1.1 ± 0.1 E+0
^{134}Cs	1.12 ± 0.09 E+2	9.98 ± 0.86 E+1	6.29 ± 0.44 E+0	6.29 ± 0.72 E+1	3.1 ± 0.2 E+0

TABLE B-1. (continued)

	Particle Size Fraction (μm)				
Radionuclide	1680-4000 Particle 1F	1680-4000 Particle 1G	1680-4000 Particle 1H	1000-1680 Particle 1I	1000-1680 Particle 1J
$^{137}\mathrm{Cs}$	1.98 ± 0.16 E+3	1.71 ± 0.15 E+3	1.15 ± 0.07 E+2	1.14 ± 0.13 E+3	5.5 ± 0.3 E+1
$^{144}\mathrm{Ce}$	3.06 ± 0.27 E+3	2.31 ± 0.22 E+3	2.18 ± 0.15 E+3	ND	3.20 ± 0.19 E+2
$^{154}\mathrm{Eu}$	5.73 ± 0.50 E+1	3.54 ± 0.33 E+1	3.02 ± 0.20 E+1	9.8 ± 2.5 E-1	5.4 ± 0.3 E+0
$^{155}\mathrm{Eu}$	1.24 ± 0.25 E+2	9.5 ± 1.9 E+1	8.3 ± 1.8 E+1	ND	1.2 ± 0.2 E+1
$^{60}\mathrm{Co}$	8.2 ± 0.7 E+0	2.3 ± 0.2 E+2	4.9 ± 0.3 E+1	8.1 ± 0.6 E+1	1.1 ± 0.1 E+2
$^{106}\mathrm{Ru}$	4.6 ± 0.4 E+1	5.6 ± 0.4 E+3	1.5 ± 0.1 E+2	1.5 ± 0.1 E+2	2.7 ± 0.3 E+2
$^{110m}\mathrm{Ag}$	ND	3.7 ± 0.9 E+0	1.1 ± 0.2 E+0	1.3 ± 0.3 E+0	1.8 ± 0.4 E+0
$^{125}\mathrm{Sb}$	4.9 ± 0.8 E+0	1.91 ± 0.13 E+2	2.22 ± 0.14 E+2	3.4 ± 0.2 E+2	4.8 ± 0.5 E+2
$^{134}\mathrm{Cs}$	5.1 ± 0.4 E+0	5.6 ± 0.4 E+1	2.7 ± 0.2 E+1	4.4 ± 0.3 E+1	5.1 ± 0.5 E+1
$^{137}\mathrm{Cs}$	8.7 ± 0.7 E+1	1.06 ± 0.4 E+3	6.5 ± 0.4 E+2	9.1 ± 0.6 E+2	1.0 ± 0.1 E+3
$^{144}\mathrm{Ce}$	2.5 ± 0.2 E+3	2.3 ± 0.2 E+3	2.4 ± 0.2 E+3	1.55 ± 0.12 E+3	1.7 ± 0.2 E+3
$^{154}\mathrm{Eu}$	4.8 ± 0.4 E+1	4.5 ± 0.4 E+1	4.3 ± 0.3 E+1	2.4 ± 0.2 E+1	3.4 ± 0.4 E+1
$^{155}\mathrm{Eu}$	1.0 ± 0.2 E+2	1.1 ± 0.2 E+2	9.7 ± 1.9 E+1	6.7 ± 1.3 E+1	6.9 ± 1.4 E+1

TABLE B-1. (continued)

	Particle Size Fraction (µm)
Radionuclide	30-74 Aliquot
^{60}Co	6.56 ± 0.47 E+1
^{106}Ru	1.09 ± 0.08 E+2
^{110m}Ag	1.01 ± 0.18 E+0
^{125}Sb	2.03 ± 0.14 E+2
^{134}Cs	3.24 ± 0.23 E+1
^{137}Cs	6.14 ± 0.43 E+2
^{144}Ce	7.12 ± 0.65 E+2
^{154}Eu	1.13 ± 0.10 E+1
^{155}Eu	2.56 ± 0.50 E+1

ND = radionuclide not detected.

TABLE B-2. SAMPLE 3/RADIONUCLIDE CONCENTRATIONS
(μCi/g)

	Particle Size Fraction (μm)				
Radionuclide	>4000 Particle 3A	>4000 Particle 3B	>4000 Particle 3C	>4000 Particle 3D	>4000 Particle 3E
^{60}Co	4.67 ± 0.27 E+1	5.94 ± 0.41 E+1	1.30 ± 0.08 E+1	2.03 ± 0.29 E+0	1.33 ± 0.24 E+0
^{106}Ru	6.25 ± 0.36 E+2	3.76 ± 0.35 E+0	4.03 ± 0.24 E+2	1.46 ± 0.08 E+3	1.43 ± 0.08 E+3
^{110m}Ag	ND	ND	ND	ND	ND
^{125}Sb	4.63 ± 0.29 E+1	6.95 ± 0.50 E+0	1.86 ± 0.13 E+1	1.34 ± 0.08 E+2	1.25 ± 0.08 E+2
^{134}Cs	3.25 ± 0.26 E+0	5.00 ± 0.42 E-1	2.23 ± 0.18 E+0	5.66 ± 0.32 E+1	5.19 ± 0.30 E+1
^{137}Cs	5.87 ± 0.34 E+1	1.17 ± 0.08 E+1	4.65 ± 0.28 E+1	9.49 ± 0.52 E+2	8.36 ± 0.47 E+2
^{144}Ce	1.77 ± 0.12 E+3	5.79 ± 0.52 E+1	1.75 ± 0.11 E+3	3.73 ± 0.24 E+3	3.92 ± 0.25 E+3
^{154}Eu	3.00 ± 0.19 E+1	7.15 ± 0.75E-1	2.24 ± 0.14 E+1	6.67 ± 0.41 E+1	6.83 ± 0.42 E+1
^{155}Eu	7.4 ± 1.5 E+1	2.92 ± 0.59 E+0	6.99 ± 0.43 E+1	1.59 ± 0.32 E+2	1.36 ± 0.27 E+2
^{60}Co	3.3 ± 0.5 E+0	6.41 ± 0.75 E+0	8.6 ± 1.0 E+0	7.13 ± 0.49 E+1	1.62 ± 0.19 E+1
^{106}Ru	2.6 ± 0.3 E+3	1.81 ± 0.21 E+2	5.06 ± 0.66 E+1	2.39 ± 0.17 E+2	1.45 ± 0.17 E+2
^{110m}Ag	ND	ND	ND	ND	ND
^{125}Sb	9.6 ± 1.1 E+1	1.88 ± 0.22 E+1	6.1 ± 1.8 E+0	4.45 ± 0.38 E+1	1.69 ± 0.21 E+1
^{134}Cs	4.4 ± 0.5 E+1	1.06 ± 0.12 E+1	9.2 ± 1.0 E+1	4.80 ± 0.33 E+1	4.59 ± 0.55 E+0
^{137}Cs	7.5 ± 0.9 E+2	3.95 ± 0.45 E+2	1.58 ± 0.18 E+3	9.32 ± 0.63 E+2	7.28 ± 0.83 E+1

TABLE B-2. (continued)

Radionuclide	Particle Size Fraction (μm) 1000-1680 Particle 3K	707-1000 Aliquot	297-707 Aliquot	149-297 Aliquot	74-149 Aliquot
^{144}Ce	7.0 ± 0.8 E+3	5.70 ± 0.69 E+2	2.17 ± 0.26 E+3	2.55 ± 0.19 E+3	9.3 ± 1.3 E+2
^{154}Eu	1.18 ± 0.14 E+2	4.34 ± 0.55 E+0	3.55 ± 0.42 E+1	4.29 ± 0.31 E+1	1.65 ± 0.20 E+1
^{155}Eu	3.1 ± 0.6 E+2	2.82 ± 0.33 E+1	7.8 ± 1.6 E+1	1.13 ± 0.23 E+2	4.05 ± 0.47 E+1
^{60}Co	6.41 ± 0.41 E+0	9.21 ± 0.59 E+1	2.21 ± 0.18 E+1	6.61 ± 0.37 E+1	8.59 ± 0.61 E+1
^{106}Ru	4.17 ± 0.28 E+1	2.07 ± 0.14 E+2	1.19 ± 0.09 E+2	3.09 ± 0.17 E+2	2.33 ± 0.17 E+2
^{110m}Ag	ND	ND	ND	ND	1.22 ± 0.33 E+0
^{125}Sb	9.00 ± 0.81 E+0	3.37 ± 0.25 E+1	1.93 ± 0.19 E+1	1.09 ± 0.06 E+2	1.93 ± 0.14 E+2
^{134}Cs	1.16 ± 0.07 E+1	3.10 ± 0.20 E+1	3.50 ± 0.27 E+1	4.31 ± 0.24 E+1	5.15 ± 0.37 E+1
^{137}Cs	2.05 ± 0.12 E+2	5.40 ± 0.34 E+2	8.35 ± 0.65 E+2	9.00 ± 0.49 E+2	9.05 ± 0.64 E+2
^{144}Ce	2.53 ± 0.16 E+3	2.38 ± 0.16 E+3	1.80 ± 0.15 E+3	1.64 ± 0.10 E+3	1.48 ± 0.12 E+3
^{154}Eu	4.69 ± 0.28 E+1	4.46 ± 0.30 E+1	3.16 ± 0.26 E+1	2.59 ± 0.16 E+1	2.30 ± 0.19 E+1
^{155}Eu	1.10 ± 0.22 E+2	1.00 ± 0.20 E+2	3.83 ± 0.31 E+1	8.2 ± 1.6 E+3	6.3 ± 1.3 E+1

TABLE B-2. (continued)

	Particle Size Fraction (μm)	
Radionuclide	30-74 Aliquot	<30 Aliquot
^{60}Co	1.40 ± 0.09 E+2	1.02 ± 0.26 E+2
^{106}Ru	6.50 ± 0.44 E+2	2.46 ± 0.63 E+2
^{110m}Ag	ND	ND
^{125}Sb	2.21 ± 0.15 E+2	1.78 ± 0.46 E+2
^{134}Cs	5.16 ± 0.35 E+1	2.87 ± 0.74 E+1
^{137}Cs	8.90 ± 0.60 E+2	6.6 ± 1.7 E+2
^{144}Ce	1.19 ± 0.09 E+3	7.5 ± 2.0 E+2
^{154}Eu	1.73 ± 0.14 E+1	1.05 ± 0.28 E+1
^{155}Eu	4.9 ± 1.0 E+1	3.07 ± 0.79 E+1

ND = radionuclide not detected.

TABLE B-3. SAMPLE 4 RADIONUCLIDE CONCENTRATIONS
(μCi/g)

Radionuclide	Particle 4A	Particle 4B	Particle 4C	Particle 4D	Particle 4E
^{60}Co	1.42 ± 0.16 E+2	1.13 ± 0.07 E+1	2.51 ± 0.17 E+2	2.75 ± 0.51 E+0	2.71 ± 0.27 E+1
^{106}Ru	3.35 ± 0.38 E+3	2.38 ± 0.15 E+2	6.00 ± 0.41 E+2	1.47 ± 0.18 E+3	1.87 ± 0.20 E+3
^{110m}Ag	ND	ND	ND	ND	ND
^{125}Sb	2.00 ± 0.24 E+2	6.81 ± 0.53 E+0	4.94 ± 0.38 E+1	1.51 ± 0.19 E+2	8.77 ± 0.98 E+1
^{134}Cs	1.02 ± 0.12 E+2	1.73 ± 0.13 E+0	1.34 ± 0.10 E+1	1.75 ± 0.22 E+2	3.33 ± 0.36 E+1
^{137}Cs	1.71 ± 0.19 E+3	3.57 ± 0.22 E+1	3.65 ± 0.24 E+2	3.92 ± 0.48 E+3	5.46 ± 0.58 E+2
^{144}Ce	8.6 ± 1.0 E+3	7.74 ± 0.53 E+2	2.51 ± 0.19 E+3	4.60 ± 0.59 E+3	5.18 ± 0.56 E+3
^{154}Eu	1.50 ± 0.17 E+2	9.32 ± 0.6 E+0	2.03 ± 0.16 E+1	6.05 ± 0.78 E+1	8.64 ± 0.93 E+1
^{155}Eu	3.15 ± 0.63 E+2	2.96 ± 0.59 E+1	1.07 ± 0.21 E+2	6.2 ± 1.2 E+1	1.76 ± 0.19 E+2

ND = radionuclide not detected.

TABLE B-4. SAMPLE 5 RADIONUCLIDE CONCENTRATIONS (μCi/g)

Radionuclide	Particle Size Fraction (μm)				
	>4000 Particle 5A	>4000 Particle 5B	>4000 Particle 5C	>4000 Particle 5D	>4000 Particle 5E
^{60}Co	3.77 ± 0.67 E+1	4.51 ± 0.31 E+1	3.94 ± 0.28 E+1	2.81 ± 0.25 E+0	1.20 ± 0.09 E+2
^{106}Ru	2.21 ± 0.39 E+3	1.25 ± 0.08 E+3	1.04 ± 0.07 E+3	5.40 ± 0.36 E+2	1.19 ± 0.08 E+3
^{110m}Ag	ND	ND	ND	ND	ND
^{125}Sb	1.67 ± 0.30 E+2	1.47 ± 0.10 E+2	2.47 ± 0.24 E+1	3.86 ± 0.28 E+1	3.00 ± 0.22 E+2
^{134}Cs	2.33 ± 0.42 E+1	1.53 ± 0.11 E+1	9.55 ± 0.75 E+0	2.25 ± 0.15 E+1	6.78 ± 0.55 E+0
^{137}Cs	3.92 ± 0.69 E+2	2.95 ± 0.20 E+2	1.64 ± 0.11 E+2	6.89 ± 0.45 E+2	1.48 ± 0.11 E+2
^{144}Ce	6.6 ± 1.2 E+3	3.84 ± 0.27 E+3	3.15 ± 0.24 E+3	1.81 ± 0.13 E+3	2.13 ± 0.17 E+3
^{154}Eu	1.20 ± 0.21 E+2	5.93 ± 0.42 E+1	4.27 ± 0.32 E+1	1.58 ± 0.12 E+1	3.82 ± 0.29 E+1
^{155}Eu	2.72 ± 0.54 E+2	1.33 ± 0.27 E+2	1.35 ± 0.27 E+2	8.1 ± 1.6 E+1	9.9 ± 2.0 E+1

TABLE B-4. (continued)

	Particle Size Fraction (μm)				
Radionuclide	1680-4000 Particle 5F	1680-4000 Particle 5G	1680-4000 Particle 5H	1000-1680 Particle 5I	1000-1680 Particle 5J
^{60}Co	2.07 ± 0.19 E+0	3.10 ± 0.18 E+1	1.0 ± 0.2 E+2	6.57 ± 0.40 E-1	1.09 ± 0.18 E+0
^{106}Ru	5.58 ± 0.34 E+2	6.93 ± 0.38 E+2	2.8 ± 0.5 E+3	1.44 ± 0.09 E+3	1.29 ± 0.09 E+3
^{110m}Ag	ND	ND	ND	ND	ND
^{125}Sb	6.35 ± 0.40 E+1	1.32 ± 0.11 E+1	6.1 ± 0.1 E+2	1.02 ± 0.07 E+2	1.16 ± 0.08 E+2
^{134}Cs	2.92 ± 0.18 E+1	2.86 ± 0.26 E+0	3.6 ± 0.6 E+2	3.17 ± 0.20 E+1	3.29 ± 0.23 E+1
^{137}Cs	7.90 ± 0.47 E+2	3.78 ± 0.21 E+1	6.5 ± 1.1 E+3	5.08 ± 0.31 E+2	5.36 ± 0.37 E+2
^{144}Ce	1.86 ± 0.12 E+3	2.36 ± 0.14 E+3	1.1 ± 0.2 E+4	3.56 ± 0.25 E+3	3.40 ± 0.26 E+3
^{154}Eu	1.73 ± 0.12 E+1	2.94 ± 0.18 E+1	2.2 ± 0.4 E+2	6.26 ± 0.42 E+1	6.23 ± 0.45 E+1
^{155}Eu	7.4 ± 1.5 E+1	1.02 ± 0.20 E+2	5.1 ± 1.0 E+2	1.62 ± 0.32 E+2	1.39 ± 0.28 E+2

TABLE B-4. (continued)

	Particle Size Fraction (µm)
Radionuclide	<1000 Aliquot
^{60}Co	5.53 ± 0.34 E+1
^{106}Ru	6.53 ± 0.40 E+2
^{110m}Ag	ND
^{125}Sb	8.01 ± 0.55 E+1
^{134}Cs	9.85 ± 0.59 E+1
^{137}Cs	1.71 ± 0.10 E+3
^{144}Ce	2.24 ± 0.17 E+3
^{154}Eu	3.54 ± 0.25 E+1
^{155}Eu	1.06 ± 0.20 E+2

ND = radionuclide not detected.

TABLE B-5. SAMPLE 6 RADIONUCLIDE CONCENTRATIONS (µCi/g)

	Particle Size Fraction (µm)				
Radionuclide	>4000 Particle 6A	>4000 Particle 6B	>4000 Particle 6C	>4000 Particle 6D	>4000 Particle 6E
^{60}Co	6.07 ± 0.67 E+0	1.66 ± 0.09 E+0	3.34 ± 0.23 E+0	ND	1.24 ± 0.09 E+0
^{106}Ru	1.07 ± 0.11 E+3	2.39 ± 0.23 E+0	1.16 ± 0.07 E+2	9.15 ± 0.62 E+2	1.32 ± 0.14 E+0
^{110m}Ag	ND	ND	ND	ND	ND
^{125}Sb	9.74 ± 0.99 E+1	3.05 ± 0.17 E+2	4.22 ± 0.26 E+1	6.95 ± 0.53 E+1	2.40 ± 0.16 E+1
^{134}Cs	3.90 ± 0.39 E+1	7.11 ± 0.40 E+0	9.73 ± 0.59 E+0	5.47 ± 0.38 E+1	2.22 ± 0.15 E+0
^{137}Cs	1.19 ± 0.12 E+3	1.24 ± 0.07 E+3	1.82 ± 0.11 E+2	1.30 ± 0.09 E+3	4.41 ± 0.29 E+1
^{144}Ce	3.65 ± 0.38 E+3	2.84 ± 0.98 E+3	1.96 ± 0.17 E+2	2.66 ± 0.21 E+3	1.91 ± 0.38 E+0
^{154}Eu	2.88 ± 0.30 E+1	ND	2.93 ± 0.25 E+0	3.25 ± 0.25 E+1	ND
^{155}Eu	1.51 ± 0.30 E+2	2.21 ± 0.88 E+1	1.03 ± 0.07 E+1	1.16 ± 0.23 E+2	ND

TABLE B-5. (continued)

	Particle Size Fraction (μm)				
Radionuclide	1680-4000 Particle 6F	1680-4000 Particle 6G	1680-4000 Particle 6H	1000-1680 Particle 6I	1000-1680 Particle 6J
^{60}Co	4.89 ± 0.35 E+0	9.3 ± 2.1 E-1	ND	2.74 ± 0.16 E+2	7.33 ± 0.43 E+0
^{106}Ru	7.0 ± 1.0 E+0	1.03 ± 0.06 E+3	8.05 ± 0.45 E+2	2.64 ± 0.16 E+3	2.92 ± 0.16 E+2
^{110m}Ag	ND	ND	ND	ND	ND
^{125}Sb	1.46 ± 0.11 E+1	9.97 ± 0.66 E+1	8.16 ± 0.50 E+1	8.28 ± 0.49 E+1	1.78 ± 0.11 E+1
^{134}Cs	3.25 ± 0.20 E+1	1.69 ± 0.09 E+2	4.67 ± 0.26 E+1	2.08 ± 0.34 E+0	4.97 ± 0.57 E-1
^{137}Cs	6.22 ± 0.38 E+2	3.79 ± 0.21 E+3	1.07 ± 0.06 E+3	2.98 ± 0.18 E+1	1.10 ± 0.06 E+1
^{144}Ce	1.84 ± 0.35 E+1	3.06 ± 0.20 E+3	2.50 ± 0.16 E+3	3.20 ± 0.34 E+2	6.90 ± 0.44 E+2
^{154}Eu	ND	4.34 ± 0.28 E+1	2.46 ± 0.16 E+1	5.04 ± 0.64 E+0	1.34 ± 0.08 E+1
^{155}Eu	ND	1.37 ± 0.27 E+2	ND	2.7 E+0	4.2 E+0

TABLE B-5. (continued)

	Particle Size Fraction (μm)				
Radionuclide	1000-1680 Particle 6K	707-1000 Aliquot	297-707 Aliquot	149-297 Aliquot	74-149 Aliquot
^{60}Co	6.87 ± 0.55 E+0	1.43 ± 0.08 E+2	5.15 ± 0.29 E+1	9.21 ± 0.59 E+1	1.11 ± 0.06 E+2
^{106}Ru	5.81 ± 0.35 E+2	4.20 ± 0.23 E+2	2.19 ± 0.13 E+2	2.94 ± 0.17 E+2	3.74 ± 0.21 E+2
^{110m}Ag	ND	ND	ND	ND	ND
^{125}Sb	8.15 ± 0.59 E+1	8.77 ± 0.52 E+1	9.77 ± 0.57 E+1	1.46 ± 0.08 E+2	1.89 ± 0.11 E+2
^{134}Cs	1.76 ± 0.10 E+2	5.66 ± 0.31 E+1	5.82 ± 0.32 E+1	5.36 ± 0.30 E+1	4.81 ± 0.27 E+1
^{137}Cs	4.06 ± 0.24 E+3	1.23 ± 0.07 E+3	1.13 ± 0.06 E+3	1.07 ± 0.06 E+3	9.58 ± 0.53 E+2
^{144}Ce	3.48 ± 0.24 E+3	2.29 ± 0.15 E+3	2.11 ± 0.15 E+3	1.40 ± 0.09 E+3	1.27 ± 0.09 E+3
^{154}Eu	5.07 ± 0.34 E+1	3.63 ± 0.22 E+1	3.55 ± 0.22 E+1	2.16 ± 0.14 E+1	2.14 ± 0.14 E+1
^{155}Eu	3.53 ± 0.24 E+1	1.07 ± 0.21 E+2	9.19 ± 1.80 E+1	6.7 ± 1.3 E+1	7.8 ± 1.6 E+1

TABLE B-5. (continued)

	Particle Size Fraction (µm)
Radionuclide	30-74 Aliquot
^{60}Co	1.25 ± 0.09 E+2
^{106}Ru	5.23 ± 0.37 E+2
^{110m}Ag	ND
^{125}Sb	1.67 ± 0.12 E+2
^{134}Cs	5.00 ± 0.35 E+1
^{137}Cs	9.54 ± 0.67 E+2
^{144}Ce	1.11 ± 0.09 E+3
^{154}Eu	1.83 ± 0.14 E+1
^{155}Eu	4.5 ± 0.9 E+1

ND = radionuclide not detected.

APPENDIX C

FISSILE/FERTILE MATERIAL ANALYSIS

APPENDIX C

FISSILE/FERTILE MATERIAL ANALYSIS

Fragmented pieces and aliquots from the core debris samples were analyzed by both gamma ray spectrometry and delayed neutron analysis. This appendix presents the preliminary results of the delayed neutron analysis. These results may change slightly because of changes in the calibration curves for these data. The analysis was performed by first measuring the total fissile/fertile material contents using a fast neutron flux at the Coupled Fast Reactivity Measurement Facility (CFRMF) and subsequently measuring the fissile material content (i.e., $^{235}U + ^{239}Pu$) in a thermal neutron flux field at CFRMF. It has been determined that the ^{239}Pu component is negligible (<0.2 wt%), and, therefore, the component principally measured is ^{235}U. The effect of the ^{239}Pu is the increase in the measured fissile material content (5 to 8%).

TABLE C-1. FISSILE/FERTILE MATERIAL CONTENT

Particle Size Fraction (μm)	Particle/Aliquot	Fertile (mg)	Fissile (mg)	Enrichment (wt%)	Particle/Aliquot Weight (mg)
Sample 1					
>4000	Particle 1A	7.9 ± 0.6 E+0	2.4 ± 0.2 E-1	3.0 ± 0.3 E+0	84
>4000	Particle 1B	1.10 ± 0.07 E+1	2.3 ± 0.2 E-1	2.0 ± 0.2 E+0	12
>4000	Particle 1C	5.70 ± 0.6 E+0	1.4 ± 0.2 E-1	2.4 ± 0.4 E+0	10
>4000	Particle 1D	5.9 ± 0.8 E+0	1.4 ± 0.2 E-1	2.4 ± 0.4 E+0	7
>4000	Particle 1E	5.5 ± 0.6 E+0	1.4 ± 0.2 E-1	2.5 ± 0.4 E+0	29
1680-4000	Particle 1F	1.09 ± 0.07 E+1	2.6 ± 0.2 E-1	2.4 ± 0.2 E+0	16
1680-4000	Particle 1G	8.2 ± 0.7 E+0	1.7 ± 0.2 E-1	2.0 ± 0.3 E+0	15
1680-4000	Particle 1H	1.5 ± 0.1 E+1	4.2 ± 0.2 E-1	2.7 ± 0.2 E+0	33
1000-1680	Particle 1I	--	--	--	10
1000-1680	Particle 1J	1.46 ± 0.08 E+1	3.3 ± 0.2 E-1	2.2 ± 0.2 E+0	21
1000-1680	Particle 1K	1.00 ± 0.07 E+1	2.5 ± 0.2 E-1	2.5 ± 0.2 E+0	19
707-1000	Aliquot	1.65 ± 0.09 E+1	3.8 ± 0.2 E-1	2.2 ± 0.2 E+0	26
297-707	Aliquot	1.62 ± 0.09 E+1	4.1 ± 0.2 E-1	2.4 ± 0.2 E+0	29
149-297	Aliquot	9.0 ± 0.6 E+0	2.1 ± 0.2 E-1	2.3 ± 0.2 E+0	23
74-149	Aliquot	5.4 ± 0.6 E+0	1.2 ± 0.2 E-1	2.1 ± 0.4 E+0	12
30-74	Aliquot	3.9 ± 0.5 E+0	8.2 ± 1.7 E-2	2.1 ± 0.5 E+0	22
Sample 3					
>4000	Particle 3A	2.1 ± 0.1 E+1	6.2 ± 0.4 E-1	2.8 ± 0.2 E+0	56
>4000	Particle 3B	<0.7 E+0	<1.6 E-2	--	23
>4000	Particle 3C	NA	NA	NA	39
>4000	Particle 3D	7.9 ± 0.3 E+1	1.9 ± 0.06 E+0	2.3 ± 0.1 E+0	97
>4000	Particle 3E	5.6 ± 0.2 E+1	1.3 ± 0.04 E+0	2.3 ± 0.1 E+0	69

TABLE C-1. (continued)

Particle Size Fraction (μm)	Particle/Aliquot	Fertile (mg)	Fissile (mg)	Enrichment (wt%)	Particle/Aliquot Weight (mg)
Sample 3 (continued)					
1680-4000	Particle 3F	NA	NA	NA	10
1680-4000	Particle 3G	NA	NA	NA	10
1680-4000	Particle 3H	5.4 ± 0.7 E+0	1.0 ± 0.2 E-1	1.9 ± 0.4 E+0	10
1000-1680	Particle 3I	NA	NA	NA	25
1000-1680	Particle 3J	4.6 ± 0.6 E+0	1.2 ± 0.2 E-1	2.4 ± 0.4 E+0	24
1000-1680	Particle 3K	1.8 ± 0.1 E+1	6.4 ± 0.2 E-1	2.3 ± 0.1 E+0	45
707-1000	Aliquot	NA	NA	NA	30
297-707	Aliquot	NA	NA	NA	18
149-297	Aliquot	NA	NA	NA	114
74-149	Aliquot	NA	NA	NA	22
30-74	Aliquot	6.9 ± 0.7 E+0	1.8 ± 0.2 E-1	2.6 ± 0.4 E+0	25
20-30	Aliquot	1.3 ± 0.6 E+0	2.2 ± 1.6 E-2	1.7 ± 1.5 E+0	4
Sample 4					
>4000	Particle 4A	NA	NA	NA	10
>4000	Particle 4B	6.1 ± 0.6 E+0	2.1 ± 0.2 E-1	3.4 ± 0.5 E+0	33
>4000	Particle 4C	NA	NA	NA	28
>4000	Particle 4D	NA	NA	NA	9
>4000	Particle 4E	NA	NA	NA	11
Sample 5					
>4000	Particle 5A	NA	NA	NA	6
>4000	Particle 5B	2.3 ± 0.1 E+1	5.5 ± 0.2 E-1	2.4 ± 0.2 E+0	26
>4000	Particle 5C	NA	NA	NA	24
>4000	Particle 5D	NA	NA	NA	27
>4000	Particle 5E	7.7 ± 0.6 E+0	2.4 ± 0.2 E-1	3.0 ± 0.3 E+0	21

TABLE C-1. (continued)

Particle Size Fraction (μm)	Particle/Aliquot	Fertile (mg)	Fissile (mg)	Enrichment (wt%)	Particle/Aliquot Weight (mg)
Sample 5 (continued)					
1680-4000	Particle 5F	2.2 ± 0.1 E+1	6.5 ± 0.3 E-1	2.9 ± 0.2 E+0	39
1680-4000	Particle 5G	NA	NA	NA	89
1000-1680	Particle 5H	NA	NA	NA	6
1000-1680	Particle 5I	2.7 ± 0.1 E+1	8.1 ± 0.3 E-1	2.9 ± 0.2 E+0	37
1000-1680	Particle 5J	1.7 ± 0.9 E+1	4.5 ± 0.2 E-1	2.7 ± 0.2 E+0	24
<1000	Aliquot	1.9 ± 0.1 E+1	6.0 ± 0.3 E-1	3.0 ± 0.2 E+0	42.8
Sample 6					
>4000	Particle 6A	NA	NA	NA	12
>4000	Particle 6B	<0.16	<0.73	--	65
>4000	Particle 6C	1.4 ± 0.5 E+1	6.4 ± 0.2 E-1	4.4 ± 1.9 E+0	40
>4000	Particle 6D	1.9 ± 0.1 E+1	5.6 ± 0.2 E-1	2.9 ± 0.2 E+0	25
>4000	Particle 6E	<0.5	<0.02	--	26
1680-4000	Particle 6F	<0.5	<0.02	--	33
1680-4000	Particle 6G	7.3 ± 0.3 E+1	2.14 ± 0.06 E+0	2.8 ± 0.1 E+0	94
1680-4000	Particle 6H	8.6 ± 0.3 E+1	2.4 ± 0.07 E+0	2.7 ± 0.1 E+0	101
1000-1680	Particle 6I	4.0 ± 0.6 E+0	1.2 ± 0.2 E-1	3.0 ± 0.6 E+0	41
1000-1680	Particle 6J	8.9 ± 0.7 E+0	2.8 ± 0.2 E-1	3.1 ± 0.3 E+0	71
1000-1680	Particle 6K	3.1 ± 0.1 E+1	9.2 ± 0.3 E-1	2.8 ± 0.2 E+0	43
707-1000	Aliquot	7.7 ± 0.3 E+1	2.07 ± 0.06 E+0	2.6 ± 0.1 E+0	139

TABLE C-1. (continued)

Particle Size Fraction (μm)	Particle/Aliquot	Fertile (mg)	Fissile (mg)	Enrichment (wt%)	Particle/Aliquot Weight (mg)
Sample 6 (continued)					
297-707	Aliquot	6.9 ± 0.3 E+1	1.71 ± 0.05 E+0	2.4 ± 0.1 E+0	130
149-297	Aliquot	4.9 ± 0.2 E+1	1.75 ± 0.06 E+0	2.7 ± 0.2 E+0	135
74-149	Aliquot	3.2 ± 0.1 E+1	8.00 ± 0.03 E-1	2.4 ± 0.1 E+0	87
30-74	Aliquot	5.6 ± 0.6 E+0	1.6 ± 0.2 E-1	2.8 ± 0.4 E+0	22

NA = data not available at this time.